AN INVESTIGATION INTO THE THERMAL MODELLING OF INDUCTION MOTORS

BY

Amar BOUSBAINE

THESIS SUBMITTED TO THE
UNIVERSITY OF SHEFFIELD FOR THE DEGREE OF
DOCTOR OF PHILOSOPHY

DEPARTMENT OF ELECTRONIC AND ELECTRICAL
ENGINEERING
UNIVERSITY OF SHEFFIELD
JUNE, 1993

Acknowledgements

I would like to express my sincere thanks to Prof. M. McCormick and Dr. W.F. Low for their supervision, encouragement and many helpful suggestions during the study.

I am also grateful to my colleagues in the department for their advice and assistance. For my wife and family who were denied much of my time and interest which they could rightfully expect, I thank them for their tolerance and understanding.

The author is also indebted to the Algerian Government for his financial sponsorship.

Abstract

Electric motors are the ubiquitous workhorses of the industry, working a in wide range of conditions and applications. Modern motors, designed to exact ratings using new materials improved manufacturing techniques, are now much smaller but have higher loadings. They are being operated much nearer to the point of overload then ever before. To ensure a satisfactory life span for the motor, temperature rise must be limited to safe values. A lumped parameter thermal model has been developed, which allows rapid and accurate estimation of the temperature distribution in a machine. The lumped parameter thermal model depends on the accurate knowledge of the thermal coefficients and more importantly the loss distribution. Hence the temperature time technique was implemented to investigate the iron loss density distribution. Experimental results are discussed and loss density information throughout the volume of the machine was generated.

A novel method of determining the thermal coefficients employed in the heat flow equation was investigated, using the thermal lumped parameter model of a machine.

Finally a 2-D finite element method was used to corroborate, or otherwise, the use of the lumped thermal network model.

Contents

List of symbols

A	Surface (m^2)
A	Cross sectional area of fin (m^2)
A_1	Internal surface of a cylinder (m^2)
A_1	Surface of the frame casing which is in contact with the cooling air (m^2)
A_{Fin}	Surface of the fins (m^2)
A_f	Effective area of the frame casing (m^2)
C	Thermal capacitance $(W \times s/°C)$
C_p	Specific heat capacity at constant pressure $(J/Kg°C)$
d	Overall diameter (m)
F	scalar factor
G	Thermal admittance $(W/°C)$
$[G]$	Admittance matrix
h	Convective heat transfer coefficient $(W/°Cm^2)$
h_f	Film coefficient of the frame $(W/°Cm^2)$
h	Length (m)
h_{Fin}	Film coefficient of the fin $(W/°Cm^2)$
H_{Fin}	Axial length of cooling fins (m)
I	Current (A)
k_a	Lamination axial thermal conductivity $(W/°Cm)$
k_r	Lamination radial thermal conductivity $(W/°Cm)$
k_e	Apparent thermal conductivity $(W/°Cm)$
k_i	Thermal conductivity of the slot insulation $(W/°Cm)$
k_{Fin}	Thermal conductivity of the fin $(W/°Cm)$
k_{air}	Thermal conductivity of air $(W/°Cm)$
l_g	Airgap length (m)
N_{pr}	Prandlt number
N_u	Nusselt number
Q_1	Rotor copper losses (W)
Q_{in}	Power input to the motor (W)
Q_{stray}	Stray load losses (W)
Q_I	Iron losses (W)
Q_t	Total losses (W)
Q_{fc}	Friction losses (W)

Q_{sc}	Stator copper losses (W)
Q_{rc}	Rotor copper losses (W)
Q_{bI}	Proportion of iron losses allocated to back iron (W)
Q_{tI}	Proportion of iron losses allocated to teeth (W)
Q	Heat generated (W)
Q_1	External heat input (W)
$[Q]$	Loss vector
q	Heat generated per unit volume (W/m^3)
R	Resistance (Ω)
R_0	Thermal resistance $(°C/W)$
r	Radius (m)
r_1	Internal radius of a cylinder (m)
r_2	external radius of a cylinder (m)
R_1	Thermal resistance $(°C/W)$
R_2	Thermal resistance $(°C/W)$
R_m	Thermal resistance $(°C/W)$
R_a	Axial thermal resistance of a rode $(°C/W)$
R_r	radial thermal resistance of a rode $(°C/W)$
r	Rotor radius (m)
r_{sh}	Radius of the shaft (m)
R_x	Thermal resistance $(°C/W)$
R_y	Thermal resistance $(°C/W)$
R_{xc}	Slot copper thermal resistance in the x direction $(°C/W)$
R_{xi}	Slot liner thermal resistance in the x direction $(°C/W)$
R_{yc}	Slot copper thermal resistance in the y direction $(°C/W)$
R_{yi}	Slot liner thermal resistance in the y direction $(°C/W)$
R_x	Resultant thermal resistance of the slot in the x direction $(°C/W)$
R_y	Resultant thermal resistance of the slot in the y direction $(°C/W)$
R_{exc}	End winding thermal resistance in the x direction $(°C/W)$
R_{eyc}	End winding thermal resistance in the y direction $(°C/W)$
R_{ex}	Resultant thermal resistance of the end winding in the x direction $(°C/W)$
R_{ey}	Resultant thermal resistance of the end winding in the y direction $(°C/W)$
R_{ac}	Axial copper thermal resistance $(°C/W)$
R_{cv}	Convective thermal resistance $(°C/W)$
R_e	Reynolds number
t	Slot liner thickness (m)
δ	Equivalent width of the slot liner plus insulation between wires (m)
S	Slip
V	Speed (m/s)
T_a	Taylor number
V_{bi}	Volume of back iron (m^3)
V_t	Volume of teeth (m^3)
W	Equivalent width of a copper wire (m)
$[\theta]$	Temperature vector
$[\theta]$	Temperature matrix

α	Resistance temperature coefficient $(1/^oC)$
α	Coefficient
μ	Viscosity $(Pa \times s)$
ω	Angular rotor velocity $(rads/s)$
ρ	Density of air (Kg/m^3)
θ_{av}	Average temperature (^oC)
θ	Temperature (^oC)
θ_a	Ambient temperature (^oC)
θ_f	Temperature of the frame (^oC)
η	Efficiency of fins
P_c	The contact pressure (N/m^2)
a	Half the stator bore (m)
b	The radius of the core frame interface (m)
c	The frame barrel diameter (m)
μ_f	Poisson ratio for the frame material
μ_s	Poisson ratio for the core material
E_f	The elastic modulus of the frame (N/m^2)
E_s	The elastic modulus of the core (N/m^2)
δ	The outer core radius - inner frame radius (m)

Chapter 1

General introduction

Electric motors and drive systems account for 64% of industrial electricity consumption [1]. With the rise in energy costs it has become increasingly desirable to save electrical energy whenever possible. Energy which is not converted into useful work results in heating of the various motor components, and accounts for the motor losses. Obviously, the quantity of heat generated must be effectively removed to prevent damage to the machine. Although the losses are lower in smaller motors, they are no less susceptible to thermal problems. In absolute quantity, the losses in small machines are generally higher, per unit output, than for large machines [2].

Today the importance of energy conservation is widely recognised, and has given rise to many publications aimed at reducing energy consumption in industry. It is estimated that about 50% of electricity supplied to industry in the UK, in 1976, was consumed by electric motor drives [3]. A corresponding study in the USA revealed that 64% of the energy generated was consumed by electric motors [4]. These indicate the global importance and wide spread application of electric motor drives in industry.

With the implementation of more advanced cooling systems and the development of efficient integrated combinations of machine and power electronic circuits the use of the AC machine is now more widespread and a recent survey [3] in America found that about 53% of the total industrial electricity consumption was by AC motors. A similar survey [5] in Japan suggested that AC motors account for 85% of the market. It has been predicted that for the period 90-95, European sales for DC drives will increase by 20% whilst AC drives will leap by a massive 83%.

Of the various types of AC motors, the induction type is by far the most popular and most widely used. Their major advantages are low cost per kW output, simplicity, robustness, and high reliability. They operate for considerable periods in harsh environments with minimum maintenance, and have consequently become the work horse of modern industry. With the continued development of new methods of increasing efficiency, the induction motors will continue to dominate industry [6,7].

For years, industry accepted low load efficiency as a compromise for the many advantages of induction motors. However, the losses which were tolerable are now no longer acceptable as the trend is towards increasing rating for each frame size. Modern AC electric motors are now being operated much nearer to their point of overload than a few years ago. The traditional large motors, well endowed with thermal capacity and tolerance to over load, have given way to more efficient compact types which are designed to exact ratings using high quality materials, improved manufacturing techniques, and computer derived optimum designs.

Thermal modelling and efficiency are very relevant topics in the designs of today's engineers. Moreover, the trend towards the design of high power to weight ratio induction motors has stimulated renewed interest in the measurement and prediction of losses. The calculation of losses in induction motors is particularly important, as it

directly influences the temperature distribution, and also the overall motor efficiency. Predicting the temperature distribution is made difficult because of the uncertainties associated with assigning losses and thermal coefficients. With advanced analytical techniques, copper losses, can be predicted to a reasonable degree of accuracy. In contrast determination of iron losses results in different values depending on the method in use. The discrepancy between the calculated iron loss value and the experimentally determined value may be of the order of 20% [8].

These losses play an important role in determining the efficiency and temperature rise [9], and hence, the rating of a machine. The importance of stray load losses in induction machines was illustrated by Odok [10], who indicated that an improvement of 5% on the efficiency would mean a reduction in the losses of about 10%-15% of the input power. For the same temperature rise, the power output of the motor can then be raised by about 15%-20%. Hence, a small improvement of the average effective efficiency of the industrial motor would save energy. An improvement of 5% would amount to about a 2.5% saving of the total industrial electrical energy bill of 1977 in this country [3]. Theoretical and experimental work on stray load losses in induction motors have been carried out previously, but yet the present knowledge of the phenomena is by no means adequate for design purposes. The works of Murkherji [11], Schwarz [12], and Jimoh et al [13] provides a comprehensive list of references to published works on measurement of these losses, and discusses their origins.

The discrepancy between the practical and analytical results, on iron losses in general and stray load losses in particular, calls for the consideration of different approaches to the study of this topic [13]. The designer is in need of an easy and accurate method of measurement that would permit these losses to be studied more intensively, and in all probability to be ultimately reduced.

The accurate prediction of these losses, therefore, has a direct bearing on the overall cost and hence, competitiveness of a particular motor design. It was decided that a systematic and objective investigation of these losses in induction motors is imperative. To set the work in context, an up to date literature survey of published work on losses in induction motors is presented in chapter 2.

Schwarz [14] stated that the most accurate method for determining losses in machines of all types, is to use a direct calorimetric method, which is a relatively simple universal method. The thermal methods [15,16,17,19] offer some scope for indirect measurement approaches, since these depend only on losses. By using this approach, not only can the iron losses be determined but also separated into fundamental components. This information will enable the machine to be redesigned effectively to improve the efficiency and performance. The temperature time technique pioneered by Laffoon and Calvert [18] and later developed by Gilbert [19], relies on the fact that if a body is initially at a steady state temperature, when the internal heat source is removed, then the initial rate of change of temperature at any point is proportional to the heat input, i.e. loss density at that point. This method has a twofold purpose, firstly to determine the iron losses, including stray losses, and secondly to enable the spatial loss density distribution to be obtained throughout the machine. The latter has great importance in the determination of temperature distribution using either the lumped parameter thermal network or numerical techniques. Chapter 3 covers the theory and the performance of the method.

Electrical machines are composite structures in which the materials used range from conductors to insulators. The diverse combination of materials gives rise to a myriad of thermal problems unique to electric machinery and the solution to these problems has a great impact on the cost, size and to some extent, the feasibility of a particular design. Thermally, the insulation is by far the weakest component in any motor [20].

Deterioration of the electrical properties of insulation, caused by excessive temperature, occurs before any other material is affected. Overheating reduces the motor life and, if sufficiently severe, produces immediate burnout. On the other hand, the iron laminations are also subjected to thermal limitations since these are insulated from each other using materials which vary from organic varnishes to inorganic coatings, all of which have some thermal limit. To ensure a satisfactory motor life time, the winding temperature must therefore remain within its designated insulation class limit. In the view of the trend towards smaller motors, the risk of abnormal thermal conditions increases and the motor must therefore be protected against overheating.

For many years the most reliable design tools for thermal design was test information obtained from other machines. This has led to the thermal designs based on overall losses, heat transfer area, average heat transfer coefficients, etc, for existing machines. This approach does not lend itself well to machines outside the range of test information available. Today designers rely on a more detailed approaches such as thermal networks, finite difference/element methods.

Thermal models [17,21,22,23,24,26,27] based on lumped thermal network, are simple and can give relatively accurate representation of the thermal conditions within the machine. It is based on the analogy between Ohm's law for electrical conduction and Fourier's law for heat conduction. The principal of the method is to divide the machine into a number of regions each of which is modelled as a point source approximating to the mean temperature of the region. These are interconnected to their neighbours by thermal admittances derived from a basic region geometry. Soderberg [23] presented a model to represent the approximate solution of the heat conduction processes and applied it to a large turbo generator with radial ventilation. Here the stator structure is divided into the tooth region and core which is connected to the teeth. In the analysis, the internal losses in the machine are assumed to be

generated at a number of locations and interconnected by an equivalent resistance network, each of which can be determined analytically.

The lumped parameter model has also been used for studying the heat flow within electric machines. An approximate equivalent network [15,16,21] has been used to represent the whole machine. Others introduced drastic assumptions to alleviate the complexity of modelling the actual bulk conduction and convection processes [22]. Recently, a more refined thermal network has been reported [17,24,26] for a wide variety of machine configurations, and operating conditions. A number of authors applied such steady state models to the transient case by associating a thermal capacitance with each element [26,28].

The lumped parameter thermal model can be implemented in the electronic circuits which receive their information from motor currents. In so doing the electronic circuit takes into account not only the heating effect of the current in the winding, but also the heat sink effect of the body of the motor, iron core, and the transfer of heat from copper to iron. They can also stimulate the cooling of the motor, depending on whether the motor is running or stationary. The equivalent thermal circuit is the heart of sophisticated electronic protection relays [29], and it is a means by which a designer is able to predict temperature rise in an induction motor.

A detailed study of the thermal parameter lumped model is covered in chapter 4, and its application to a 4kW totally enclosed fan cooled induction motor along with its solution is given in chapter 5.

For a prediction of temperature within an electric machine it is necessary to know the location and magnitude of heat loss, the thermal properties and the thermal behaviour of the cooling system. However, considerable uncertainties exist regarding

the thermal conductivities of the materials from which the machine is constructed, and the film coefficients at the cooled surfaces [30]. There are often discrepancies in the measured thermal conductivity, even of common materials, without it being at all clear whether the divergence is due to difference between samples or to inaccurate measurements. On the other hand, the subject of thermal conductivity in machines is unlikely to be dealt with thoroughly because of the difficulties involved in a rigourous treatment [31]. For example, there is a considerable difference in the methods of insulation, fitting of the coils into the slots, impregnation of winding etc., of various types of machines, all of which cause variations in the thermal conductances. There may also exist slight constructional differences between identical machines which contribute to unpredictable differences in the thermal behaviour. Therefore, the thermal coefficients that are necessary for the temperature calculations cannot be determined directly from values of specific thermal conductivities taken from tables of physical properties. Such data must be obtained by analysis on actual machines.

Information on thermal properties is characterised by two facts; what is known is widely and confusingly scattered , and the unknowns generally outnumber the known [32]. Roberts [30] measured the thermal conductivities of packets of enamelled laminations of various thicknesses and compressions and showed that the thermal conductivity along the lamination depends on the silicon content, whereas the thermal conductivity normal to lamination depends on:

- Individual lamination thickness
- Surface finish of the laminations
- Pressure under which laminations are clamped
- Type and thickness of interlaminar insulation

The whole subject thus remains clouded due to the discrepancies that exist for many materials. The uncertainty can be dispersed only with an infusion of reliable data which can be accomplished by becoming aware of the difficulties and pitfalls that are so prevalent in the determination of this property. Chapter 6 deals with an improved method of determining the apparent thermal conductivities using an equivalent thermal circuit of the whole machine. The accuracy of the method relies on the accurate knowledge of the temperature and loss density distributions within the machine.

In recent years, digital computers have made a very large impact upon design methods for rotating electrical machinery, and have literally revolutionised the design process which continues unabated. For the problems involving complex material properties and boundary conditions, the engineer resorts to numerical methods that provide very accurate results. The accuracy and efficiency of the finite element method in comparison to the standard finite difference method used for computation of temperature was studied by Emery and Carson [34]. They demonstrated that the computation of the steady state temperature using finite element method is superior. A two dimensional finite element method for the solution of the steady state heat flow in the stator of induction motor has been studied by Sarkar et al [35]. A more elaborate three dimensional finite elements have been introduced for the solution of both steady state and transient heat flow equations in the stator cores of large turbine generators by Armor [36,37] and Sarkar et al [38,39]. Since there were discrepancies between the results obtained experimentally and those obtained using the lumped parameter model, the finite element method was used to corroborate, or otherwise, the results of the lumped parameter model. Chapter 7 discusses the use of the finite element method used to establish the temperature distribution in an induction motor. The results of the lumped parameter and finite element methods were compared and conclusions drawn.

Finally, conclusions and recommendations for further work are reported in chapter 8.

Chapter 2

Losses in Induction Machines

2.1 Introduction

An electric machine converts mechanical into electrical energy in the generator mode, and electrical into mechanical in the motor mode. In so doing, the machine incurs losses which are lost as heat. These losses determine the efficiency and the ventilation requirements of the machine so that the allowable temperature is not exceeded. To obtain maximum efficiency and reliability from a machine, considerable care must be taken by the designer in utilising different methods of minimising losses, and providing sufficient thermal capacity in the machine to absorb and/or dissipate the losses associated with any desired duty cycle. Industrial motor standards are continually improved and updated by the addition of new materials, or by changing the existing materials to produce appropriate recommendations aimed at achieving these objectives. Moreover, as energy conservation is becoming increasingly important, the trend is now towards development of high efficiency motors as well as motors with high power to weight ratios. Therefore, in the construction of modern

electric machines, every effort is made to take full advantage of active materials in order to raise the efficiency and reduce the weight of the machines. Whilst most users of electrical machines will agree that losses take second place to reliability, nevertheless they play a significant role in the assessment of tenders. Therefore, there exists a strong case for trying to evolve methods for accurately measuring these losses.

Losses are produced by magnetic fluxes and electric currents in electric machines which have complicated distributions such that the sources of losses are often ambiguous. Furthermore, when heat is generated its dissipation follows yet another complicated thermal pattern since the machine consists of materials which have different thermal conductivities in different directions. The cooling medium also has a major effect on localised temperatures and again the distribution of the flow of coolant is almost indeterminable [40]. As a result, various classifications of losses have been adopted for practical purposes. British standard [41] subdivides losses in a machine into three components:

a) **Fixed losses :**

1. Losses in the active iron, and additional no load losses in other metal parts
2. Losses due to friction
3. The total windage loss in the machine

b) **Load losses :**

1. I^2R losses (copper losses) in primary windings
2. I^2R losses in secondary windings

c) **Additional load losses :**

1. Losses introduced by load in active parts and other parts other than the conductors.
2. Eddy current losses in primary or secondary winding conductors caused by current dependent flux pulsation

Another alternative is to segregate losses into [42,43]:

a) **No load losses :**

1. Iron losses
2. Windage and friction losses

b) **Load losses :**

1. Stator I^2R losses
2. Rotor I^2R losses
3. Stray load losses

The last classification is taken as the basis on which to discuss the losses occurring in a squirrel cage induction motor. Fig. 2.1 gives the global scheme according to this classification.

2.2 No load losses

2.2.1 Iron losses

Iron losses are the losses that occur in the iron as a consequence of an alternating magnetic field. The losses comprise hysteresis and eddy current losses resulting from

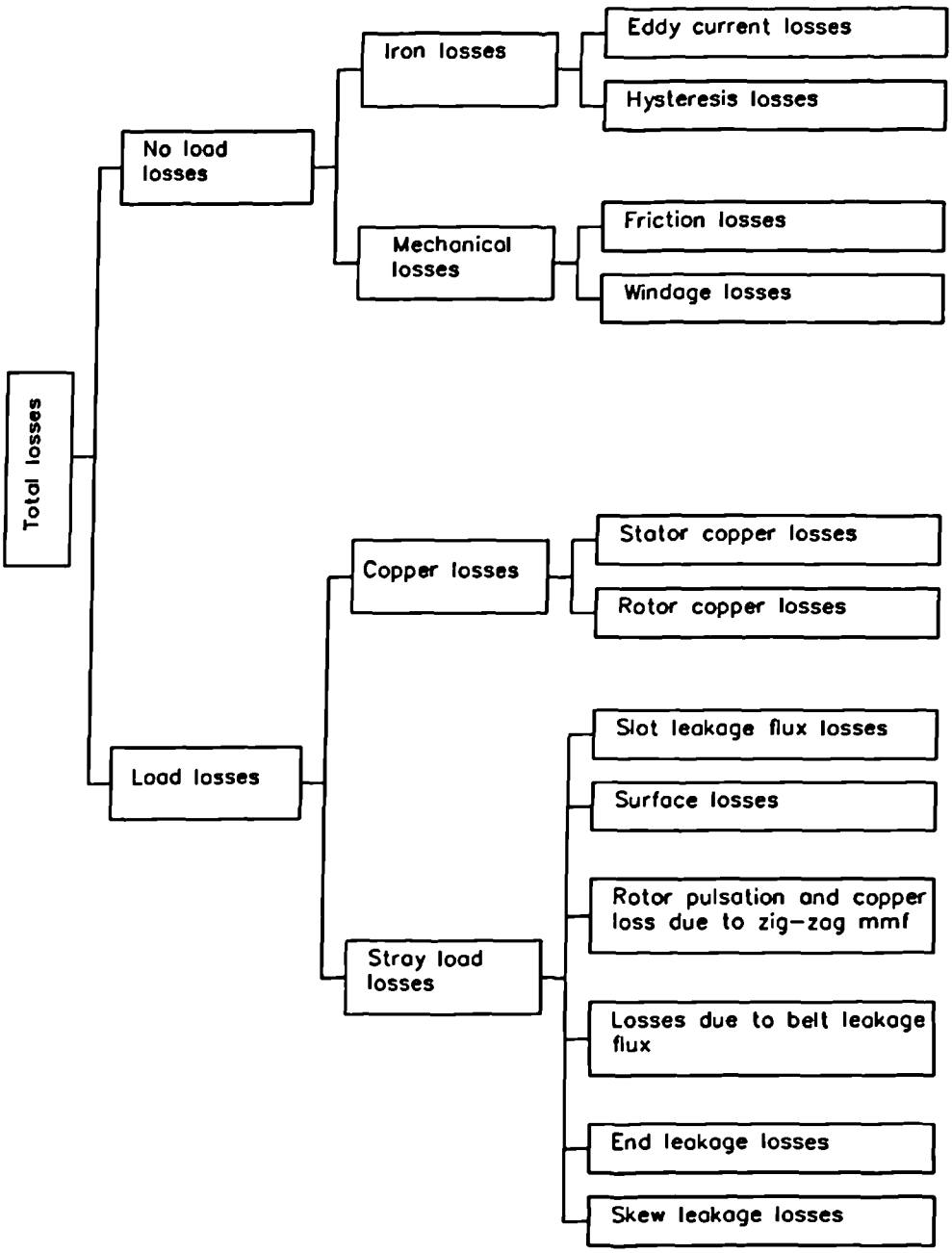

Fig. 2.1 Induction motor loss segregation.

the induction of currents which circulate within the conducting material. The iron losses mainly occur in the stator magnetic sections, since under normal operating conditions the frequency of the rotor flux is low, resulting in small rotor losses.

Iron losses can be calculated empirically, but it has been shown [8] that this generally results in a higher figure for iron loss than that obtained using a more rigourous analysis based on tests. A rigourous analysis of hysteresis losses, however, is difficult owing to the fact that not only does the angle between B and H vary throughout the given cycle of magnetisation, but the shape of the loop itself varies with the maximum value of the magnetisation. Rao [44] approached the problem by replacing the actual hysteresis loop with an ellipse which has the same maximum magnetisation and the same area as the closed loop, and hence was able to establish that the saturation of the mean magnetisation curve results in iron loss different from eddy current loss.

An attempt to find a more accurate method of calculating iron losses with minimum empiricism was presented by Alger and Eksergian [45] in which flux densities in the core of a cylindrical machine, corresponding to a sinusoidally distributed radial air gap flux density were determined by solving Maxwell's equations for a smooth air gap boundary. It was observed that the flux density vector at each point of the core describes an elliptical cycle. Thus by formulating the problem in terms of radial and tangential components of the flux density, eddy current losses due to these components can be calculated separately, since they are always mutually perpendicular in space and can have no interaction.

Linkous [46] attributed higher core losses to skew of the rotor currents with respect to the stator currents, which resulted in higher flux density in the end laminations than the middle region.

The introduction of computers has led to the application of powerful numerical techniques, such as finite element and finite difference methods to the electromagnetic modelling of electrical machines. This has since been extended to the thermal modelling of electrical machines [33,36,38]. Lorenzen and Nuscheler [47] suggested that the basic requirement for loss calculation is a knowledge of the dependence on space and time of the flux densities in the plane of lamination. They ascertained this dependency by using a 2-D finite difference method which took into account the anisotropy and nonlinearity of the material. However, the problem of empiricism still exists since the iron loss in the discretised domain is determined using the measured power loss information for the same material derived using semi-empirical methods. Bertotti [8] used a 2-D finite element model to compute the iron losses. Here the peak flux density was evaluated in each element of the mesh to determine the corresponding loss through a known dependence of the loss versus induction, as provided by the standard material specifications. Bertotti concluded that the computed core losses were about 20% lower than the measured and attributed this to the additional loss contribution from eddy currents in the stator cage and the actual deterioration of the material properties during lamination punching and core assemblage. In a more recent publication, Atallah [48] used finite element analysis to obtain a series of instantaneous magnetostatic field distributions within a permanent magnet brushless DC motor. The localised iron loss densities were determined for an infinitely long machine by analysing the temporal and spatial variation of the flux density distribution. From this it was concluded that the iron loss markedly alters and is dependent upon the operating conditions of the machine.

An alternative method for determining iron losses is the calorimetric method. Since all the power losses within machine appear as heat, the determination of the losses through the accurate measurement of the heat output from the machine is possible. This has the advantage that the losses are obtained directly in terms of heat

units, which can be measured to a relatively high degree of accuracy and make no assumptions regarding type of supply or frequency. Laffoon and Calverts [18] used a calorimetric method to determine the losses of a high speed synchronous machine by measuring the volume and temperature rise of the cooling medium, and concluded that while the calorimetric method is quite satisfactory for measuring total losses, it is not applicable for measuring the specific heat loss in different parts of the machine, since these usually represent a small percentage of the total measured loss. The main drawback is that this method is slow, tedious and it is often difficult to obtain a perfect heat insulator to eliminate all heat leakage. Furthermore, the accuracy of the method relies heavily on the accurate measurement of air flow, temperatures, pressure, humidity, and their distribution across the flow path. Turner et al [49] avoided the necessity of measuring the relative humidity, barometric pressure, and the temperature and the flow profile across the entry and exit ports, by providing a heat source within the calorimeter. Initially, the machine is externally loaded and operated at the desired load until the temperature rise in the air flowing through the calorimeter is constant. The unexcited machine is subsequently rotated and the air flow rate kept constant, ensuring that the flow conditions in the equipment remained the same, and heat is supplied to the air by an alternative source (heater). The electrical input to the heater is then adjusted to give a temperature rise in the air flow which is the same as that measured during the first test. From the test results, it was estimated that the resolution of the method was approximately 0.8% of the full load and 2.6% of the no load excluding friction and windage losses.

2.2.2 Friction and windage losses

In fan cooled machines the power required to drive the fan and to overcome the air resistance presented to the other rotating parts of the machine is classed as windage

loss. Losses caused by the resistance to the motion within the bearings is classed as friction loss. In reality it is not possible to separate the windage and friction losses in a machine as both are associated with rotation. Nevertheless, at low speeds the windage losses associated with rotation are small and an estimate of friction loss can be made. On the other hand, at high speed the predominant component of these losses is due to the external fan which drives cooling air across the machine frame. These friction and windage losses are usually empirically determined. For example, Alger [50] estimated that a typical value for friction and windage losses in a 7.5 kW, 1800 rpm induction motor is about 1.5% of its full load output, and increases roughly as square root of the speed.

In practice, the measurement of iron, friction and windage losses are straightforward using a series of no load tests despite all the complexities involved in their prediction. In the no load test, the machine is run at rated voltage and frequency without any connected load until the power input becomes constant. The power input at the rated voltage will therefore be the sum of the friction and windage, core, and no load primary copper losses. Subtracting the calculated copper losses at the test temperature from the power input gives the sum of the friction and windage, and core losses. The friction and windage losses can then be segregated from the core losses by varying the applied voltage, at rated frequency, between 125% of rated voltage down to about 25%. Since the speed will only vary slightly during the test, friction and windage losses will essentially be constant and by extrapolating to zero volts these losses can be determined as shown in Fig. A.3 in appendix A. For greater accuracy a correction for the stator copper loss should be made by deducting the appropriate values of I^2R before plotting the power curve.

2.3 Load losses

2.3.1 Copper load losses

Copper losses are a consequence of current flow in the stator and rotor conductors, and can be calculated from the equation I^2R, where R is the circuit resistance which is a function of both temperature and frequency.

Measurement of copper losses follows the general method outlined in standards [41, 42]. The stator copper loss is directly determined by measuring the d.c. resistance of the winding at a known temperature and adjusting the resistance for temperature effects using

$$R_t = R_a(1 + \alpha(\theta_t - \theta_a)) \tag{2.1}$$

where,

R_t:the test value of the winding resistance

R_a:the winding resistance at the ambient temperature

θ_t:the test winding temperature in degree Celsius

θ_a:the ambient winding temperature in degree Celsius

α:the temperature coefficient of resistance

and multiplying by the square of either a measured or calculated primary current.

Rotor copper loss is determined indirectly by measuring the slip and the input power at the required load and is given by

$$Q_2=(Q_{in} \text{ - Stator } I^2R \text{ - Iron loss})\times S$$

where S is the slip

Generally, stator windings are made up of relatively small wire gauges and skin effect can be neglected. Thus only the temperature effect, which alters the resistivity of the conductors, needs to be considered.

If the conductors are of a large cross sectional area, as in the case of squirrel cage induction motors, the apparent resistance will be different from the d.c. resistance at high slips due to the distorting effect of the induced currents in the conductor, and the effect of current in adjacent conductors and surrounding iron, which result in the current being forced towards the top of the conductor. The effective resistance of the conductor can be calculated from the assumption that all the current flows with uniform density within the skin depth. Liwschitz-Garik [51,52] developed analytical equations detailing the calculations of the skin depth and showed that the skin depth is approximately independent of shape.

2.3.2 Stray load losses

Stray load losses are defined as the additional losses which occur due to changes in the load condition. These losses are partly due to eddy currents in armature conductors, solid copper, end ring; hysteresis and eddy current in portions of the main magnetic circuit as well as in the stationary structural parts of the machines.

Some theoretical and a considerable amount of experimental work [13] has been carried out to quantify these losses in electrical machines, but the present knowledge of this phenomena is by no means adequate for design purposes. Although this subject has been investigated for many years there is still disagreement on the definition and components of stray load losses. According to Jimoh et al [13] the major reasons

for the confusion are associated with the following:

- Each author made the classification compatible with his own contribution.
- The confusion in identifying the components that constitute differential leakage fluxes.
- The confusion that arises from the use of term 'leakage flux' and 'harmonic flux'
- The confusion that arises from the inter-usage of the terms 'differential leakage', 'zigzag and phase belt leakage', and 'airgap leakage' even though they are the same.

The most objective definition is that given by Alger et al [53] which defines the losses as the excess of the total losses actually occurring in a motor at a given load current over the sum of the calculated copper losses for that current, the no load core losses, and the friction and windage losses. Christofiedes [54] defines stray load losses, in a mathematical form, as the difference between the total power loss of the machine on load and the losses determined by the loss segregation method.

$$Q_{stray} = Q_t - (Q_I + Q_{fw} + Q_{sc} + Q_{rc})$$

where

Q_{stray}:stray load losses,

Q_t:total losses of the machine on load,

Q_{fw}:friction and windage losses,

Q_I:iron losses deduced from no load test,

Q_{sc} and Q_{rc} are the stator and rotor copper losses respectively.

This definition is based on the way that stray load losses manifest themselves under load conditions. It does not define load losses in terms of their causes, nor does it state the place at which they are dissipated.

Included in the definition of Q_{stray} are the losses due to the flux harmonics known as tooth pulsation fluxes, produced by the slotting on either sides of the airgap. These harmonics are independent of the currents and their amplitudes depend only upon the variation in the airgap reluctance and the magnitude of the main flux. Since these losses are also produced on no load when the machine is excited by a purely sinusoidal airgap m.m.f, they are hence fundamentally different in nature from the losses produced by the m.m.f harmonics, and are defined as stray no load losses [12].

No standard list of stray load loss components exists, however, it is important to know the nature and the origin of the component of stray load losses. For clarity the major components of stray load losses and their descriptions follow:

1) Losses due to slot leakage flux: These are due to current flow along the stator slots which give rise to leakage flux across the slots. The cross field in the slot produce additional copper losses through skin effect which forces the current to flow in the top part of the conductor, thus decreasing the effective area of the conductor and increasing its resistance.

2) Losses due to the end leakage flux: The peripheral currents in the overhang of the end winding set up fluxes which enter the laminations in the axial direction and penetrate the end region metal parts. This leakage flux induces eddy current losses in the conductive components of the stator end region. These losses vary not only with the design of the end winding but also with the distance of ventilating

shields, the centres of the peripheral currents in the stator and rotor end windings and the distance of the end metal parts from the end windings [53], etc. Due to the geometrical and electromagnetic complexities the estimation of these losses is extremely difficult. Nevertheless, it has been found that it is satisfactory to assume that the stray load losses in the end region of induction motor are equal to a portion of the volt amperes of the end leakage reactance, multiplied by an empirical constant, usually taken to be equal to 0.3 by Alger et al [53].

3) Surface losses due to zigzag leakage flux: The stator flux distribution in the airgap is not sinusoidal because the airgap m.m.f wave is stepped due to the concentration of currents in slots, and the effect of slot openings. These cause slot frequency pulsation in the radial flux density around the airgap, producing eddy current in the iron surfaces of the stator and rotor laminations.

The peripheral air gap flux distribution can be decomposed into a series of rotating harmonics fields, the principal ones being the stator and rotor slot harmonics with pole numbers equal to $2n_1 \pm 1$ and $2n_2 \pm 1$ times the fundamental poles, where n_1 and n_2 are the number of slots per pole in the stator and rotor respectively. Although the slot harmonic fields caused by both the slot openings and the steps in the m.m.f distribution have the same frequency and number of poles, the losses due to the stator slot openings (permeance harmonic loss) are at no load, while the losses due to nonsinusoidal m.m.f are at load losses. An analytical study of these losses was carried out by Christofides [54] who concluded that when the flux paths become saturated by the main flux, the harmonic m.m.f and flux density waves are appreciably reduced resulting in a reduction in surface losses.

4) Losses due to belt leakage flux: The low order harmonic fields due to the phase belts of the stator winding also induce currents in the rotor producing additional losses. These losses are small in wound rotor machines but are of importance in squirrel cage motors. For these fields the impedance of a squirrel cage motor is small in comparison with the magnetising reactance when the machine is operating at full load. Therefore all the stator load current is assumed to flow through the rotor for the phase belt harmonics. Alger et al [53] gave an expression for these losses assuming the magnetising current to be negligible.

5) Losses due to skew leakage flux: When the rotor slots are skewed one slot pitch, assuming the current to be the same throughout the length of the bar, there is a phase displacement of the fundamental m.m.f waves of the stator and rotor towards the two ends of the core [46]. This phase displacement increases linearly as one moves away from the centre of the active conductor in the axial direction to the ends, to give a corresponding increase in the radial flux density and hence producing extra losses known as skew leakage losses.

6) Rotor pulsation and I^2R losses due to zigzag leakage flux: These losses are due to the penetration of high frequency fluxes into the rotor teeth, causing circulating currents in the rotor windings. One of the most important parameters influencing the magnitude of these losses is the number of the rotor slots, since this determines the degree of coupling between the slot harmonics and rotor circuit. From this point of view, the ideal arrangement would be to make the stator and rotor slot numbers equal to ensure minimum harmonic penetration. In practice, this introduces undesirable cogging torques. With unequal stator and rotor slot numbers, the net circulating voltage, due to the stator slot harmonic field, around each rotor tooth depends upon the difference between the slot numbers. As the

ratio of rotor to stator departs from unity, more stator slot harmonic field pass down to the rotor teeth greatly increasing the pulsation and I^2R losses. However, if the slots are skewed one stator slot pitch, regardless of the slot ratio, the voltage induced in the bars will be nearly zero, but there will be a considerable voltage acting across the slots. Where the bars are not completely insulated, the difference in the voltage induced between adjacent bars will cause currents to flow in a circumferential direction. These currents produce extra losses in the teeth, and also some I^2R losses in the bars [55].

In the design of a high efficiency machine it is important to know the magnitude of these losses so that steps may be taken to reduce them. There are direct and indirect methods of determining stray load losses and they are presented in the IEEE Std.112 [42].

1) **Direct method:** The stray load losses are determined by the input-ouput method which consists of measuring the input and output powers, the difference being the total loss in the machine. From this copper losses in both stator and rotor, stator iron losses and friction and windage losses are then subtracted to give the stray load losses. This method can be inaccurate as it requires the subtraction of two nearly equal quantities and hence demands a very high level of measurement accuracy. Schwartz [12], for example, showed that for a machine of 90% efficiency an inaccuracy of only 1% would produce an error of 10% in the losses which is of the same order as the stray load losses being determined.

2) **Indirect method:** For the strict compliance with IEEE Std.112 [42] the stray load losses are determined by the reverse rotation test. This test is based on the assumptions that tooth frequency flux pulsations are the main source of high fre-

quency stray load losses; that these losses can only be supplied by mechanical power, and that their value is the same for both full speed forward and reverse rotations. However, Chalmers and Williamson [61] have shown that these assumptions are, to varying degrees, fundamentally incorrect and this view supported by Bird [56], and Schwartz [12].

Stray load losses of induction motors are critically dependent on the power factor which determines the phase relationship between the stator and rotor m.m.fs. The tests devised and employed for the measurement of stray load losses come under two groups:

a) **Full load test methods :**

1. Input-output
2. Pump back
3. Calorimetric
4. Differential dynamometer
5. Mechanical differential
6. Back to back

b) **Light load test methods :**

1. Ac/dc short circuit
2. Reverse rotation

From theoretical and practical investigations Schwartz [12] concluded that making an allowance for stray load losses is a reasonable and practical method for declaring efficiency. However, if no figures are available from test methods outlined above, a

nominal value of 0.5% of the input power for motors is approved by British Standard [41]. ANSI [57], however, states that unless otherwise specified the total value of stray load losses at rated load is equal to 1.2% of the rated output for motors rated less than 1865 kW, and 0.9% of the rated output for motors rated at 1865 kW and greater, when using method F1 stated in [42]. For some designs of small machines these losses might be higher than 0.5%, several authors have reported values well above this limit. Barton and Ahmad [58] demonstrated that the figure quoted by British Standard [41] was totally inadequate. A further shortcoming was given by Alger [14] who observed that this practice does not give the designer any preference nor encourage development work in this subject.

In general, the induction motor operates at near constant speed. Certain applications, however, call for variable speed induction motors, and modern methods of static frequency conversion have liberated the induction motor from its historical role as a fixed speed machine. However, because the output voltage and current of static converters are nonsinusoidal, and rich in harmonics, they have adverse effects on the induction motor performance. In general, the nonsinusoidal waveform is treated by decomposing it into fundamental and associated harmonics, considering their effects separately. This approach, whilst satisfactory for calculating copper losses, is not accurate for calculating iron losses because of the nonlinearity of the magnetic circuit [59].

The presence of harmonics in both the stator and rotor currents means that the total r.m.s value of the currents will be larger than the fundamental value hence an increase in losses. At harmonic frequencies the current distribution within the bar does not remain uniform due to skin effects, and this increases the resistance of the bar, which not only dependents on bar depth but also on the shape, material, frequency and slot topology. Klingshirn and Jordan [60] pointed out the presence of

harmonics in the applied voltage waveform can cause the flux density in the air gap to be approximately 10% greater than the fundamental value, leading to an increase in the stator core losses.

According to Chalmers and Williamson [61] the complexities of the problem and small amount of iron losses to be expected, do not justify the time consuming calculations involved in taking the nonlinearity into account. This opinion is not shared by Klingshirn and Jordan [60] who have taken into account the problem albeit by rather simplified methods.

An appropriate method for assessing losses is to use electrical network models. The method represents the machine by lumped circuit parameters from which losses can be calculated. Benamrouche [62] examined in detail three models to calculate the losses of a 4kW induction motor with sinusoidal and nonsinusoidal supply. The first model is based on the conventional Steinmetz equivalent circuit, the second on an equivalent circuit modified to account for stray load losses, and the third is the extended chain equivalent circuit. The loss components calculated for each model were compared to those obtained experimentally. The conclusion drawn was that present induction motor models are not sufficiently accurate due to the difficulties involved in modelling iron losses.

2.4 Conclusion

In an induction motor, losses in magnetic materials account for 10-20 % of total losses [7]. The iron loss effectively reduces both the output capability and possibly the life of the machine. To limit these undesirable effects a prior requirement is to accurately assess the iron losses, and understand their nature and ideally their

spatial location. Conventional induction motors incorporate steel rotor and stator cores, which are laminated to inhibit the flow of eddy currents. Core materials have developed rapidly over the last 20 years. Today, thin steel plates (down to 0.18mm) can be produced for laminations, and the steel suppliers have improved the grain size, and removed the crystalline structure altogether in some cases (in amorphous alloys). This has increased the permeability of the alloys and has reduced eddy currents and hysteresis in cores formed from these materials.

While the methods stated in this chapter are quite satisfactory for calculating the losses, there is no method for checking the distribution and location of the losses throughout the various parts of the machine. An accurate knowledge of the loss distribution is essential for temperature rise calculations which forms one of the major objectives of this thesis, and this is dealt with in detail in chapter 4.

Although the problem of stray load losses has been treated in a great number of papers, the questions concerning this subject qualitatively are still not clear. The experimental investigation of stray load losses in an assembled machine poses one of the most difficult measurement problems in the assessment of a machine. The difficulties in the measurement of these losses lie not only in the complexity of the measuring method but rather in the degree of accuracy required.

A satisfactory method for determining the distribution of losses within the machine and for providing information on stray load losses is the temperature time technique. The following chapter discusses this method and discribes its application to the thermal analysis of induction motors.

Chapter 3

Local loss density measurements using a thermometric method

3.1 Introduction

The heat generated within a machine is transferred to surrounding regions by a combination of conduction, convection and radiation processes. The dominant processes in heat transfer within the motor, and to the environment, are conduction and convection whereas radiation is important only on the outer surfaces. Conduction is the first stage in the process of heat flow from the generation site to the outer surfaces, after which convection takes over. The conduction process can be mathematically described using a second order differential equation of the diffusion type, whereas the convection mode is described by Newton's law of cooling. Any accurate thermal model must therefore encompass these modes of heat transfer.

Thermal models fall into two categories; those employing numerical techniques [33,

36,38], and those using lumped parameters [17,21,22,23,24,26]. In the first category, which includes finite element and finite difference methods, the machine is discretised into small elements, or grids, and the appropriate heat flow equations are applied to each finite element, or to each node. These methods account well for the conduction mode of heat transfer but it is very difficult to obtain such satisfactory results with the convection and radiation modes [24]. These methods produce a large amount of data, and hence require a large amount of computation to obtain reasonable results.

The second category, based on an electrical circuit analogy, is conceptually simple and requires the machine to be divided into a number of homogeneous elements or blocks, each of which is treated as a node and connected to adjacent nodes by thermal conductances. Heat generation, or storage, in the element is assumed to occur at the nodes. The appropriate choice of thermal network depends on the level of accuracy which is being sought. In general, it is desirable to select a scheme which represents sufficiently accurately the physical division of the machine into parts, without being overly complicated as with numerical methods. The thermal model relies on a complete knowledge of the dimensions of the machine, material properties, and the heat generated at the different nodes.

The main goal in thermal modelling is to predict the temperature rise rather than the loss distribution. Recently, however, this method has been extended to the investigation of the distribution of losses within the machine volume using the temperature distribution as the main indicator of losses. For example, Bahbouth et al [15] applied the thermal model by dividing a 0.746 kW induction motor into three basic thermal blocks viz, stator windings, stator including the frame, and rotor. Here it was assumed that the temperature drop in the axial direction of the stator laminations is negligible, as is the temperature drop between the rotor core and rotor teeth, and between rotor core and the shaft. Then by comparing the experimental and

the predicted temperature distribution the loss distribution within the machine was predicted for different power sources, viz, variable frequency sine wave and inverter. The same approach was adopted by Oliver et al [16], and a more sophisticated slip ring induction motor model was developed by Chitlet et al [17]. Similar work was presented by Numburi and Burten [27] who took steady state temperature rise as a direct indicator of loss. Their investigation was focussed on the end regions of the machine where an extensive statistical study was used to interpolate the experimental data from which resulted a simple model representing the interaction of the copper and iron losses.

The difficulty in determining, numerically, the factors which govern the heat flow, especially convection and radiation, limits the accuracy of the predicted temperature distribution. This is further compounded by the need to assume that the heat flow is negligible in the axial direction. Consequently the predicted temperature distribution, and hence loss distribution within the volume of the machine, are inaccurate. To remove any ambiguities related to the loss distribution, a thermometric method based on the temperature time method is used. The method was pioneered by Laffoon and Calvert [18] who applied it to measure the core loss in a synchronous machine, and further developed by Gilbert [19] who used it to investigate the core losses of alternators and transformers. The temperature time method has been applied by Czerhisky and MaCmillan [63] in a novel manner to measure the core loss of a magnetic material sample.

3.2 Temperature time technique

The temperature time method is based on the fact that losses generated in the different parts of the machine, as a consequence of operating conditions, can be obtained by measuring the energy absorbed or released when the operating conditions are altered. The initial rate of change of temperature is then proportional to the heat input at the measurement points, provided the cooling remains constant for the duration of the test.

3.2.1 Theory of the method

For an ideal homogeneous body within which heat is generated and dissipated to surrounding regions, the heat balance equation is given by [64]:

$$Q = G(\theta - \theta_a) + C\frac{d\theta}{dt} \tag{3.1}$$

where

Q:heat input,

G:thermal admittance,

θ:temperature of the body,

θ_a:ambient temperature,

C:thermal capacitance.

If heat input is removed (i.e. $Q = 0$) when the steady state conditions are reached, with all other conditions remaining constant, then Eq. (3.1) reduces to

$$G(\theta - \theta_a) = -C\frac{d\theta}{dt} \tag{3.2}$$

and the solution of the differential equation is given by,

$$\theta = \theta_a + c_1 exp - \frac{G}{C}t \tag{3.3}$$

where c_1 is the constant of integration determined from the initial conditions, i.e. at $t = 0$ (the instant of switching off), $\theta_{t=0} = \theta_0$, steady state temparature. The resultant expression for the temperature is thus

$$\theta = \theta_a + (\theta_0 - \theta_a) exp - \frac{G}{C}t \tag{3.4}$$

The initial slope of the cooling curve is given by

$$\left(\frac{d\theta}{dt}\right)_{t \to o} = -\frac{G}{C}(\theta_0 - \theta_a) \tag{3.5}$$

Moreover, prior to the removal of the heat input, when steady state conditions were reached $\frac{d\theta}{dt} = 0$, and so from Eq. (3.1)

$$Q = G(\theta_0 - \theta_a) \tag{3.6}$$

The loss density is therefore given by substituting Eq. (3.6) in Eq. (3.5) to give

$$Q = -C\left(\frac{d\theta}{dt}\right)_{t \to 0} \tag{3.7}$$

Hence, for any point within the volume, the rate of heat flow (loss density) is proportional to the initial rate of decrease of temperature.

The temperature time method therefore involves the measurement of temperature at selected locations over a short period of time.

3.3 Selection of sensors

To implement the temperature time method, the temperature must be recorded in the shortest time possible. Furthermore according to Ball and Lorch [65], the temperature sensor should be as thin as possible to reduce the influence of its thermal

mass on the local temperature rise, which is particularly important for short measurement times. Moreover, if such a sensor is to be embedded, for example in the stator, then the diameter of the drilled holes should be as small as possible so that the magnetic circuit is not disturbed. Thermocouples should satisfy these criteria and are small and robust enough to withstand vibration effects. To improve robustness, the thermocouples should be of the mineral sheathed type. These are integrated units where the space between the thermocouple wires and flexible sheath metal is filled with magnesium oxide, which is both a good heat conductor and electrical insulator. The junction is welded to the tip of the sheath which has the advantage of a very quick response to thermal changes, and because it is flexible, it can be bent. However, this cannot be done too often as the wires tend to break, or the insulation becomes displaced and the thermocouple short circuits. Table 3.1 [66] shows the characteristics of the commonly used thermocouples, and taking into account of the range of temperatures within a motor, T type thermocouples were chosen.

Type	Conductor material (positive conductor first)	Temperature range °C	Tolerance on temperature C
E	Nickel: Chronium/Constantan	0 to 400	± 3
J	Iron/Constantan	0 to 300 300 to 850	± 3 ± 1%
K	Nickel:Chronium/Nickel:Aliminium	0 to 400 400 to 1100	± 3 ±0.75%
T	Copper/Constantan	0 to 100 100 to 400	± 1 ±1%
R	Platinium:13% Rhodium/Platinium	0 to 1100 1100 to 1400	± 1 ± 2
S	Platinium:10% Rhodium/Platinium	0 to 1100 1100 to 1400	± 1 ± 3
B	Platinum: 30% Rhodium	0 to 1100 1100 to 1550	± 3 ± 4

Table 3.1: Commonly used thermocouples to British standard

Mineral insulated thermocouples, supplied by Labfacility Ltd, having a diameter of 0.5 mm, and response time of 0.3 s (manufacturer's data) were used. The metal sheath is terminated by a pot seal which allows linking to the digital read out unit. A special plug is fitted with the connecting pins which are made from identical thermocouple material to that of the mating socket. This arrangement allows rapid fitting without sacrificing thermocouple conductor uniformity. The sheath allowed thermocouples to be correctly placed into the holes. Ball and Lorch [65] showed that soldering thermocouples on the strip of lamination can cause losses to increase locally by as much as 50%. It also allows the eddy current in the strip to set up transient voltages in the thermocouple circuit which seriously interfere with the thermal e.m.f. Thus the fit was strengthened using a special strength glue, of high thermal conductivity, which allowed excellent thermal contact to be obtained. In order to reduce the effects due to the variation of the magnetic fields in the vicinity, the connecting wires were twisted together to make the circuit non inductive.

3.4 Positioning of thermocouples in the test machine

The number of thermocouples required for measuring the loss density using the temperature time method is usually large and depends on the accuracy being sought, and the effect on the test motor magnetic circuit that may result as consequence of drilling the holes in the stator of the motor. Owing to the large number of thermocouples it was envisaged that the casing of the standard production motor would present a great obstacle to accurately locating and drilling the holes in the stator. An unwound squirrel cage motor, without the casing, was requested from Brook Crompton Parkinson Ltd., full details for the motor are given in appendix A.

For the motor it is desirable to select a scheme which optimises the physical placement of thermocouples. Such a scheme is based on a judgement as to the factors which are likely to contribute significantly to the generation of losses. For example, the flux distributions in the stator teeth are different from those in the back iron. Furthermore, to obtain a volumetric loss density distribution using interpolation techniques [68] the loss density distribution along the three cylindrical coordinate directions is required, viz, circumferential, radial and axial. In order to obtain the total iron loss, ideally, a three dimensional function (axial, radial, and circumferential) should be defined which can give the loss density at any point of the machine, and then integrated over the whole volume. The problem of nonlinearity which exists in machines, makes the determination of this function too difficult, if not impossible. A reasonable approach, owing to the large number of points at which the loss densities are to be calculated, and their distribution throughout the stator iron of the motor, is to divide the stator into two blocks, back iron and teeth. In view of the aforementioned considerations, three sections were selected for the measurement of loss density, as shown in Fig. 3.1. Two sections, $S1$ and $S3$, are located at the ends of the motor, whilst the third, $S2$, is positioned at the middle of the stator axial length. The thermocouples are identified by their numbers as indicated. The axial loss density distribution was to be determined at a constant angular position ($\theta = 90^o$ mech.degs), using thermocouples inserted at $\frac{L}{4}$ and at $\frac{3L}{4}$ at radii $r = 5.79cm$ and $7.49cm$ from the centre of the motor. In total sixty four thermocouples were placed in the stator core. To investigate the losses in the rotor three thermocouples were used; one in the rotor back iron, a second in the aluminium bar and a third at the surface of a tooth. The thermocouple extension wires were passed through an axial bore in the shaft and connected to silver slip rings encased in a strong fixing unit.

Since the motor did not have a casing drilling holes into the back iron to accom-

modate the thermocouples was not difficult. Drilling holes into the teeth from the stator bore, however, was not envisaged to be practical since grooves, which are along the length of the stator bore, would have to be introduced to accommodate the thermocouple extensions. Furthermore, the relatively small stator bore implied that machining of these grooves was not possible. The alternative was therefore to drill all holes from the outer stator surface.

For the rotor, the holes were drilled axially from the non-driven end, as shown in Fig. 3.2. The leads of the thermocouples in the rotor were led through a hollow extension of the main shaft and then connected to the rotating slip ring assembly attached to this shaft extension.

To minimise the introduction of any changes to the magnetic circuit all the holes were made as small as practically possible ($0.7mm$). The motor was sent to Brook Crompton for winding and assembly, followed by positioning and setting of the thermocouples in this department.

Due to the projection of the thermocouples leads from the stator body, it was not possible to fit the casing to the stator as is usual. Hence a test rig was developed which enabled the stator/rotor to be kept in position, whilst allowing all the thermocouple extension wires to be brought out from the stator. The test rig consisted of two aluminium rings to hold the laminations at both ends. The rings were secured rigidly using three stainless steel bars equally spaced around their circumference. To protect the end windings, three aluminium blocks were placed between the end plates and the stator core. The stator was then fixed to the test bed by means of specially designed mild steel supports. Once the stator had been positioned, the rotor was then put in place and the end plates secured using bolts. A photograph of the fully instrumented motor is shown in Fig. 3.3, while a schematic diagram of

the test motor assembly is shown in Fig. 3.4.

The test motor was mechanically coupled to a separately excited 5kW d.c. machine, which represented the load for the induction motor. As well as being operated in generating mode, the d.c. machine was also used to drive the induction motor.

3.5 Testing procedure

In obtaining measurements using the temperature time method the following conditions must be satisfied

- The motor must have reached a steady state temperature.
- The source of heat loss should be removed in as short a time as possible i.e. load and supply removed instantaneously.
- The speed of the test motor must remain constant after the removal of the source.

Fig. 3.5 shows a schematic diagram of the electrical circuit which enabled all the requirements to be satisfied simultaneously by activating a single switch.

The thermocouple outputs were monitored and converted to their corresponding temperatures using a 10 channel microprocessor based thermocouple unit. Reading of the thermocouple measurements were taken automatically every 10s over a period of time, and the data transmitted to a computer where it was stored. Each test run was made at least twice to establish the accuracy and repeatability of the results.

3.6 Results

During the experiment stage some thermocouples were inevitably destroyed whilst others went open circuit. The reminder of the thermocouples in the stator exhibited consistent readings, whereas readings obtained from the rotor thermocouples were erratic especially at the point of disconnection of the load, and the excitation, i.e. at the time of recording the data, which is crucial for accurate determination of loss density. Despite several attempts to improve the situation, the results for the rotor were inconsistent. Furthermore, it was found that due to the length of the tests, upto 4 hours to reach steady state conditions, the brushes on the slip rings tended to wear off. This resulted in poor contact between the brushes and slip rings from a lack of pressure. Moreover, the debris resulting from the wear of the brushes affected the contact between the slip rings and brushes and hence the small currents going through the contacts. Nevertheless, since slip frequencies in the rotor are small this leads to a negligible rotor iron loss and hence the rotor iron loss information is deemed not crucial for accurate determination of rotor temperature.

A typical temperature time profile obtained from a thermocouple located in a tooth is shown in Fig. 3.6. Based on the analysis given in section 3.2.1, the localised loss density can be determined by estimating the gradient at $t = 0$, corresponding to switching off the supply to the induction motor. The temperature time data can be approximated using either a linear or exponential function, whichever gives a better fit, from which the gradient can be calculated. By using this procedure, the circumferential, axial and radial distributions of loss densities can be determined.

A series of tests were conducted under full, half, and light load conditions to obtain loss density distributions for incorporation into the lumped parameter thermal model, to be described in the next chapter.

3.6.1 Circumferential loss density distribution

Figs. 3.7a, 3.7b, and 3.7c show the circumferential loss density distribution in the three transverse sections S_1, S_2 and S_3 for the motor under a full load conditions. Repeated measurements show that the variations are within $\pm 6\%$ of these curves. From the graphs, it is apparent that the loss density is highest in the teeth, as expected.

Several factors could have contributed to the higher loss density in the teeth. One of the major components is the surface losses. These losses constitute a large component of losses and arise as consequence of the small airgap which is made as small as possible in order to keep down the magnetising current in induction motors. Owing to the variation in the reluctance caused by the slotting the flux density at any point on the stator surface will vary as the rotor rotates. This induces eddy currents at the surface of the teeth which generate surface losses. Moreover, the presence of the slots causes the flux to vary from the radial direction when the teeth are opposite each other, to a partly tangential direction in the surfaces of the teeth as a tooth is opposite a slot. The iron in this region is therefore undergoing an elliptical cycle of magnetisation at tooth frequency resulting in surface losses [40]. In addition, harmonic losses due to phase belt and slot harmonic fields which are confined to the surface of the tooth.

There is a variation of loss density in the teeth, particularly pronounced in sections S_1 and S_2. This may be due to the effect of the axial component of the end leakage flux, which induces additional losses at each end of the stator. Moreover, since the average iron loss is approximately proportional to the square of the flux density, it seems likely that the extra flux density is due to skew effect which is maximum at the ends of the core, and would give rise to increased core losses.

In general the figures show that, taking into account of the errors margins $\pm 6\%$, the stator loss density distribution is relatively uniform.

3.6.2 Axial loss density distribution

Fig. 3.7d shows the variation of loss density along the axial direction at the stator teeth and back iron. From analysing the curves, it can be observed that there is an increase in loss density with the increase of distance from the centre of the motor. This reflects the skewing effect which produces an increase in radial flux density, and increases with distance from the centre. Consequently, it produces a corresponding iron loss in the stator core and teeth at fundamental frequency. Of special interest is Table 3.2 where the average loss densities in the teeth and back iron are given for the three sections. In both the teeth and back iron the middle section loss density is smaller than the outer sections.

The loss densities in the teeth are more pronounced, especially at the ends of the core where the factors, described in previous section, contributed to the increase of losses in this region.

3.6.3 Radial loss density distribution

Figs. 3.7e, 3.7f, and 3.7g show the variation of the loss density in the radial direction for the three sections S_1, S_2 and S_3. It can be seen that for all the sections, the loss density is highest in the teeth and decreases progressively towards the outer periphery of the back iron. Obviously flux densities are higher in the teeth and as the flux is more disturbed additional losses are expected. It can be observed that, in general, there is an increase in loss density in the end sections over the middle, which can be a consequence of end leakage and skew effects stated in the above two sections.

At half load the loss density distributions for the different sections in Figs. 3.8a-g. The curves in general follow the same trend as those of the full load test. It can be observed that, apart from the value of loss densities being lower than those at full load, the machine is almost under the same conditions as at full load.

At light load, however, the loss density distributions shown in Figs. 3.9a-g, the curves show some differences from the two other load conditions. The feature which is most dominant, is that the loss densities at the end sections are slightly lower than the middle section in the axial direction. This is may be due to the weaker effects of end leakage losses. This may be attributed to the fact that the temperatures in the machine for this load condition were relatively low, and sampling time for the temperature time curve was too short. Hence, in combination with the low accuracy readout from the data logger, (one decimal place), the result could be practically inaccurate.

Based on the localised loss density distributions, average loss densities can be determined. These are shown in Table 3.2 where Q_{S1}, Q_{S2} and Q_{S3} are the average loss

densities in the sections $S1$, $S2$ and $S3$ respectively, while Q_S is the overall average loss density of the three sections. From the tabulated results it can be seen that the average loss density in the teeth increases substantially with load whereas in the back iron the increase is relatively small. This is predominantly due to the existence of large harmonic fluxes which are generated as a consequence of the machine being loaded. The harmonic fluxes produced by the induced rotor currents, cause increased stator teeth surface losses. For light loads, however, the effects of stray load losses are negligible. Hence, loss densities in the teeth and back iron are now almost of the same magnitude.

Sections	$Q_{S1}(W/m^3)$ $\times 10^{-6}$	$Q_{S2}(W/m^3)$ $\times 10^{-6}$	$Q_{S3}(W/m^3)$ $\times 10^{-6}$	$Q_S(W/m^3)$ $\times 10^{-6}$	Losses (W)	%
Full load test						
Back iron	0.0667	0.0487	0.0491	0.0527	83	69.7
Teeth	0.1222	0.0720	0.1044	0.1060	36	30.3
Half load test						
Back iron	0.0521	0.0398	0.0378	0.0414	69	75
Teeth	0.0679	0.0545	0.0652	0.0652	23	25
Light load test						
Back iron	0.0449	0.0463	0.0348	0.0403	72	78.3
Teeth	0.0477	0.0512	0.0520	0.0548	20	21.7

Table 3.2: Loss density in the transverse sections for different load conditions

The iron loss of each block is calculated by multiplying the average loss density by the total volume of that block, as shown in Table 3.2, and the overall iron loss is then obtained by summing the back iron and teeth losses.

Loss density is estimated from the initial gradient of the temperature time characteristic and, hence, is a function of the sampling period. To assess the effect of sampling period the temperature time measurements were made for various sampling periods. Table 3.3 shows the total calculated losses for different sampling periods.

Total iron losses ($Watts$)			
Methods in use	F. load	H. load	light load
Temperature time ($20s$)	119	92	92
Temperature time ($30s$)	140	102	96
Temperature time ($40s$)	163	110	99
Temperature time ($60s$)	197	119	106

Table 3.3: Total iron losses for different sampling periods

Theoretically, to obtain the loss density measurement accurately, the readings must be taken over an infinitely short time. The minimum practical sampling period is limited to 20 seconds, since below this the thermocouples' readout is not sufficiently accurate to measure the change in temperature, particularly under light loads. The sampling period of $20s$ resulted in a better agreement with the other methods as shown in Table 3.4, and was used for subsequent measurements, (iron losses determined using equivalent circuit is described in detail in Appendix A). For longer sampling periods, the measurements are less accurate, because of the errors introduced when calculating the initial gradient of the temperature time curves which are due to heat diffuse to or from parts. Ross [64] measured the losses in the core of a synchronous machine using the temperature time method. The interval between data readings was about 40 s over a period of 240 s.

Method in use	Total iron loss at load ($Watts$)
Manufacturer's	110
Standard equivalent circuit	118
Temperature time ($20s$)	119
Temperature time ($30s$)	140
Temperature time ($40s$)	163
Temperature time ($60s$)	197

Table 3.4: Total iron losses using different methods

3.7 Discussions

Of special interest in the results for the loss density distribution is the difference between the full load and light load losses which are defined as the stray load losses. For the test machine, the stray load losses were approximately 27W, which is approximately 3.2% of the total losses or 0.68% of the rated output power of the motor (appendix A). Table 3.5. compares the stray load losses obtained from various sources. It can be seen that, compared to empirical methods, the temperature time method represents a more reliable and accurate method for stray loss estimation.

Source	Stray load losses ($Watts$)	Method of calculation
Manufacturer's	25	-
BS 4999 [41]	20	0.5% of the rated output power
Schwarz [12]	84.3	10% of total losses
ANSI [57]	48.0	1.2% of the rated output power
Temperature time method	27.0	0.68% of rated output power
Temperature time method	27.0	3.2% of total losses

Table 3.5: Stray load losses from various recommendations

3.8 Conclusions

Loss density distributions were obtained at different sections, and under different load conditions, for a 4kW induction motor. Similar profiles were observed for both full load and half load tests. However, for light load test the curves are slightly different owing to the different conditions which the test motor is under. For an accurate determination of local loss density a short sampling period is necessary so that the initial gradient of the temperature time characteristic can be calculated

correctly. This implies that accurate instrumentation is necessary to measure small changes in temperature.

The provision of volumetric loss density distribution data would open the way for researchers to investigate in greater detail the nature of some loss components due to skew and end leakage. The information gathered may be used for the production of future designs and to corroborate, or otherwise, previous published works on the subject.

The experimental difficulties in the investigation of stray load losses not only lie in the complexity of the measuring method but also in the requirement of high measurement accuracy. The temperature time method presents a very powerful technique for investigating losses in general, and stray load losses in particular, and this has been validated by a good correlation with the stray load losses obtained using recommended value of British Standard [41].

Despite all the practical difficulties, the temperature time method shows great potential for gaining valuable information on the volumetric iron loss distribution within the motor. This is of prime importance for the accurate prediction of temperature rise in machines.

Stray load losses contribute to the heating of the various components of a machine but there is very little literature to show the correlation of heating effects with the magnitude of stray load losses. Schwarz [12], however, noted that additional losses of the order of 1.5% to 2% of the rated output in a large high efficient machine, would have a marked effect on the heating performance. However, for small machines where the efficiency levels are considerably lower, high stray load losses would go undetected by virtue of their relatively small effect on heating. The temperature

time method is a powerful tool by which stray load losses can be determined, and thus their heating effects on the machine can be checked. These two major issues will be treated in the next chapter.

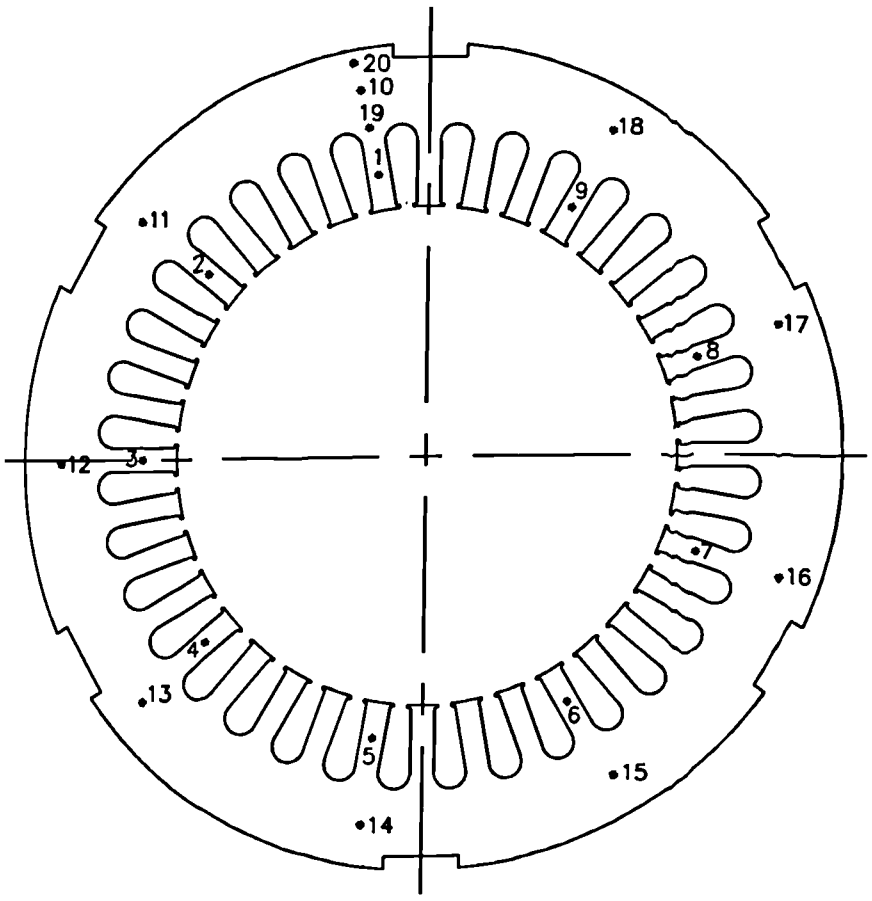

(a) Transverse section S1

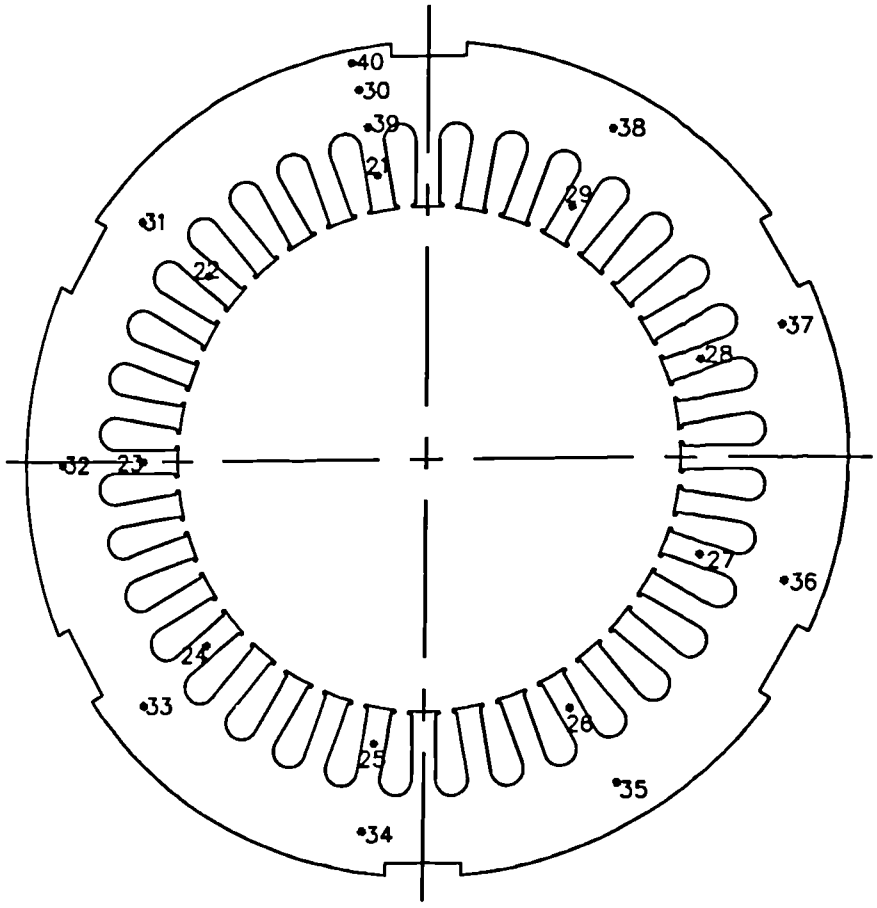

(b) Transverse section S2

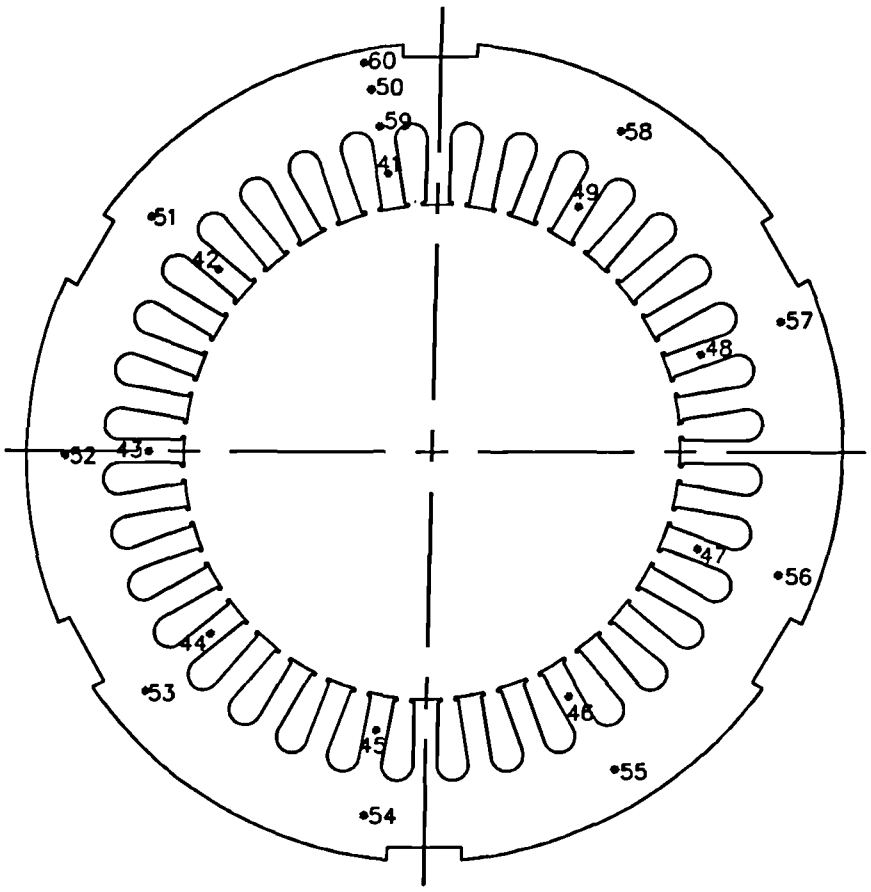

(c) Transverse section S3

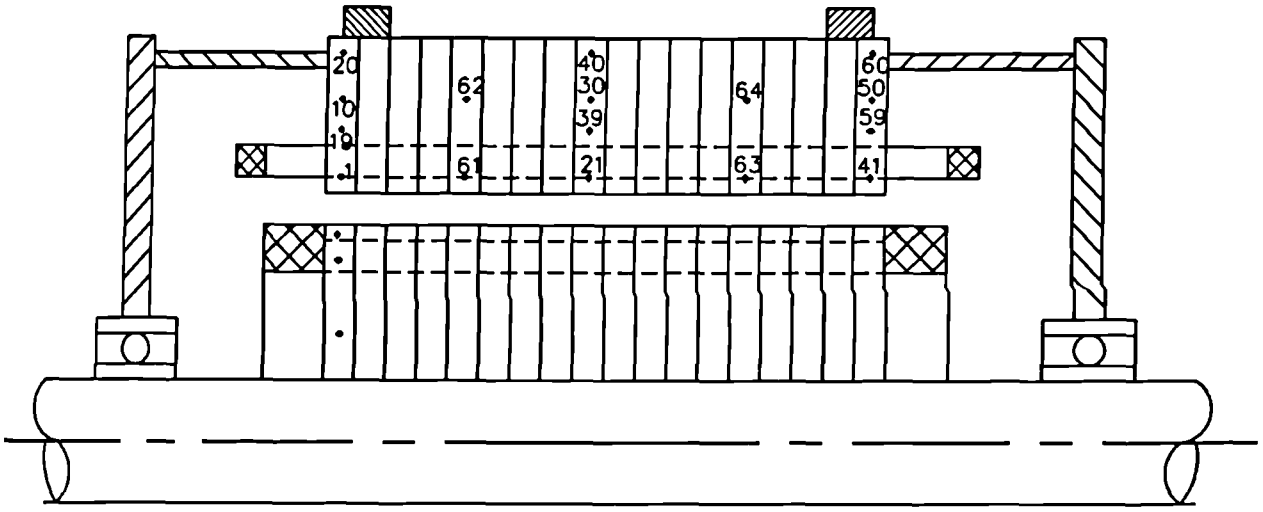

(d) Axial section S4

Fig. 3.1 Thermocouples placement within the test motor.

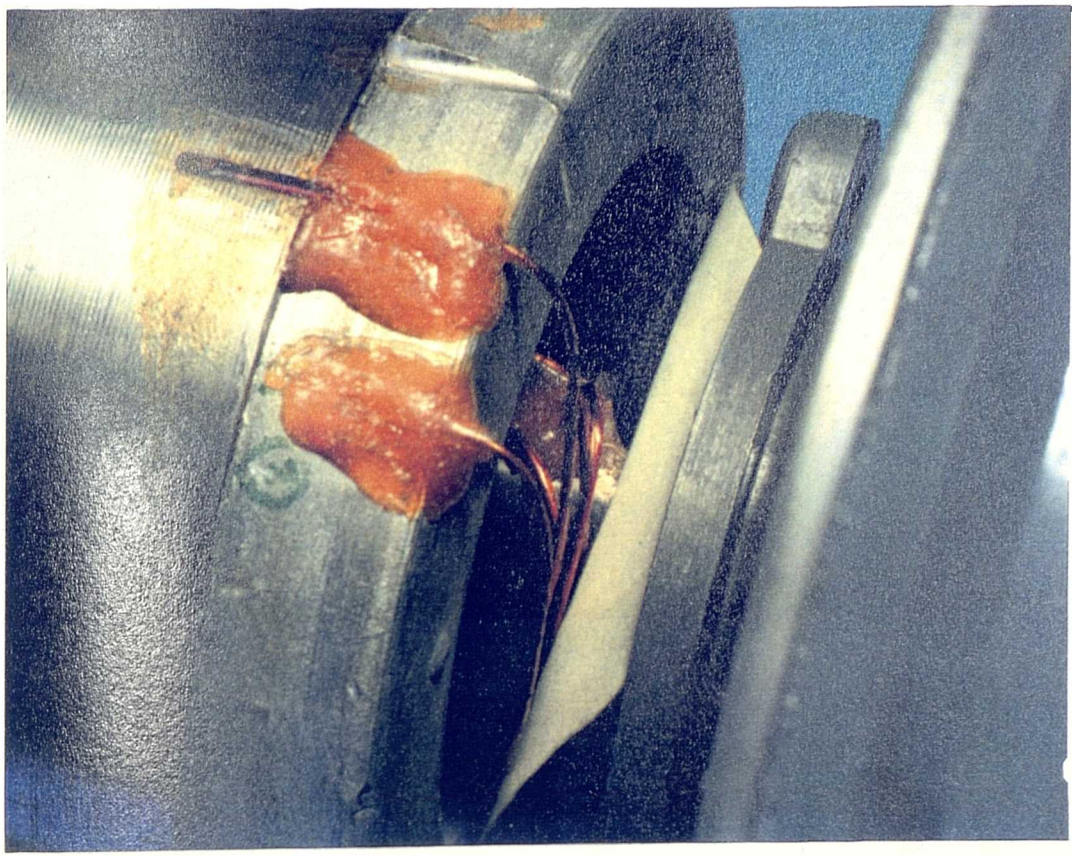

Fig. 3.2 Photograph of the rotor showing the thermocouple placement.

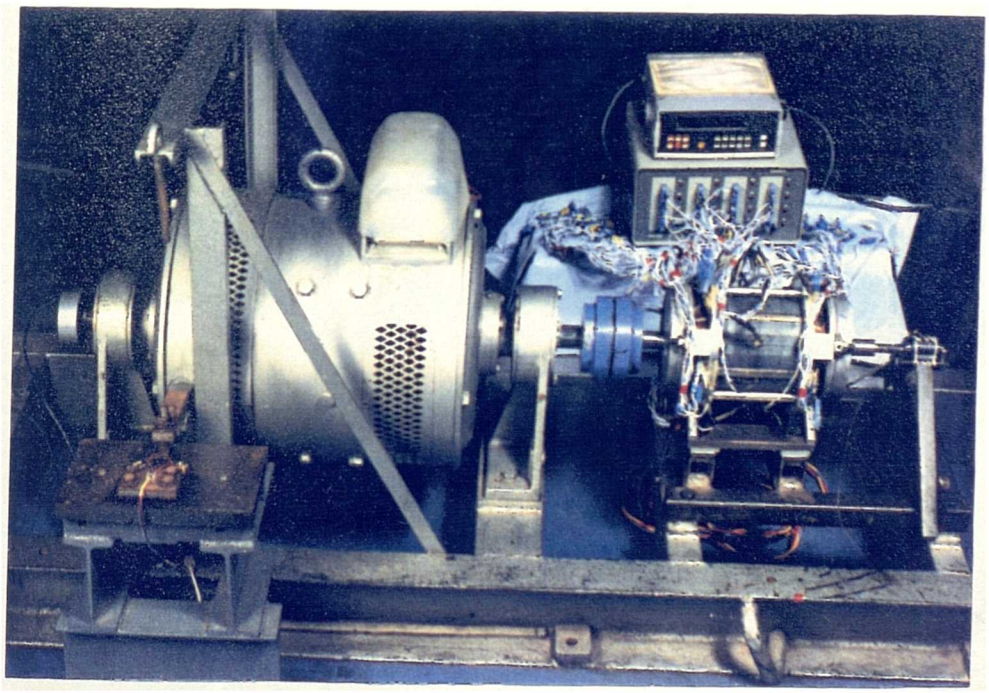

Fig. 3.3 Photograph of the fully instrumented test motor.

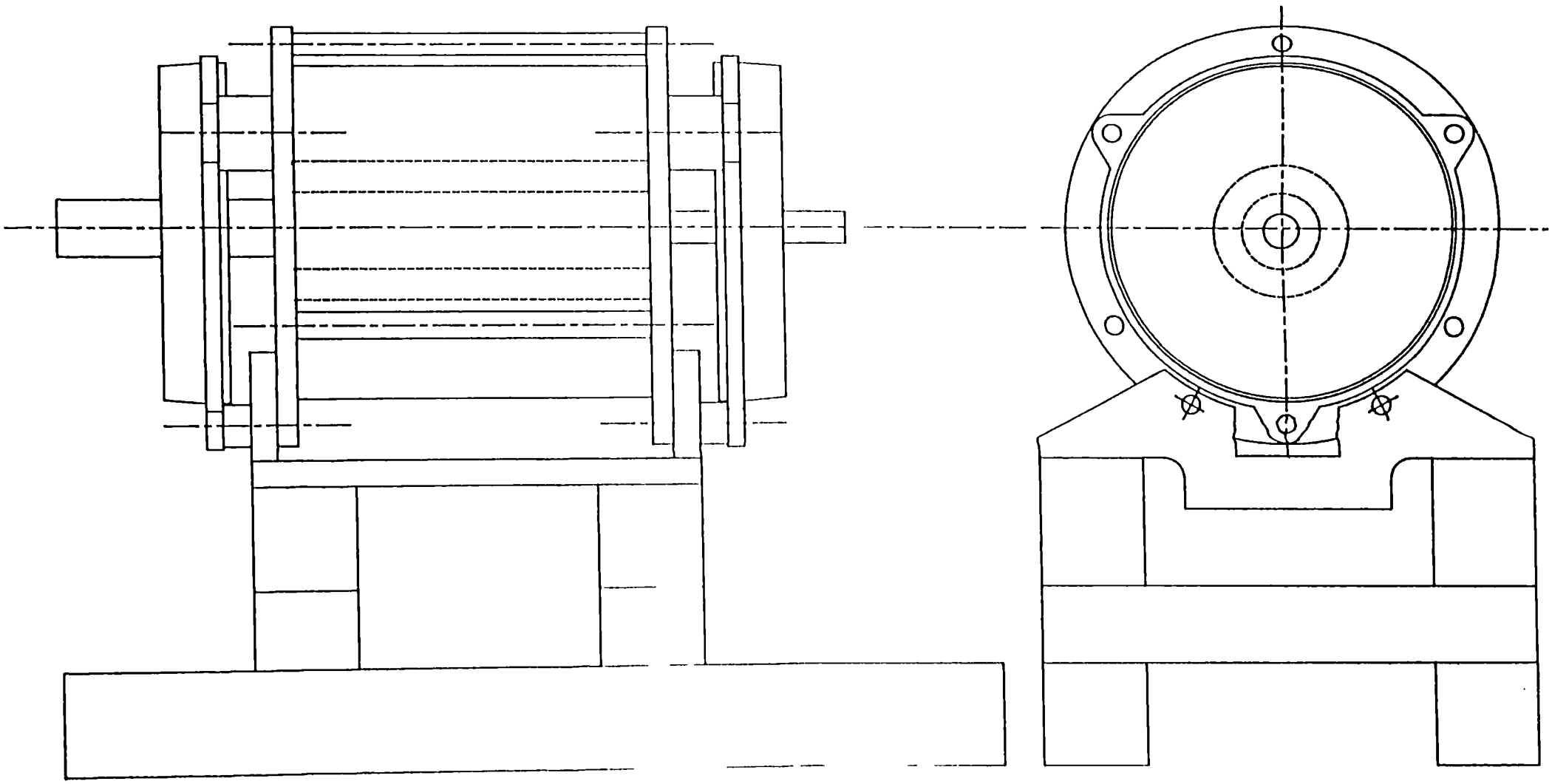

Fig. 3.4 Illustrative representation of test motor assembly.

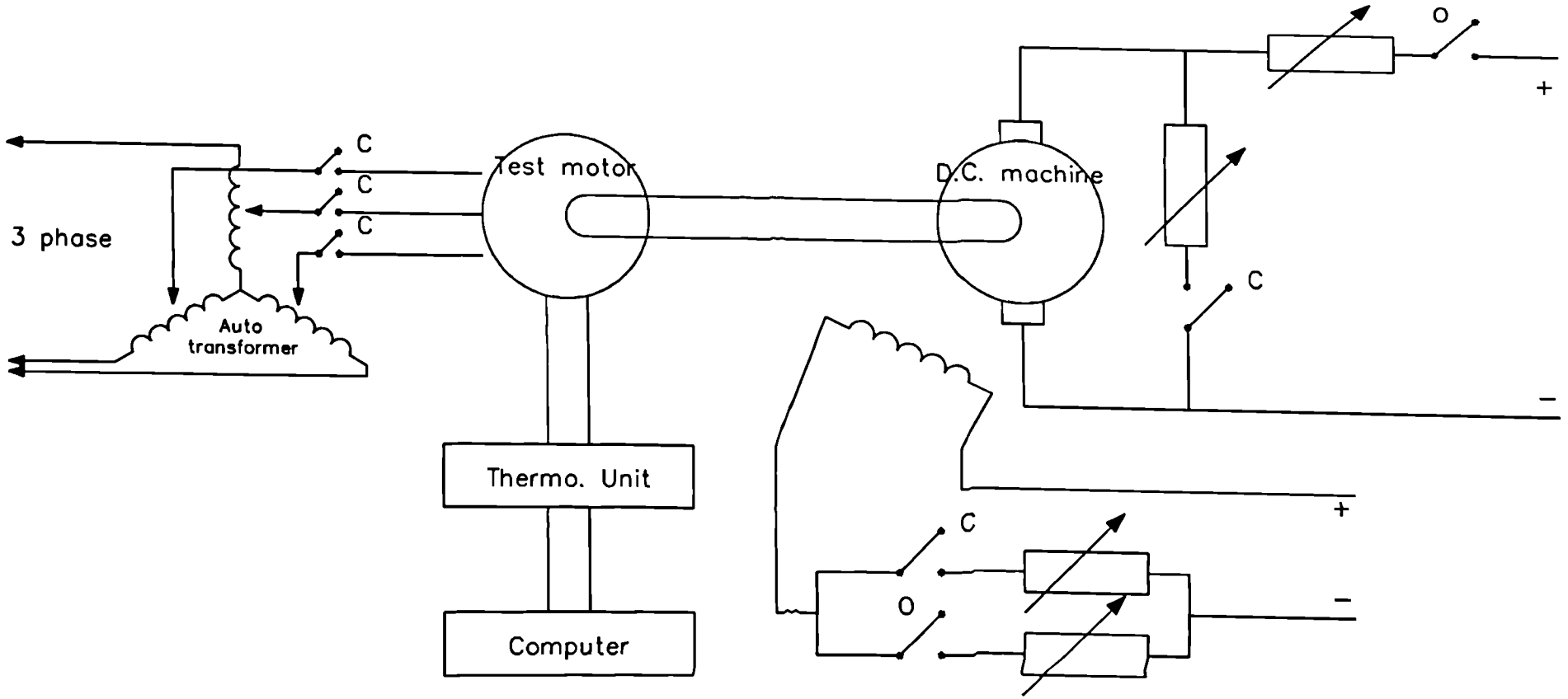

Fig. 3.5 Schematic diagram of the test rig.

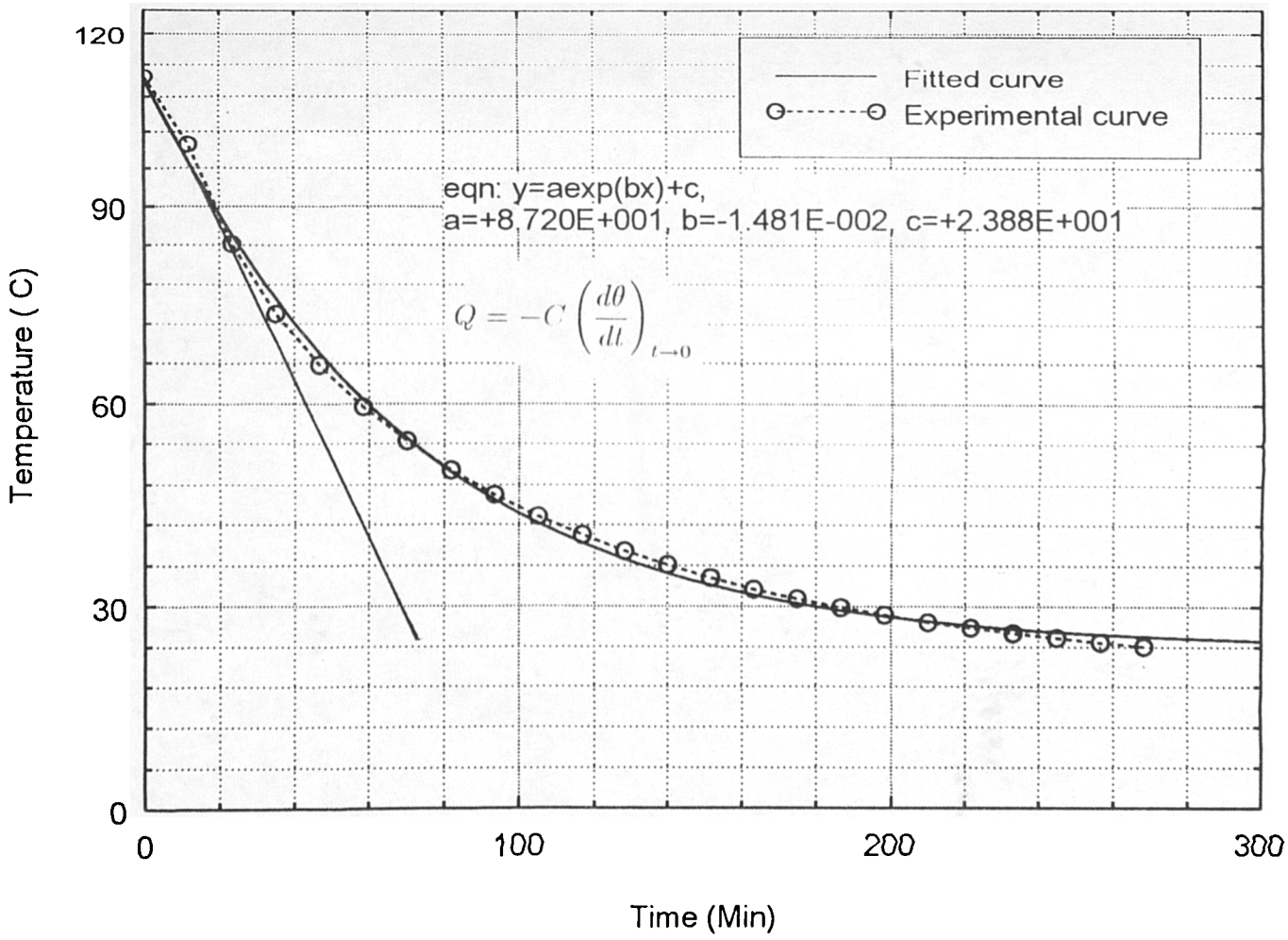

Fig. 3.6 Typical temperature time characteristic for a thermocouple embedded in tooth

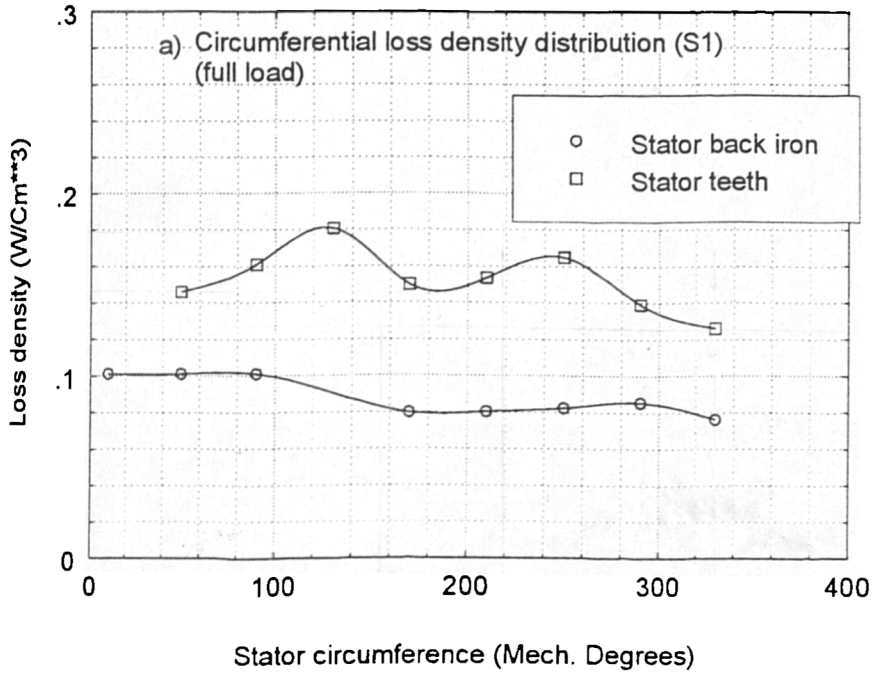
a) Circumferential loss density distribution (S1)
(full load)
Stator back iron
Stator teeth
Loss density (W/Cm**3)
.3
.2
.1
0
0
100
200
300
400
Stator circumference (Mech. Degrees)

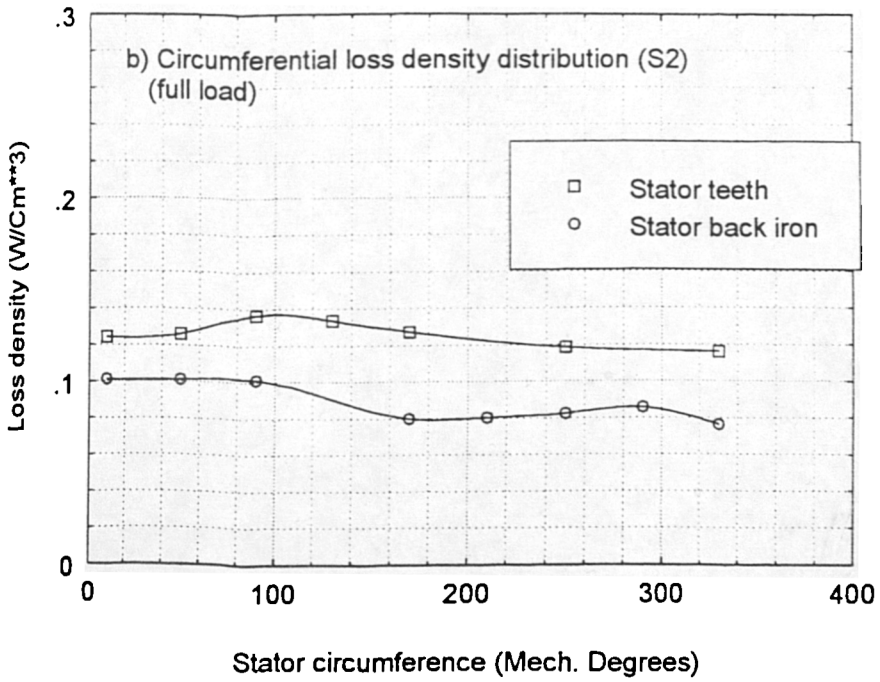
b) Circumferential loss density distribution (S2)
(full load)
Stator teeth
Stator back iron
Loss density (W/Cm**3)
.3
.2
.1
0
0
100
200
300
400
Stator circumference (Mech. Degrees)

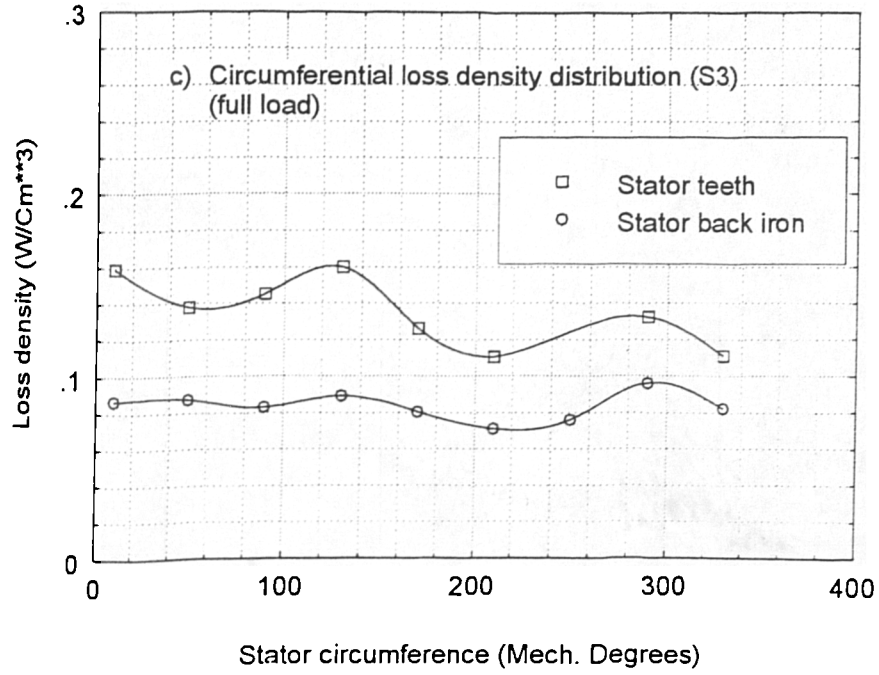
c) Circumferential loss density distribution (S3)
(full load)
Stator teeth
Stator back iron
Loss density (W/Cm**3)
.3
.2
.1
0
0
100
200
300
400
Stator circumference (Mech. Degrees)

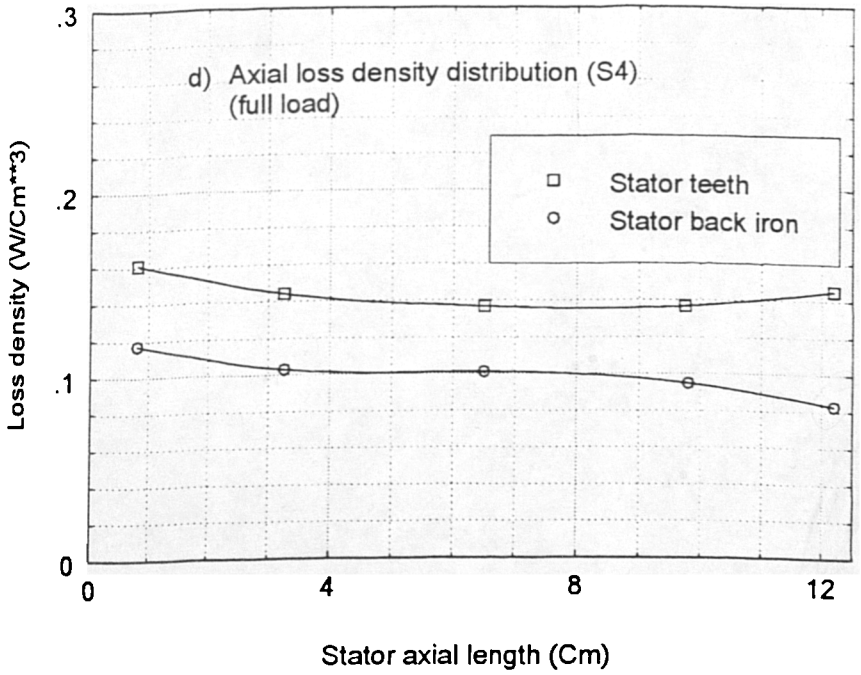
d) Axial loss density distribution (S4)
(full load)
Stator teeth
Stator back iron
Loss density (W/Cm**3)
.3
.2
.1
0
0
4
8
12
Stator axial length (Cm)

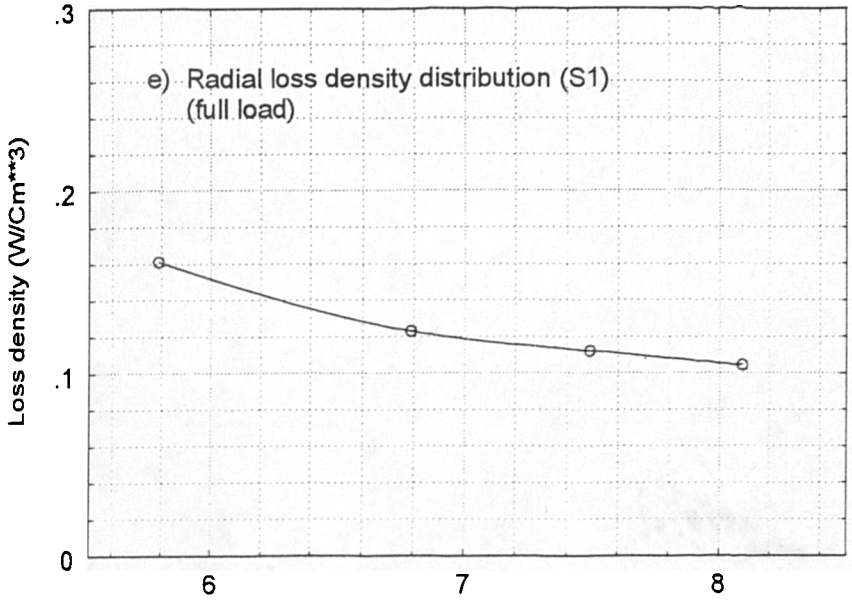
e) Radial loss density distribution (S1)
(full load)
Loss density (W/Cm**3)
.3
.2
.1
0
6
7
8
Stator radial distance from the centre of the motor (Cm)

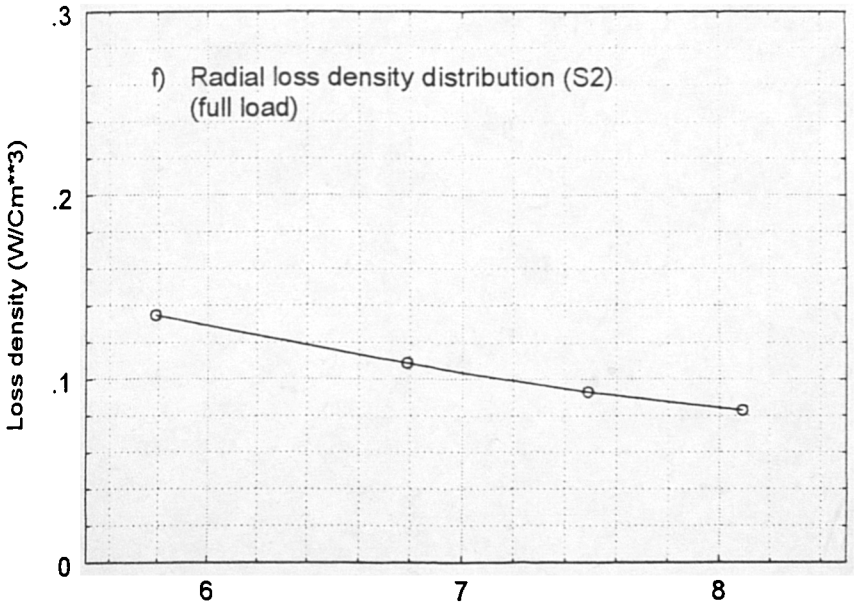
f) Radial loss density distribution (S2)
(full load)
Loss density (W/Cm**3)
.3
.2
.1
0
6
7
8
Stator radial distance from the centre of the motor (Cm)

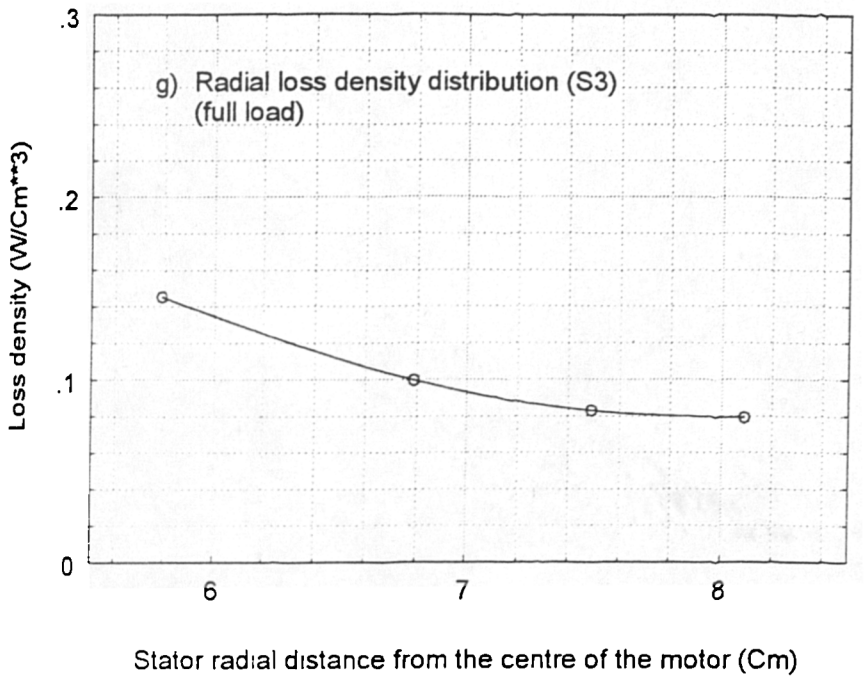

Fig. 3.9a-g Loss density distribution in induction motor (full load).

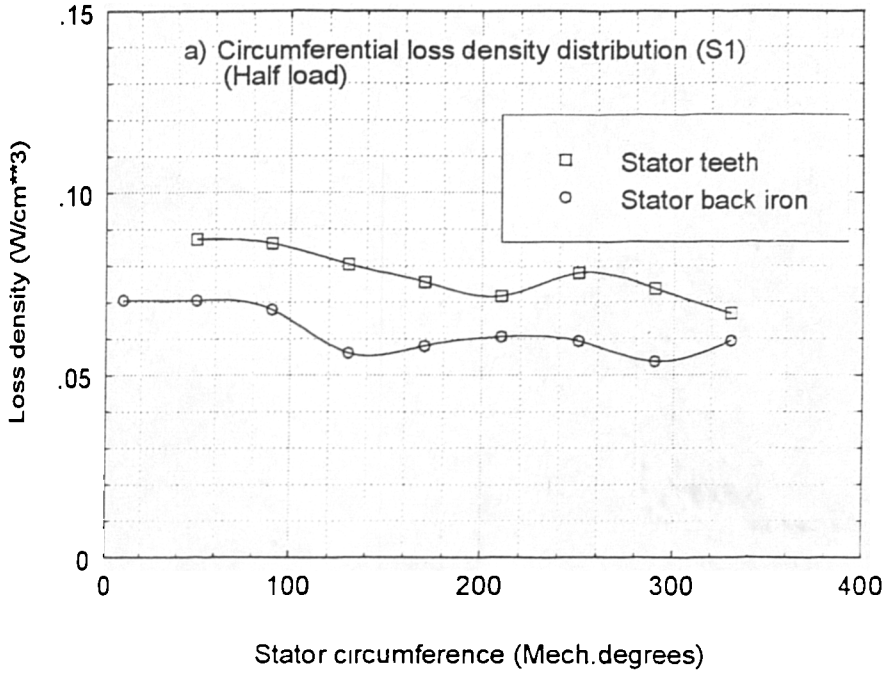
a) Circumferential loss density distribution (S1)
(Half load)
Stator teeth
Stator back iron
Loss density (W/cm**3)
.15
.10
.05
0
0
100
200
300
400
Stator circumference (Mech.degrees)

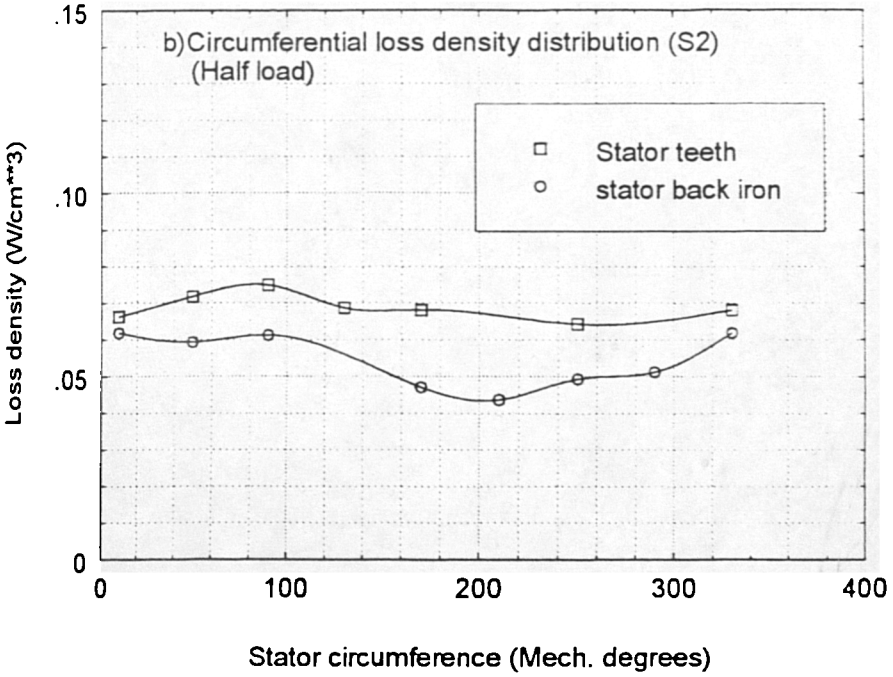
b)Circumferential loss density distribution (S2)
(Half load)
Stator teeth
stator back iron
Loss density (W/cm**3)
.15
.10
.05
0
0
100
200
300
400
Stator circumference (Mech. degrees)

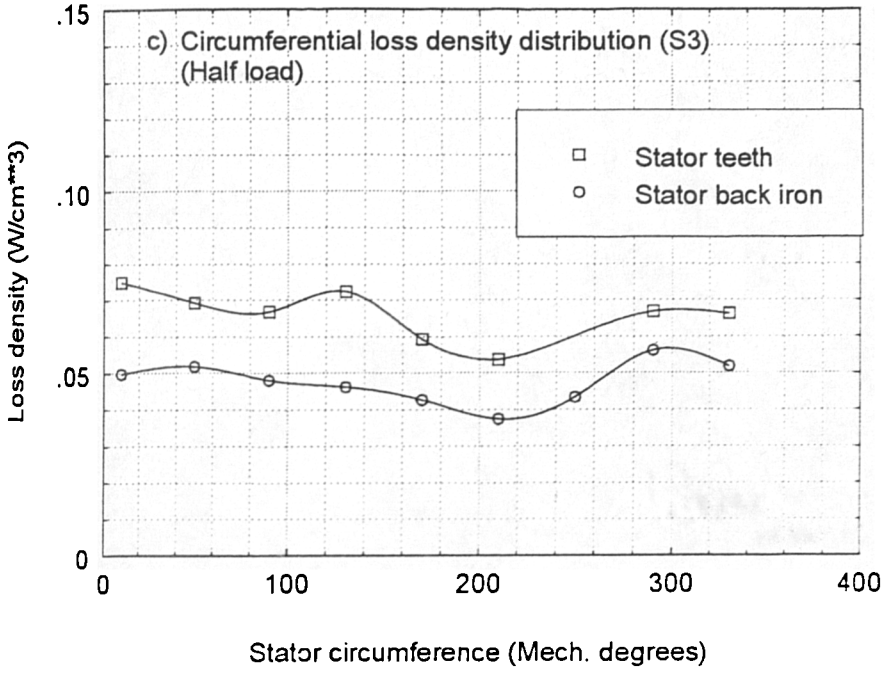
c) Circumferential loss density distribution (S3)
(Half load)
Stator teeth
Stator back iron
Loss density (W/cm**3)
.15
.10
.05
0
0
100
200
300
400
Stator circumference (Mech. degrees)

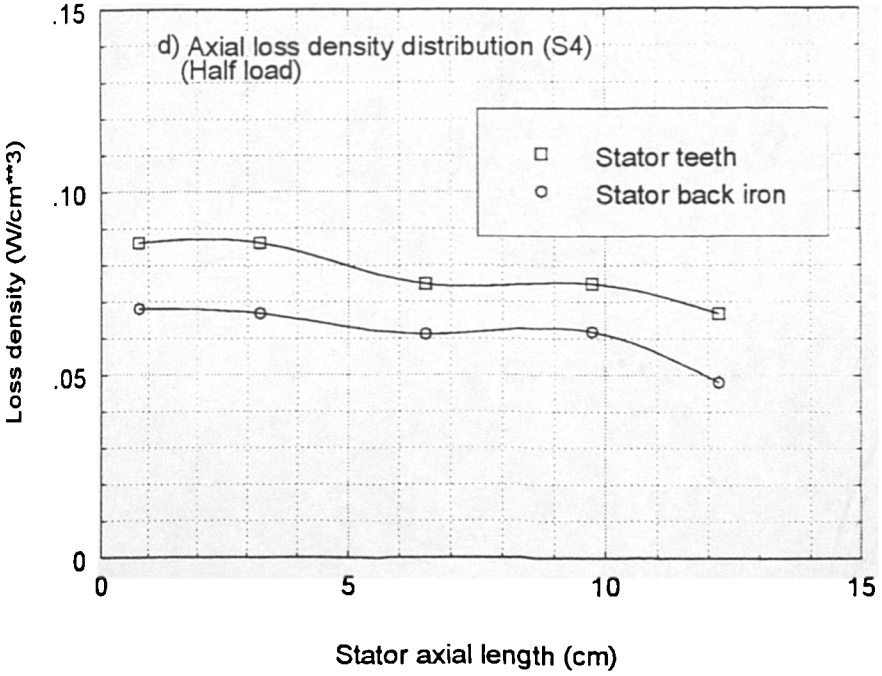
d) Axial loss density distribution (S4)
(Half load)
Stator teeth
Stator back iron
Loss density (W/cm**3)
.15
.10
.05
0
0
5
10
15
Stator axial length (cm)

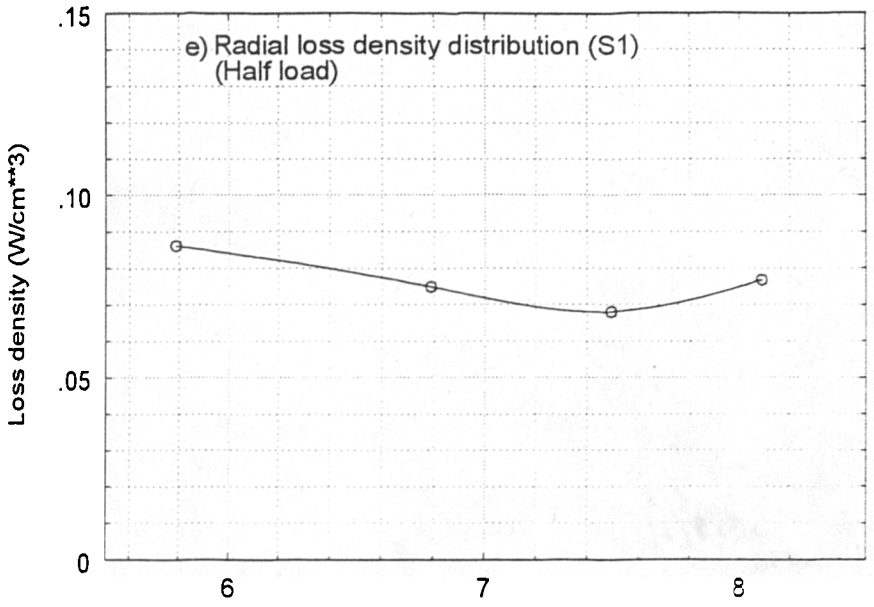
e) Radial loss density distribution (S1)
(Half load)
Loss density (W/cm**3)
.15
.10
.05
0
6
7
8
Stator radial distance from the centre of the motor (cm)

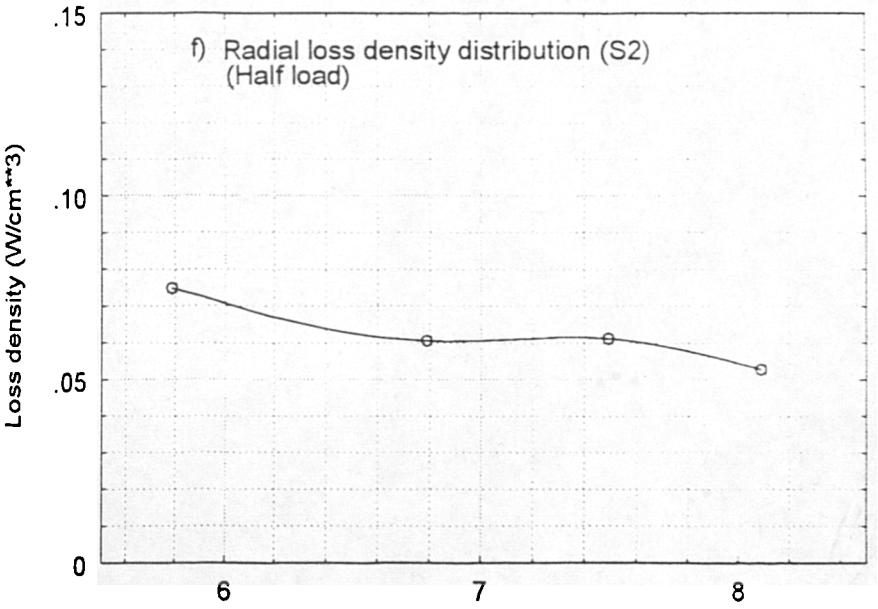
f) Radial loss density distribution (S2)
(Half load)
Loss density (W/cm**3)
.15
.10
.05
0
6
7
8
Stator Radial distance from the centre of the motor (cm)

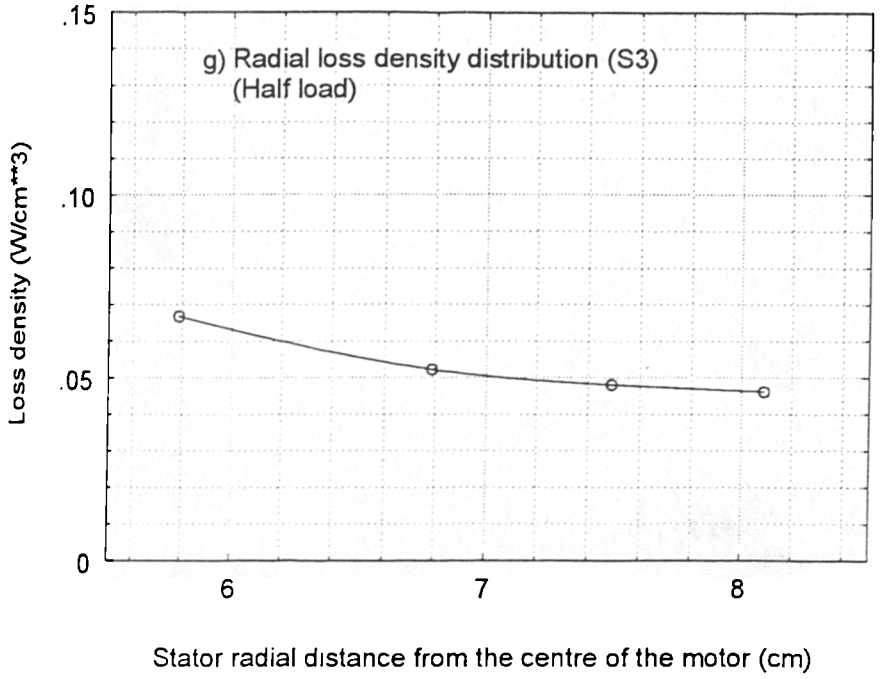

Fig. 3.8a-g Loss density distribution in induction motor (half load).

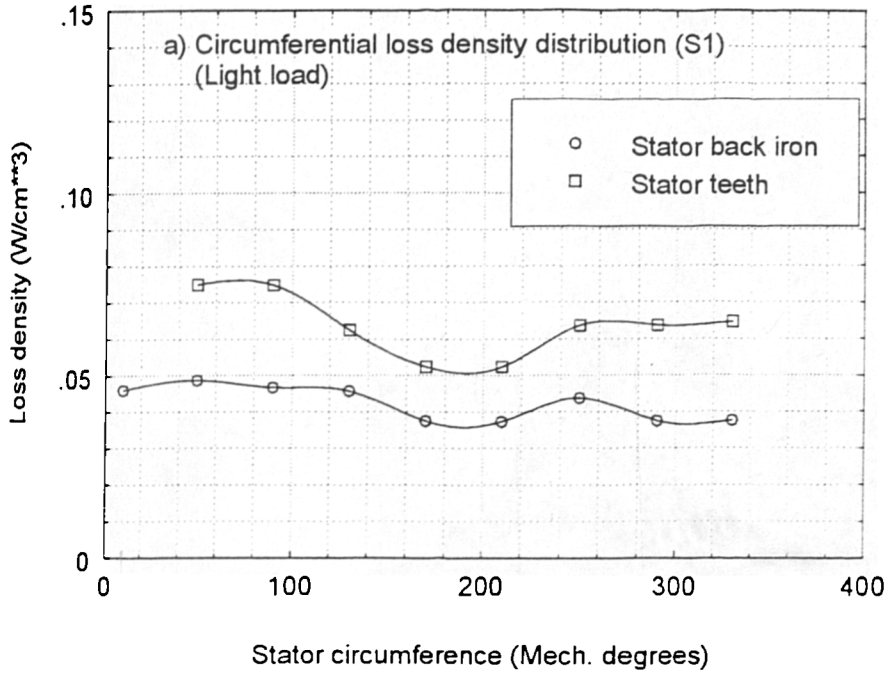
a) Circumferential loss density distribution (S1)
(Light load)
Stator back iron
Stator teeth
Loss density (W/cm**3)
.15
.10
.05
0
0
100
200
300
400
Stator circumference (Mech. degrees)

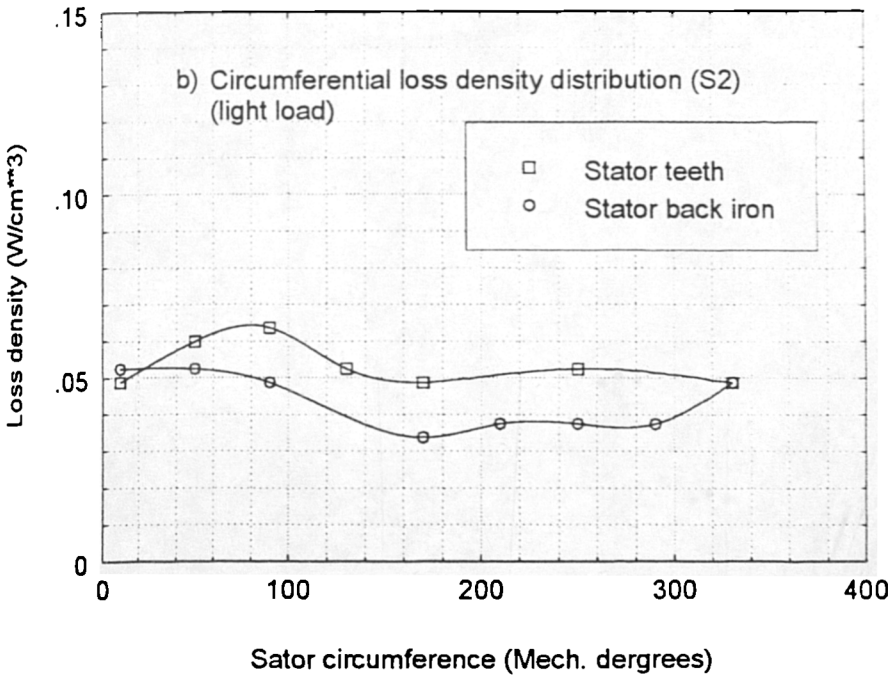
b) Circumferential loss density distribution (S2)
(light load)
Stator teeth
Stator back iron
Loss density (W/cm**3)
.15
.10
.05
0
0
100
200
300
400
Sator circumference (Mech. dergrees)

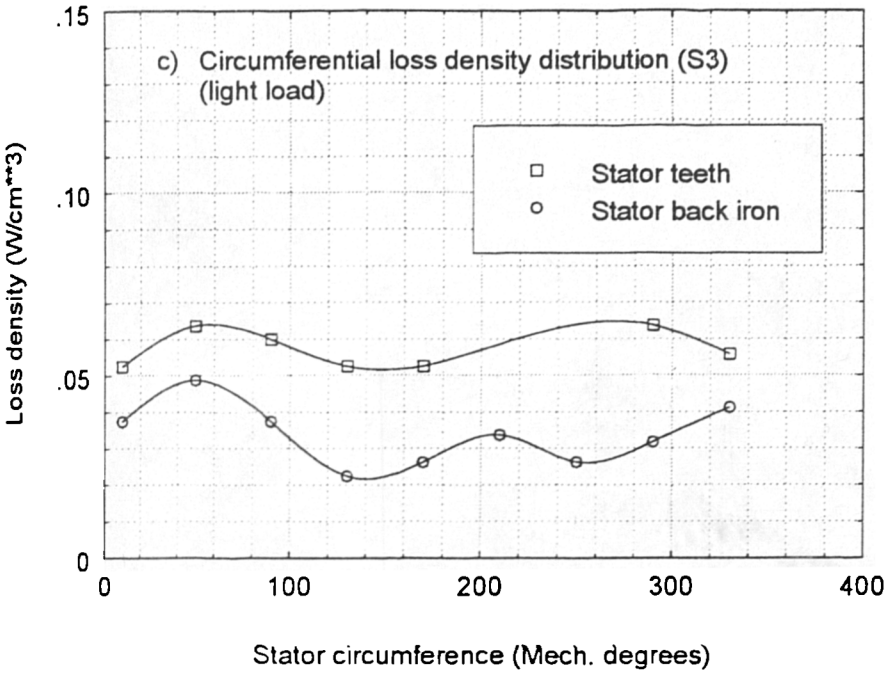
c) Circumferential loss density distribution (S3)
(light load)
Stator teeth
Stator back iron
Loss density (W/cm**3)
.15
.10
.05
0
0
100
200
300
400
Stator circumference (Mech. degrees)

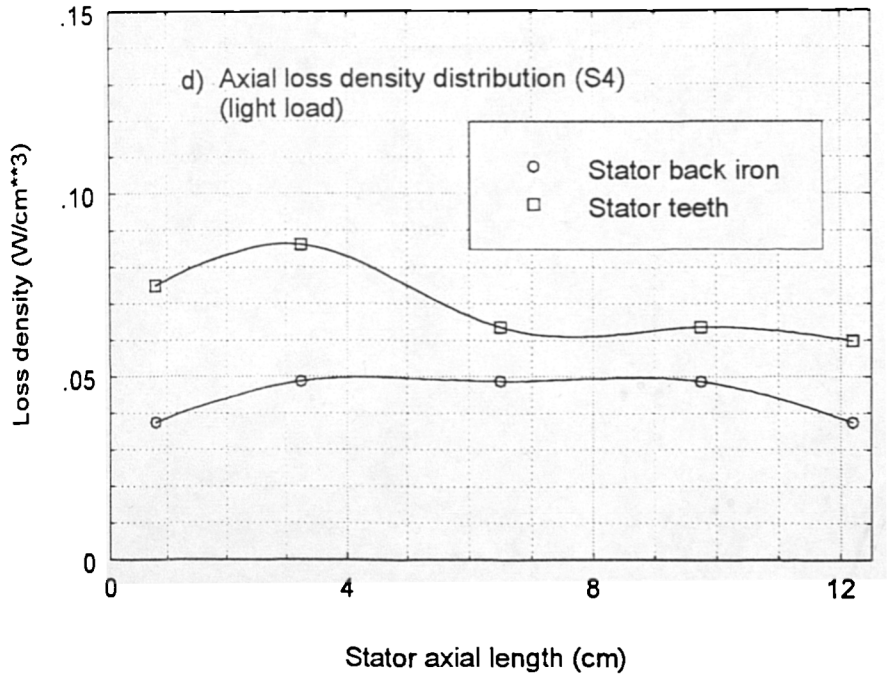
d) Axial loss density distribution (S4)
(light load)
Stator back iron
Stator teeth
Loss density (W/cm**3)
.15
.10
.05
0
0
4
8
12
Stator axial length (cm)

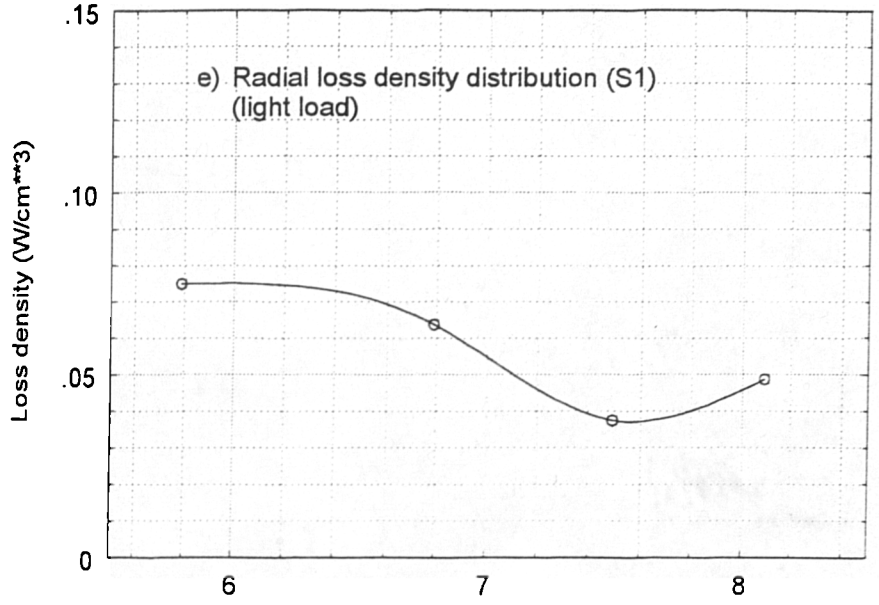
e) Radial loss density distribution (S1)
(light load)
Loss density (W/cm**3)
.15
.10
.05
0
6
7
8
Stator radial distance from the centre of the motor (cm)

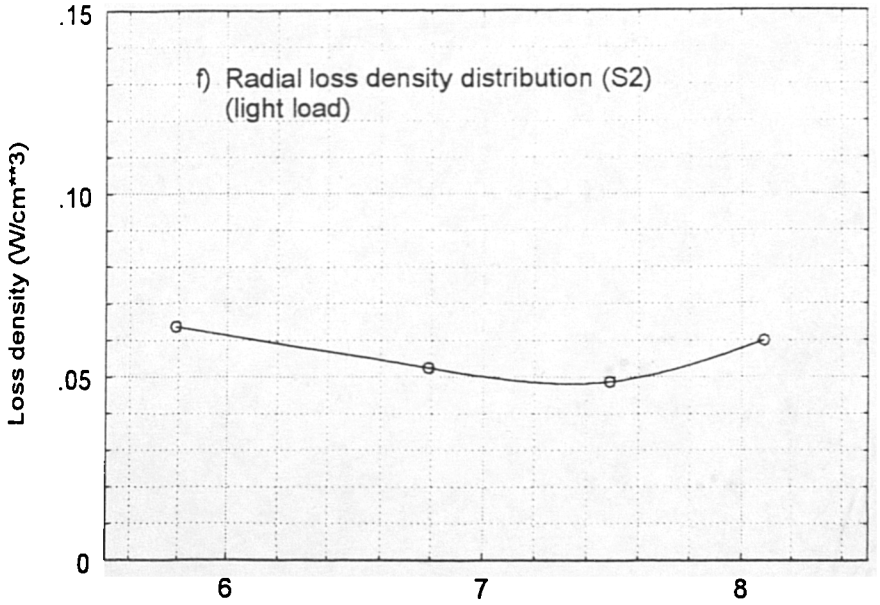
f) Radial loss density distribution (S2)
(light load)
Loss density (W/cm**3)
.15
.10
.05
0
6
7
8
Stator radial distance from the center of the motor (cm)

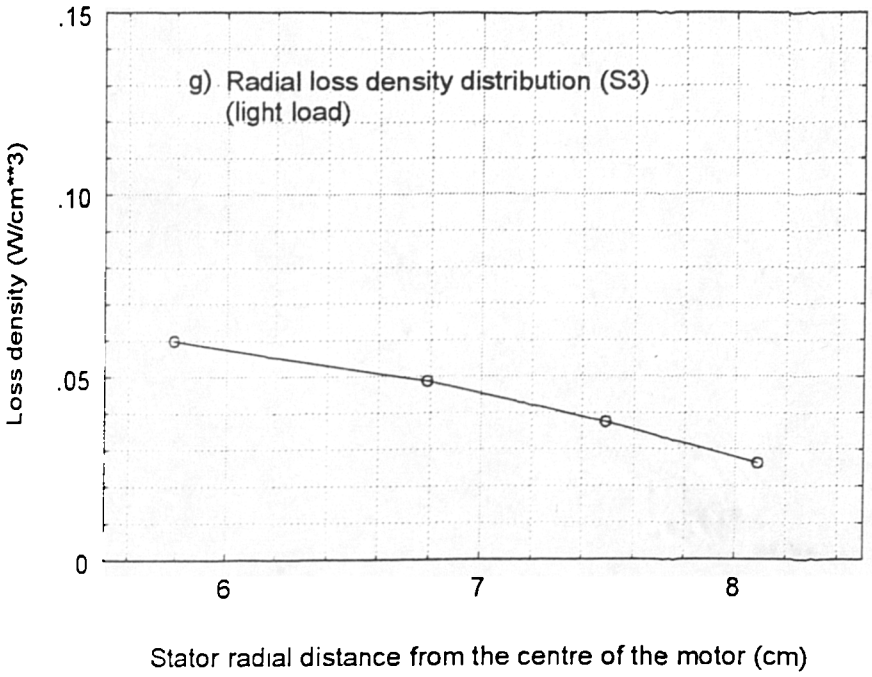

Fig. 3.7a-g Loss density distribution in induction motor (light load).

Chapter 4

Thermal modelling of induction motors

4.1 Introduction

A rotating electrical machine is a nonhomogeneous heat exchanger with temperature limitations, complex conducting paths and thermal barriers. The temperature rise is frequently the limiting parameter in determining the maximum rating from a given machine frame size. Two principal factors determine the temperature rise. First, the total iron and copper losses, and second, the efficient dissipation of heat. In the past, heating problems were usually solved by adding more active material to the machine, that is increasing the dissipating area by means of fins, or equipping the machine with bigger fans. However, in recent years the demand has been for high power to weight ratios. In addition, industry is beginning to scorn the high noise level inherent with the use of bigger fans. Under these circumstances, it is therefore imperative that better techniques for predicting temperatures within machines are

available.

As performance specifications, in term of efficiency and power density, become more demanding, so does the need for better thermal, electromagnetic and mechanical design strategies. Thermal design, however, has tended to lag behind other aspects of machines design, due to the fact that this is a complex study, involving the fluid mechanics, heat transfer and electrical behaviour of the machines. This is compounded by the fact that an electrical machine is itself a complex system consisting of different materials and distributed heat sources.

Early attempts at the prediction of the temperature rise in machines were largely based on empirical formulae derived from temperature measurements obtained from tests. The effects of insulation and air flow on the thermal performance of the machine were not fully understood, and hence, the prediction were largely unsuccessful [33].

To date, written material deals mainly with very large machines where losses can be calculated with relative accuracy [22]. Little, however, has been done towards developing accurate and comprehensive methods for calculating heating in small machines despite the fact that the analysis methods developed for estimating heating and dissipation in large machines are not well suited for small machines [22]. In addition the general construction of large machines, particularly with regards to their ventilating systems, differ considerably from smaller machines and, hence, the same analysis cannot be adopted directly for small machines.

Thermal models fall into two categories; those that use numerical techniques such as finite element and finite difference methods, and those that use lumped parameters. For numerical methods the machine is represented by dividing a 2-D or 3-D

section into a large number of small regions. These are interconnected at nodes, which may be arranged along grid lines, as in the finite difference technique, or in almost arbitrary arrangements, as in the finite element scheme. Simple functions are chosen to approximate the variation of the temperature over each region and the temperature is modified iteratively until the distribution satisfies the governing partial differential equations. Robert [33], and Tindall et al [69] applied three dimensional finite difference method for a large salient pole synchronous generator, taking into account the axial heat flow in the copper, and the effects of changing air and copper temperatures. Armor [36] and Sarkar et al [38] introduced three dimensional finite element models for solving heat flow equations to give the steady state temperature distribution in the stator cores of large turbine generators. A finite element solution of the three dimensional transient heat conduction equation in cylindrical polar coordinates, using arch shaped finite elements with explicitly derived coefficient matrices was introduced by Armor [37], and also by Sarkar et al [39].

The solution and calculation of the finite difference and finite element solution is limited by the discretisation and tolerances applied to the model and allows, in principal, any level of accuracy to be determined. However, the input parameters, in form of material properties, film coefficients and heat sources, generally limit the accuracy of any model, no matter how refined. A three dimensional model is generally required in order to take into account the end windings and motor end surfaces. Therefore, the increased resolution offered by 2-D finite element/finite difference methods have little value. However, the use of three dimensional finite elements which would account for the 3-dimensional effects, has been restricted due to the long computing times.

Despite its simplicity, the lumped parameter model has been used for studying

the heat flow within electric machines. Approximate equivalent networks [21,22] have been used to represent the whole machine. Others introduced very drastic assumptions to alleviate the complexity of modelling the actual bulk conduction and convection heat processes [22]. Recently more sophisticated models have been developed [17,24,26] for a wide variety of machines, configurations and operating conditions. Due to the suitability of this method for accurate prediction of thermal conditions within the machine, the relationship between machine geometry and thermal admittance will be derived and applied in the following sections.

4.2 Definition of the machine geometry

To analyse the process of heat transfer in an electrical machine, an idealised machine geometry is chosen and divided into basic elements, each of which is identified by a node in the equivalent thermal circuit, with its corresponding thermal capacitance and heat source. The choice of subdivision of the machine into elementary components results from the compromise between the simplicity of the model and the quality of information sought. Obviously, areas in which effects of subdivision are most marked must be well defined, but not overly complex. There is often a range of possible schemes, and the most appropriate division is made by judgement regarding the physical factors which are likely to contribute significantly to the temperature rises. Thus, it is necessary to rely on a good knowledge of the thermal properties and construction of the machine in order to define the principal heat flow paths of the active components. Typical heat exchange map for an induction motor is shown in Fig. 4.1.

The lumped elements are chosen to correspond approximately to the uniformity of

temperature in the machine. For example, Figs. 4.2 and 4.3 show the measured radial and circumferential steady state temperature profiles of a totally enclosed fan cooled motor operating on full load. The curve of Fig. 4.2 shows that a steep drop in temperature occurs in the air gap, and from the frame to ambient. In contrast the active parts are practically isothermal. Furthermore the circumferential temperature distribution, shown in Fig.4.3, suggest that since the temperature gradient is small in this direction, circumferential heat flow can be neglected without serious errors.

With the absence of ventilation canals, the thermal equivalent circuit of the motor can be taken as symmetrical about its radial plane through the centre of the motor. The influence of asymmetrical temperature distribution which exist as a result of the external fan being mounted at one end will be assumed to be small. Based on the above assumptions, only half of the motor needs to be modelled.

The different lumped elements are chosen on the basis of thermal and physical uniformity, viz

- Uniformity of temperatures within the element and the surfaces
- Uniformity of the heat generated for the active elements
- Uniformity of physical properties within each element
- Uniformity of exchange conditions by convection for each of the surfaces

The division of the motor into its basic thermal elements are shown in Figs. 4.4 and 4.5. In the transverse section, Fig. 4.5, the motor can be considered as a coaxial system of concentric cylinders representing the shaft, rotor iron, stator iron etc. Hence a general cylindrical component, shown in Fig. 4.6, is used as a basis for modelling the motor. Since the circumferential variation of temperature is assumed

to be negligible, heat transfer in this direction is ignored and conduction is only in the radial and axial planes.

In order to simplify the analysis two further assumptions are made,

- Heat flow in the radial and axial planes are independent of each other
- The mean temperatures in either of these directions are the same

The first assumption allows the application of the one dimensional heat flow equation to both planes whilst the second allows the network developed from one dimensional conductive heat transfer equations to be coupled together resulting in a two dimensional model. The use of these assumptions is common practice [22,23,24,33], but care should be taken over the simplification issues which depend heavily on the specific construction of the machine.

4.3 Model for heat flow in the axial direction

For an arbitrary cylinder, the steady state heat conduction in the axial direction is governed by Poisson's equation and given by,

$$\frac{d^2\theta}{dx^2} + \frac{q}{k_a} = 0 \tag{4.1}$$

where

x is the axial direction, measured from the centre,

q is the heat generated per unit volume (W/m^3),

k_a is the thermal conductivity in the axial direction $(W/m\ ^0c)$

The general solution to this equation, derived in appendix B, is given by

$$\theta(x) = \theta_4 + \frac{q}{2k_a}(h^2 - x^2) \tag{4.2}$$

where $h = \frac{H}{2}$

and the mean temperature (appendix B) is given by

$$\theta_{av} = \theta_4 + \frac{QR_0}{3} \tag{4.3}$$

where

$$R_0 = \frac{h}{\pi k_a(r_2^2 - r_1^2)}$$

$$Q = q\pi h(r_2^2 - r_1^2)$$

Comparison of Eqs. (4.2) and (4.3) shows that the location of the mean temperature is at

$$x_{av} = \frac{h}{\sqrt{3}}$$

The behaviour of the thermal circuit in the axial direction can thus be represented by the network shown in Fig. 4.7 with

$$R_1 = \frac{h}{3\pi k_a(r_2^2 - r_1^2)} = \frac{R_0}{3} \tag{4.4}$$

This network, which is symmetrical, accurately represents the axial heat flow in the cylinder for the case of only internal heat generation, and has the representation for all the temperatures of interest; θ_3 and θ_4 of the surfaces and θ_{av} the mean temperature. It can be observed that the thermal resistance from the mean temperature to the cooling medium is $\frac{R_0}{3}$, which is the thermal resistance of an equivalent cylinder of cross sectional area $\pi(r_2^2 - r_1^2)$ and effective length $\frac{h}{3}$.

4.4 Model for heat flow in the radial direction

The governing one-dimensional Poisson's equation for radial conductive heat transfer is given by,

$$\frac{d^2\theta}{dr^2} + \frac{1}{r}\frac{d\theta}{dr} + \frac{q}{k_r} = 0 \tag{4.5}$$

subject to the radial boundary conditions,

$$\left(\frac{d\theta}{dr}\right)_{r=r_1} = -\frac{Q_1}{k_r A_1} \text{ and } \theta_{r=r_2} = \theta_2$$

The general solution, described in detail in appendix B, is given by

$$\theta(r) = \theta_2 + \frac{Q}{2\pi k_r h(r_2^2 - r_1^2)}\left[\frac{r_2^2 - r^2}{2} - r_1^2 \ln\frac{r}{r_2}\right] - \frac{Q_1}{2\pi k_r h}\ln\frac{r}{r_2} \tag{4.6}$$

from which,

$$\theta_1 = \theta_2 + \frac{Q}{2\pi k_r h(r_2^2 - r_1^2)}\left[\frac{r_2^2 - r_1^2}{2} - r_1^2 \ln\frac{r_1}{r_2}\right] - \frac{Q_1}{2\pi k_r h}\ln\frac{r_1}{r_2} \tag{4.7}$$

and the mean temperature,

$$\theta_{av} = \theta_2 + \frac{Q}{4\pi k_r h(r_2^2 - r_1^2)}\left[\frac{r_2^2 - r_1^2}{2} - r_1^2(1 - 2B)\right] + \frac{Q_1}{4\pi k_r h}(1 - 2B) \tag{4.8}$$

where

$$B = \frac{r_1^2}{r_2^2 - r_1^2}\ln\frac{r_2}{r_1}$$

For the particular case when $Q = 0$, i.e. no internal heat generation, the temperature variation can be modelled by the two resistor network shown in Fig. 4.8, where

$$\begin{aligned} R_1 &= \frac{\theta_1 - \theta_{av}}{Q_1} \\ &= \frac{1}{4\pi k_r h}\left[\frac{2r_2^2}{r_2^2 - r_1^2}\ln\frac{r_2}{r_1} - 1\right] \end{aligned} \tag{4.9}$$

$$\begin{aligned} R_2 &= \frac{\theta_{av} - \theta_2}{Q_1} \\ &= \frac{1}{4\pi k_r h}\left[1 - \frac{2r_1^2}{r_2^2 - r_1^2}\ln\frac{r_2}{r_1}\right] \end{aligned} \tag{4.10}$$

For the case when $Q \neq 0$, the 'T' equivalent circuit was chosen, as shown in Fig. 4.9, where

$$\begin{aligned} R_m &= \frac{\theta_{av} - \theta_2}{Q} - R_2 \left(1 + \frac{Q_1}{Q}\right) \\ &= \frac{-1}{8\pi k_r h (r_2^2 - r_1^2)} \left[r_1^2 + r_2^2 - \frac{4 r_1^2 r_2^2}{r_2^2 - r_1^2} \ln \frac{r_2}{r_1} \right] \end{aligned} \tag{4.11}$$

and R_2 as defined previously in Eq. (4.10)

By coupling the radial and axial equivalent circuits at the position of average temperature, a complete model of a hollow cylindrical section shown in Fig. 4.10 is obtained.

For particular solution of the radial flow equation for a solid cylinder, $r_1 \rightarrow 0$, the temperature profile, Eq. (4.6) become

$$\theta(r) = \theta_2 + \frac{Q}{2\pi k_r h r_2^2} \left[\frac{r_2^2 - r^2}{2} \right] \tag{4.12}$$

and the mean temperature

$$\theta_{av} = \theta_2 + \frac{Q}{8\pi h k_r} \tag{4.13}$$

Thus the resistance to heat flow from the component mean temperature to the radial boundary is given by

$$R_r = \frac{\theta_{av} - \theta_2}{Q} = \frac{1}{8\pi h k_r} \tag{4.14}$$

and the thermal resistance in axial direction is given by setting $r_1 \rightarrow 0$

$$R_a = \frac{h}{3\pi k_a r_2^2} \tag{4.15}$$

The two previous equations can be used to model the shaft in the axial and radial directions as a cylindrical rod. The axial heat conduction of the shaft is modelled as three sections; one that lies under the rotor iron, a second that lies under the bearing, and a third that acts as a thermal link between mean temperatures of the first two. The mean temperature of the entire shaft is taken to be the temperature

at centre of the third section. A good thermal contact is assumed to exist between the shaft and the frame across the bearings, and as there is only a small contact area with the endcap air, any heat transfer between these components was neglected.

4.5 Modelling of the winding

Even though it is impractical to model individual conductors in a slot, good accuracy is still required because of the hot spots which are likely to occur in the windings. Thus a fictitious homogeneous medium with approximately the same transverse thermal conductivity as the actual conductors and insulation was developed to model the windings. The effective conductivity of the medium, however, depends on the actual arrangement of the conductors and insulation within the slots. Since the conductors in use are round with small cross section, the thermal conductivity does not differ greatly for different directions of the heat flow across the array of conductors, and it is reasonable to consider the medium as an isotropic. The following assumptions have been adopted:

- There is no significant heat flow through slot opening.
- All the wires have the same insulation.
- The thickness of the slot liner is uniform.
- No voids are present in the slot.
- The thermal conductivity of the copper is considered to be infinite compared to those of the insulating materials.

To model the windings, the round wires are replaced by conductors of a square cross section with a width, W, which has the conductor area as the round wire, and an insulation of uniform thickness, δ, which has the same cross sectional area as the actual insulation, including the space between the insulated wires. The equivalent conductors are shown in Figs. 4.11a and b.

Hence the copper cross sectional area is given by

$$A = \frac{\pi}{4}(d - 2t)^2 = W^2 \tag{4.16}$$

whilst the insulation area is given by

$$d^2 - A = (W + 2\delta)^2 - W^2 \tag{4.17}$$

Thus

$$d = W + 2\delta \tag{4.18}$$

The equivalent cross section of the new arrangement conductors is shown in Fig.4.11b. Assuming that the planes xz and yz are isothermal, the per unit length thermal resistances for an equivalent conductor in these two directions, with reference to the equivalent circuit shown in Fig. 4.11c, are

$$R_x = R_y = \frac{2\delta}{k_i(W + 2\delta)} + \frac{W}{2k_i\delta + k_cW} \tag{4.19}$$

where

k_i is the thermal conductivity of insulation,

k_c is the thermal conductivity of copper.

The corresponding resistances of an equivalent fictitious element of the same geometrical dimensions as the composite material are,

$$R_x = R_y = \frac{W + 2\delta}{k_e(W + 2\delta)} = \frac{1}{k_e} \tag{4.20}$$

where k_e is the equivalent thermal conductivity of the fictitious element.

Comparing Eqs. (4.19) and (4.20) respectively yields the equivalent thermal conductivity for the coppper/insulation combination which is given by

$$\frac{1}{k_e} = \frac{2\delta}{k_i(W+2\delta)} + \frac{W}{2k_i\delta + k_cW} \tag{4.21}$$

For $k_c \to \infty$ yields

$$k_e = k_i\left(1 + \frac{W}{2\delta}\right) \tag{4.22}$$

The effective thermal conductivity for heat flow across an array of conductors embedded in insulating material can be also determined by treating the combination as homogeneous but with an effective thermal conductivity k_e which is given by

$$k_e = Fk_i$$

where $F > 1.0$, and assuming that the region is completely filled with a homogeneous insulation material. F can be determined from experimental curves [70], by estimating the percentage of copper by volume in the slot.

4.5.1 Transverse heat conduction model for the embedded windings

Fig. 4.12 shows a simplified section for a quarter of a turn of the winding. There are n identical sections where n denotes the number of slots. Fig.4.13 shows the cross section to be modelled. This configuration can be analysed on the basis of a two dimensional conduction model with uniformly distributed internal heat generation and no external heat input. The circuit of Fig.4.14,a comes directly from the general case of Fig.B.2 in appenidx B. The equivalent thermal circuit can be further simplified by setting $\theta_1 = \theta_2$ and has been presented in Fig.4.14,b. giving the values of

R_{xc} and R_{yc}. The resistance of R_{xi} and R_{yi} are just the thermal resistances offered by the slot liner insulation in the transverse and radial directions respectively.
The thermal resistance of copper resistance in the transverse direction is,

$$R_{xc} = \frac{W_{av}}{12k_eC_hh} \tag{4.23}$$

whereas in the radial direction it is,

$$R_{yc} = \frac{C_h}{3k_eW_{av}h} \tag{4.24}$$

The resistances R_{xi} and R_{yi} are the thermal resistances offered by the external layer of insulation in the directions x and y respectively.

$$R_{xi} = \frac{\delta}{k_{sl}C_hh} // \frac{\delta}{k_{sl}C_hh} \tag{4.25}$$

$$R_{yi} = \frac{\delta}{k_{sl}W_{iav}h} \tag{4.26}$$

where k_{sl} is the thermal conductivity of the slot liner

The equivalent thermal resistances for the n slots and their slot liner insulation in the transverse and radial directions are

$$R_x = R_{xc} + R_{xi} = \frac{W_{av}}{12nk_eC_hh} + \frac{\delta}{2nk_{sl}C_hh} \tag{4.27}$$

$$R_y = R_{yc} + R_{yi} = \frac{C_h}{3nk_eW_{av}h} + \frac{\delta}{nk_{sl}W_{iav}h} \tag{4.28}$$

4.5.2 Transverse heat conduction model for the end windings

The end winding is modelled as a homogeneous toroid structure, as shown in Fig. 4.12. The difference between the embedded windings and the end windings is that, here, the heat flows out radially throughout the length of the end winding in

the absence of the slot liner insulation. It is assumed that the surface temperature of the end winding is uniform around its periphery. The circuit of Fig. 4.14c comes directly from the general case of Fig.B.2. The value of the thermal resistances in the approximate equivalent network of Fig.4.14d are

$$R_{exc} = \frac{W_{av}}{12k_e C_h h_{av}} \tag{4.29}$$

$$R_{eyc} = \frac{C_h}{12k_e W_{av} h_{av}} \tag{4.30}$$

and thus the resultant thermal resistances for the n slots in the transverse and radial directions become

$$R_{ex} = \frac{W_{av}}{12nk_e C_h h_{av}} \tag{4.31}$$

$$R_{ey} = \frac{C_h}{12nk_e W_{av} h_{av}} \tag{4.32}$$

4.5.3 Model for axial heat flow in copper

It is assumed that only the copper conductors transfer heat axially along the slot. The thermal resistance in the axial direction is modelled in the same manner as a cylinder and is given in Eq. (4.15).

$$R_{ac} = \frac{h}{3k_c W_{av} C_h} \tag{4.33}$$

4.5.4 Rotor winding model

The rotor was modelled as a continuous aluminium cylinder with a volume equal to the total volume of the bar. The end ring was modelled as a disc joined to the main cylindrical structure.

4.6 Modelling of heat convection related elements

The convection heat transfer between the exposed surfaces of the solid components of the motor, and the external or internal air in the enclosed motor, is modelled by a single thermal resistance R_{cv} using Newton's law of cooling and can be expressed as

$$R_{cv} = \frac{1}{hA} \tag{4.34}$$

where

A:is the surface area in contact with the cooling air (m^2)

h:is the film coefficient $(W/m^2\ ^oC)$.

Heat convection is a very complex process and the simplicity of Eq. (4.34) is misleading because the film coefficient is a function of geometry, dimensions of the surface, material type, direction and velocity of flow; temperature, density, viscosity, specific heat and thermal conductivity of the fluid.

However, because of the difficulty in determining the coefficient of heat transfer, experimental and analytical results obtained by other authors [24,26,76,70] relating to air flow around similar geometries were used.

4.6.1 Convective heat transfer model between frame and ambient

The heat transfer from motor frame to ambient is a function of the total surface area, the efficiency of the cooling fins and the convective film coefficient of the forced cooling air. The heat transfer coefficient from a ribbed surface depends on the air

flow velocity, the relative dimensions the rib, etc. The air flow between the ribs can be regarded as analogous to the flow of air in channel. According to Heiles [71] the heat transfer coefficient is given by,

$$h_{Fin} = \left(\frac{\rho c_p V D}{4H} 10^4\right)(1 - \exp(-E)) \tag{4.35}$$

where

$$E = 0.1448(H_{Fin}^{0.946}/D^{1.16})(k/\rho c_p V)^{0.214}$$

where

V:flow velocity of the cooling air (cm/s)

k:thermal conductivity of the cooling air $(W/cm°C)$

ρ :density of the cooling air (g/cm^3)

c_p:specific heat of cooling air $(W\ s/g\ °C)$

H_{Fin}:axial length of cooling fins (cm)

D:flow diameter, equals to diameter for channels of circular cross-section, (cm)

h_{Fin}:heat transfer coefficient $(W/m^2\ °C)$

The value obtained from Eq. (4.35) is for smooth surfaces and nonturbulent flows. However, turbulences in the air flow raises the value of heat transfer coefficient considerably. According to Heiles [71] the increase in heat transfer coefficient is independent of the flow velocity, i.e. fan speed, and can be accounted by multiplying the result obtained in Eq. (4.35) by a turbulent factor ξ, which is typically in the range $1.7 - 1.9$.

The value of fin efficiency (η) multiplied by the fin surface area gives a reduced area which can be regarded as being equivalent to an equal additional area on the casing as regards heat dissipation. The resultant increased area of the casing can then be

related to the value of the heat transfer coefficient h_f. The fin efficiency can be found by [72]

$$\eta = \frac{\tanh[(h_{Fin}p/k_{Fin}A)^{0.5}H_{Fin}]}{(h_{Fin}p/k_{Fin}A)^{0.5}H_{Fin}} \tag{4.36}$$

where

A and p are the cross sectional area and the perimeter of the fin respectively

h_{Fin}: film coefficient of the fin

k_{Fin}: thermal conductivity of the fin material

H_{Fin}: axial length of the fin

With the assumption that no heat flows from the tip of the fins, the total heat dissipation from the frame/fins combination is then obtained as,

$$Q = [(A_1 + \eta A_{Fin})\xi h_f](\theta_f - \theta_a) \tag{4.37}$$

where A_1 and A_{Fin} are the surface of frame casing which is directly in contact with the cooling air and surface of the fins respectively.

$A_f = (A_1 + \eta A_{Fin})$ frame effective area.

4.6.2 Convective heat transfer model for the air gap

The heat transfer characteristics in the air gap are the least well defined in an electric machine. Although experimental data for heat transfer across a gap between the concentric cylinders exists, the results are not consistent and have not been rationalised so that they can be extended to other situations [73]. In a totally enclosed fan cooled motor, there is little or no axial heat flow from the air gap into the surrounding end cap air, and all the heat emitted from the rotor surface is assumed to be transferred directly across the air gap to the stator.

The types of hydrodynamic flow of the cooling medium depend on the rotor running speed, the airgap length, the finish surfaces forming the airgap of non salient pole machines, etc. The effect of rotation is described by Taylor's [74] work on heat transfer between smooth rotating cylinders, where the roughness effect is accounted for by increasing coefficients of Taylor by approximately 10% as suggested by Gazley [73].

The airgap of the machine is modelled by a smooth inner rotating cylinder and a grooved stationary surface.

The convective heat transfer coefficient is expressed by Taylor as

$$h = \frac{Nu\ k_{air}}{lg} \tag{4.38}$$

where N_u, is the Nusselt number can be evaluated from whichever of the following alternative formulae according to the range of calculated Taylor values, and summarised in reference [70] as shown in Table 4.1.

Nusselt Number N_u	Taylor Number T_a
$N_u = 1$	$T_a < 41$
$N_u = 0.106 T_a^{0.63} P_r^{0.27}$	$41 < T_a < 100$
$N_u = 0.193 T_a^{0.5} P_r^{0.27}$	$100 < T_a < (T_a)_{v.t}$

Table 4.1: Evaluation of N_u pertinent to the range of T_a

Ta, and Pr, are Taylor's and Prandlt's numbers respectively, and can be found from the following expressions,

$$T_a = \frac{\rho \omega r l_g}{\mu} \sqrt{\frac{l_g}{r}} \tag{4.39}$$

$$P_r = \frac{c_p \mu}{k_{air}} \tag{4.40}$$

With Gazley's [73] recommendations the nusselt's numbers are modified and are shown in Table 4.2

Nusselt Number N_u	Taylor Number T_a
$N_u = 1.1$	$T_a < 41$
$N_u = 0.117 T_a^{0.63} P_r^{0.27}$	$41 < T_a < 100$
$N_u = 0.212 T_a^{0.5} P_r^{0.27}$	$100 < T_a < (T_a)_{v.t}$

Table 4.2: Evaluation of N_u pertinent to the range of $T_a$with 10% increase

where $(T_a)_{v.t}$ is the value of T_a above which turbulent flow is dominant instead of vortex flow.

4.6.3 Heat transfer model between end windings and end-cap air

In the endcap region, the end winding space presents a particular problem because the flow conditions are not clearly defined since the air is turbulent in the enclosed space and there are no smooth or flat surfaces. Furthermore, the end windings themselves are generally irregular since they are made of wires.

Experimental work of Luke [75] on the dissipation of heat flow from the end windings is used to determine the value of the film coefficient associated with the endcap air. For small cooling air velocities, less than $7m/s$, Mellor [26] approximated the results

of Luke by

$$h = 15.5(0.39V + 1) \tag{4.41}$$

where

V is the cooling air velocity (m/s)

A rough and simple estimation for the velocity of air is the average of the velocity of the air at the shaft, and at the end shield which is considered to be zero.

$$V = \frac{\omega r_{sh}}{2}$$

where r_{sh} is the shaft radius.

For cooling velocities higher than that mentioned above, h may be found directly from Luke results [75].

4.6.4 Heat transfer model for the end shield

Due to motion of the rotating parts of the motor (rotor), air flows tangentially to the end shield, and this process of forced convection can be modelled as flow past a flat plate. The analytical expressions developed by Chapman [76] are used, i.e.

$$N_u = 0.664 R_e^{\frac{1}{2}} P_r^{\frac{1}{3}} \quad R_e < 4.10^5 \text{ for laminar flow.}$$

$$N_u = 0.036 R_e^{0.8} P_r^{\frac{1}{3}} \quad R_e > 4.10^5 \text{ for turbulent flow.}$$

where

$Re = \frac{\rho V H_{sh}}{\mu}$ is the Reynolds number

Heat transfer and fluid data book [70] gives film coefficients for the a flat plate, which is shown to be valid for the vertical end plates of the end shield. Hence a set of averaged coefficients were used.

4.7 Thermal contact resistances

When materials are placed together, an interface is formed, e.g. between the copper and insulation, and these represent thermal resistances to heat flow between the materials. Experimental work has been carried out to determine the contact resistances between metals but even so the understanding of contact heat transfer, particularly in electrical machines, is limited because of considerable difficulties in characterising a contact surface precisely. Of particular importance in a machine is the stator back iron/frame interface since this represent a thermal resistance in the main flow path from the internal sources to the ambient. In general this thermal resistance is a function of the physical properties of the contact material, the surface conditions and finish, roughness of the material, and the contact pressure. Mellor et al [26] observed that a substantial difference exists between the contact coefficients found experimentally and those obtained from extrapolated curve of Brunot and Backland [77], and cast doubt upon the validity of the extrapolated curve. Moreover, even for large variation in the value of thermal contact resistance, it was found [26] that the effect on the estimation of the winding temperatures from the model used had little effect.

The heat flow across the interface can be modelled by a simple resistance, R_{ct} defined

as,

$$R_{ct} = \frac{1}{h_{ct}A} \tag{4.42}$$

The thermal coefficient, h_{ct} is a function of the pressure which is created when the frame is shrunk onto the core during manufacture, and the roughness of the surface in contact. The pressure is estimated using Eq. (4.43) [78] using manufacturer's design drawings data, and the physical properties of the core and frame materials.

$$P_c = \frac{\delta_c}{\frac{b}{E_f}\left(\frac{b^2+c^2}{c^2-b^2} + \mu_f\right) + \frac{b}{E_s}\left(\frac{a^2+b^2}{b^2-a^2} - \mu_s\right)} \tag{4.43}$$

where

P_c:the contact pressure

a:half the stator bore

b:the radius of the core frame interface

c:the frame barrel diameter

μ_f:Poisson ratio for the frame material

μ_s:Poisson ratio for the core material

E_f:the elastic modulus of the frame

E_s:the elastic modulus of the core

δ:the outer core radius - inner frame radius

For low contact pressures, the heat transfer coefficient for the contact resistance can be found directly from the experimental curves of Brunot and Buckland [77], but for higher values Roberts [78] extrapolated the experimental results of Brunot and Buckland [77] using the semi-emperical equation developed by Shlykov and Ganin [79].

4.8 Radiation mode of heat transfer

Radiation does not form an important mode of heat transfer because the temperatures that are involved do not vary considerably. It is permissible to include radiation in a coefficient of dissipation or equivalent conductance which can be regarded as constant. However, there is no difficulty in finding an analytical expression for this mode of heat transfer.

The transfer of heat by radiation depends upon the difference between the fourth powers of the absolute temperatures of the parts concerned, and linearity must not be assumed where radiation plays a significant part. It is found that nonlinearity associated with radiation is rarely of importance in machines [83]. The contribution of radiation to the total cooling of a conventionally ventilated machine is expected to be small [24]. In some cases it is expedient to define a radiation coefficient, h_r on the basis of a linear temperature difference as with the film coefficient in heat convection. Thus the expression for calculating the net heat transfer rate can be written as,

$$Q = h_r A_f(\theta_f - \theta_a) \tag{4.44}$$

where

$$h_r = \sigma F_{fa}(\theta_f^2 + \theta_a^2)(\theta_f + \theta_a)$$

where

h_r:the radiant heat transfer coefficient

σ:the Boltzman constant

F_{fa}:the shape factor

θ_f:the absolute temperature of the frame

θ_a:the absolute temperatures of the ambient

A_f:the effective area of the frame.

When both the convective and radiant heat losses occur simultaneously, a simple equation may be used to represent the two processes of heat transfer, i.e.,

$$Q_r = A_f(h_c + h_r)(\theta_f - \theta_a) \tag{4.45}$$

Because the motor dimensions are small compared to the cavity, laboratory, the shape factor based upon the surface of the motor body is equal to unity, and the emissivity factor is the emissivity of the surface of the motor. The test motor gives a value of 24.5 W when the emissivity of an ordinary painted machine is taken to be 0.9. This represent approximately 3% of the total losses of the motor in use.

4.9 Conclusion

A lumped thermal model for a totally enclosed fan cooled induction motor has been developed and discussed. The model is based on dimensional data, physical and thermal constants, and published and/or experimental heat transfer characteristics. The performance of the lumped thermal circuit not only depends on the formulation of a correct network but also on the allocation of losses to the nodes and on the correct evaluation of thermal coefficients. The correct allocation of losses and specification of the thermal coefficients will be dealt with in the next chapter together with the performance of the model.

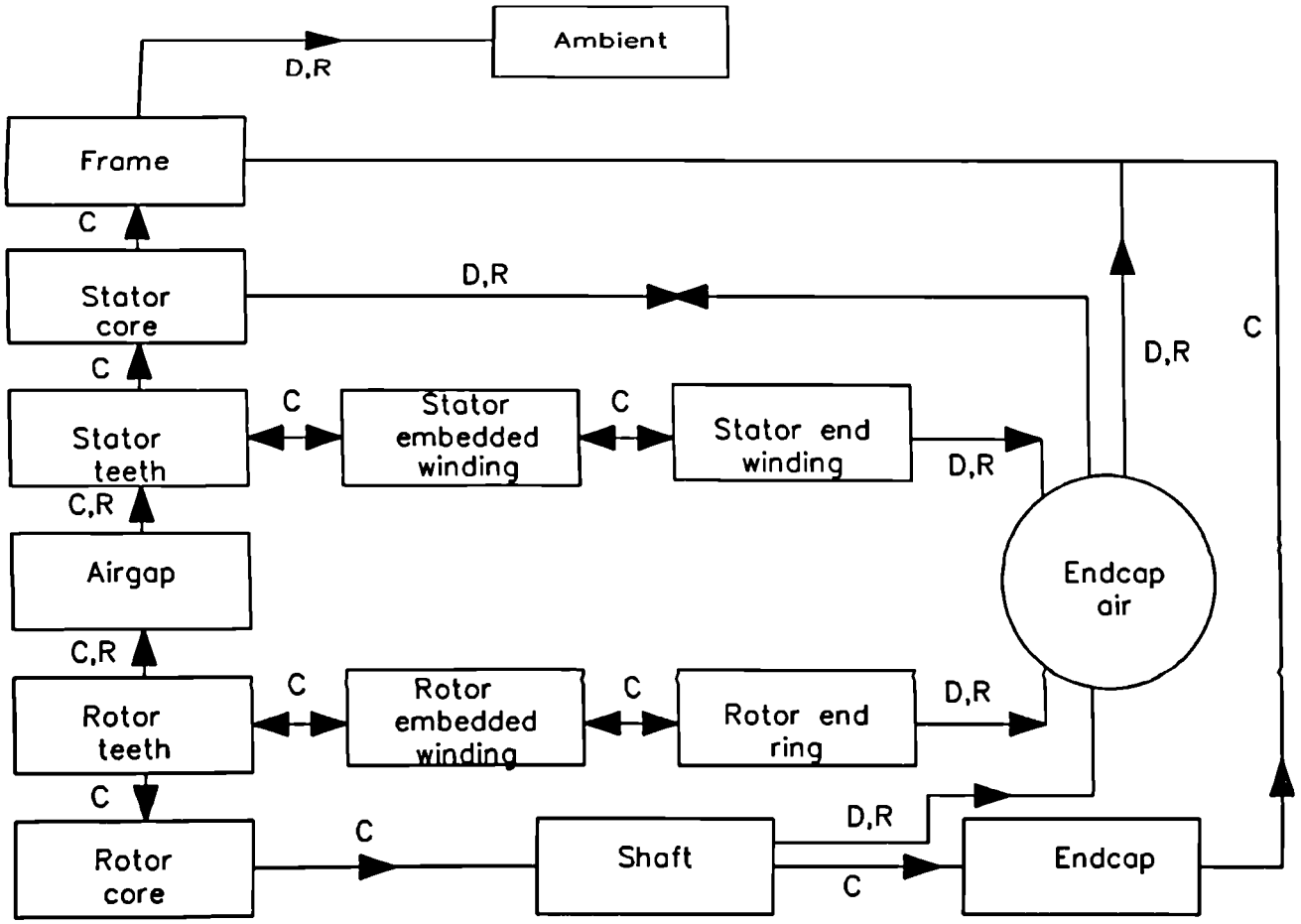

C: Conduction, D: Convection, R: Radiation.

Fig. 4.1 Heat exchange map

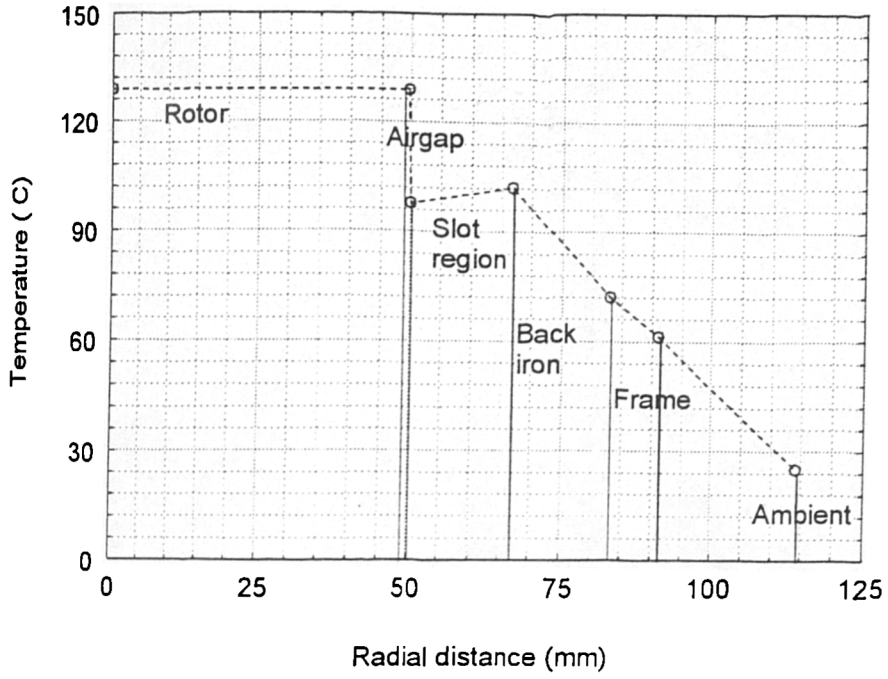

Fig. 4.2 Radial temperature distribution at full load.

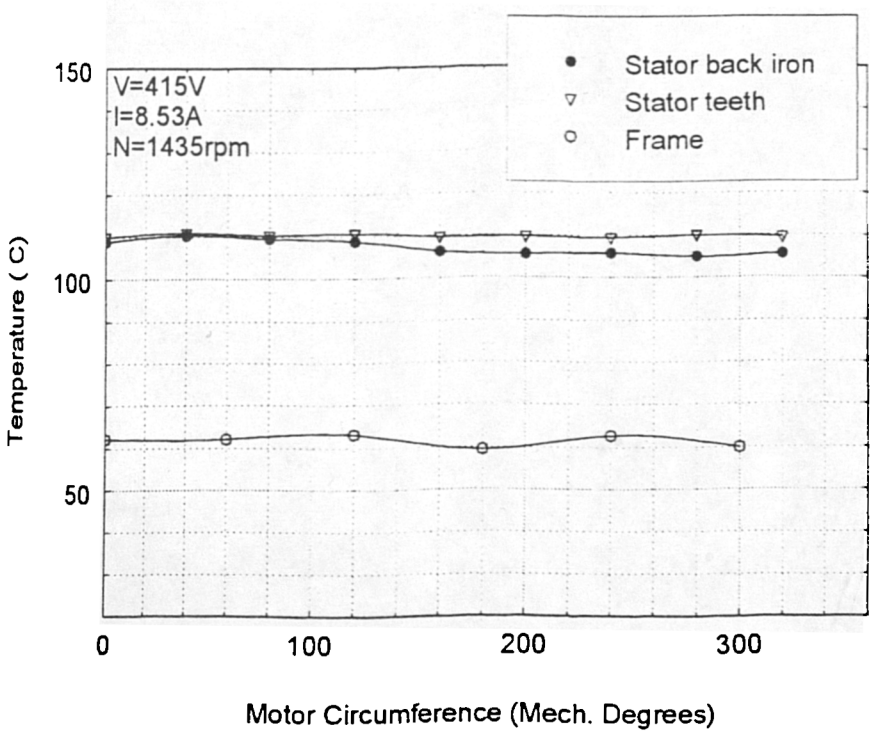

Fig. 4.3 Circumferential temperature distribution at full load.

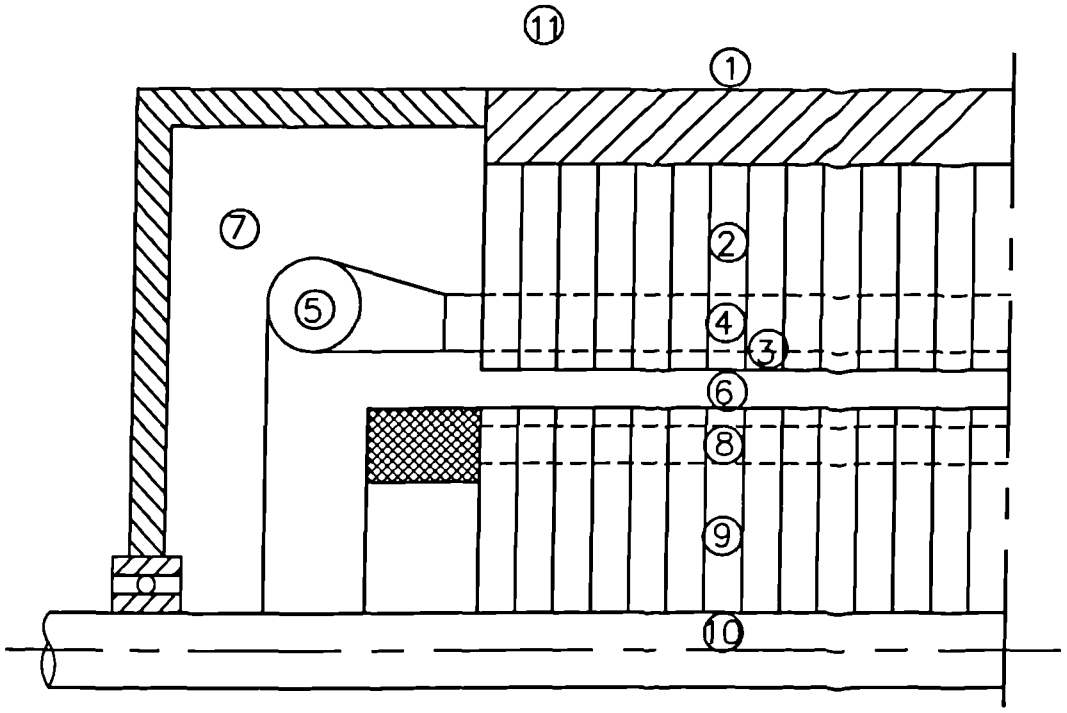

1) Frame
2) Back iron
3) Teeth
4) Embedded winding
5) End winding
6) Airgap
7) Endcap air
8) Rotor winding
9) Rotor iron
10) Shaft
11) Ambient

Fig. 4.4 Subdivision of the machine into lumped elements.

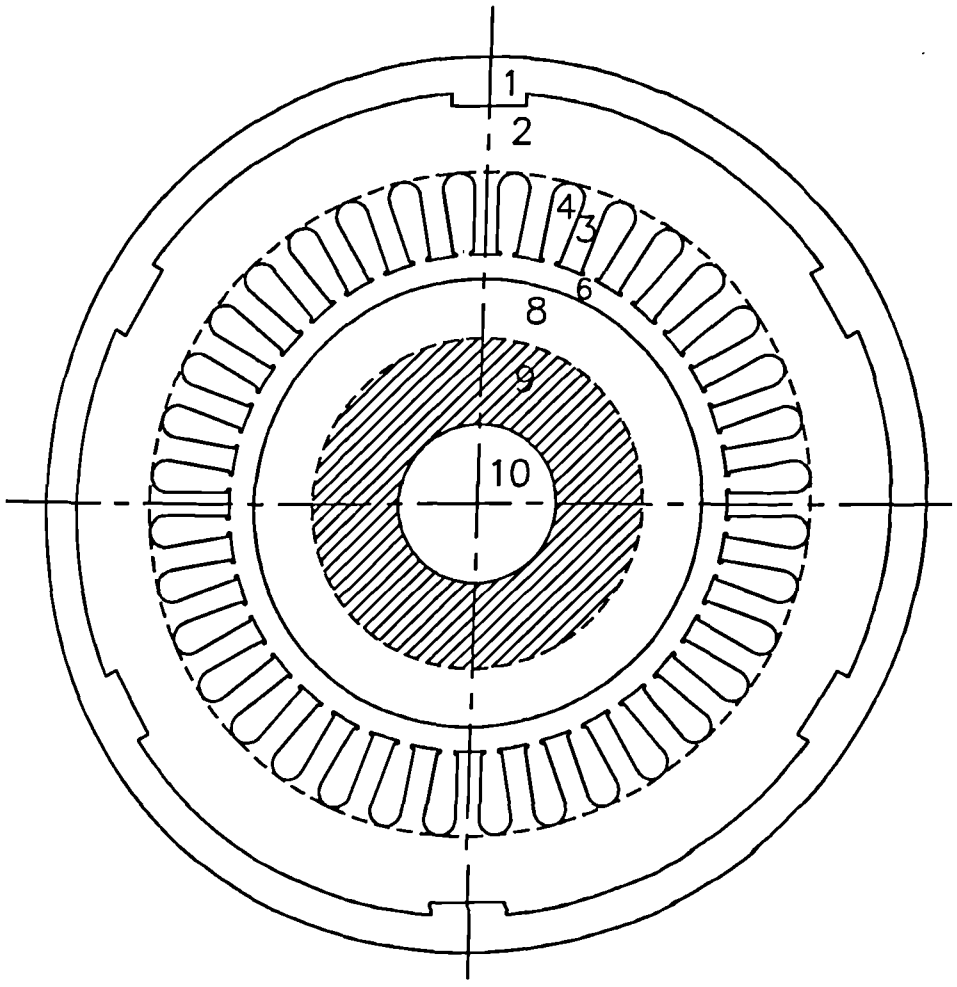

Fig. 4.5 Transverse section of an induction motor showing the lumped elements.

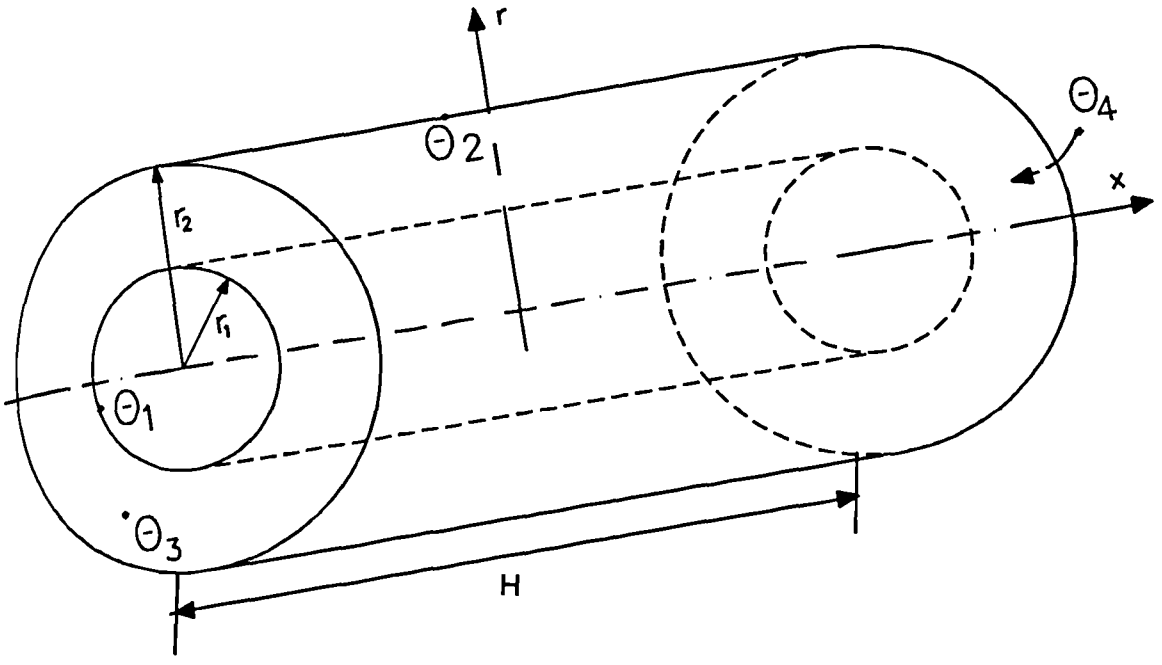

Fig. 4.6 Two dimensional cylindrical element

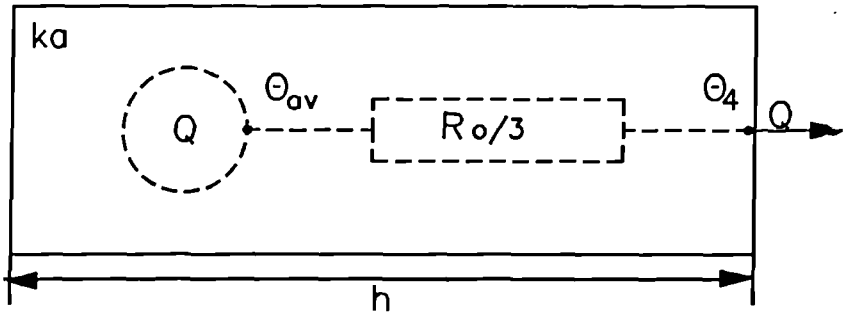

Fig. 4.7 Equivalent circuit for a cylindrical element in axial direction (internal heat generation only)

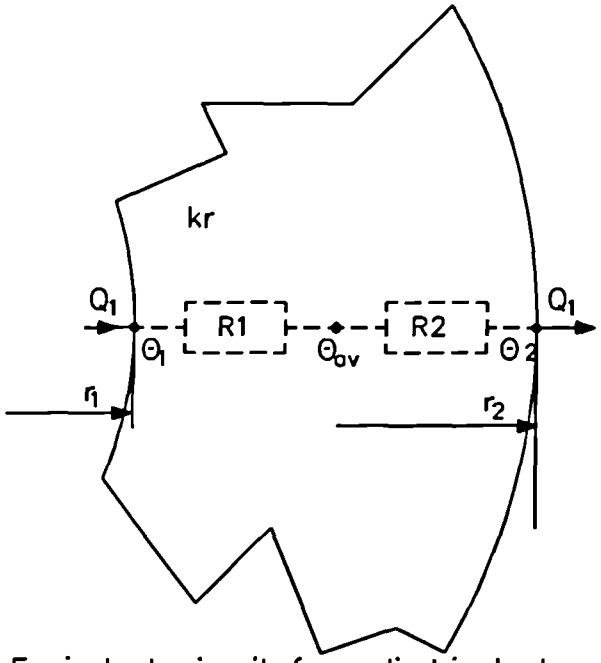

Fig. 4.8 Equivalent circuit for cylindrical element in the radial direction (no internal heat generation)

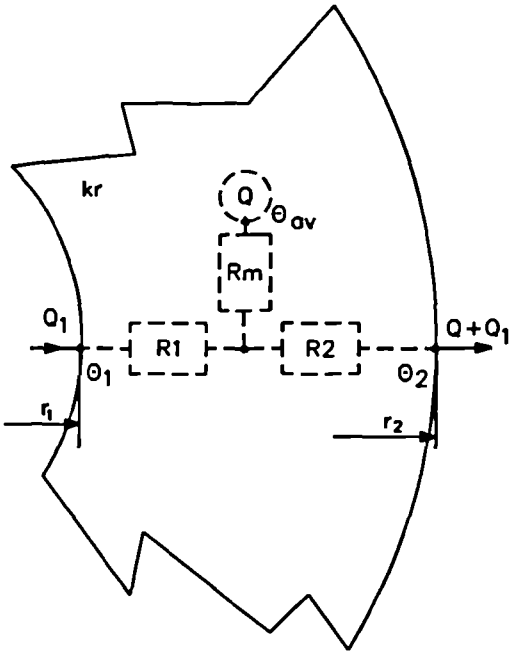

Fig. 4.9 Equivalent circuit for cylindrical element in the radial direction (with internal heat generation)

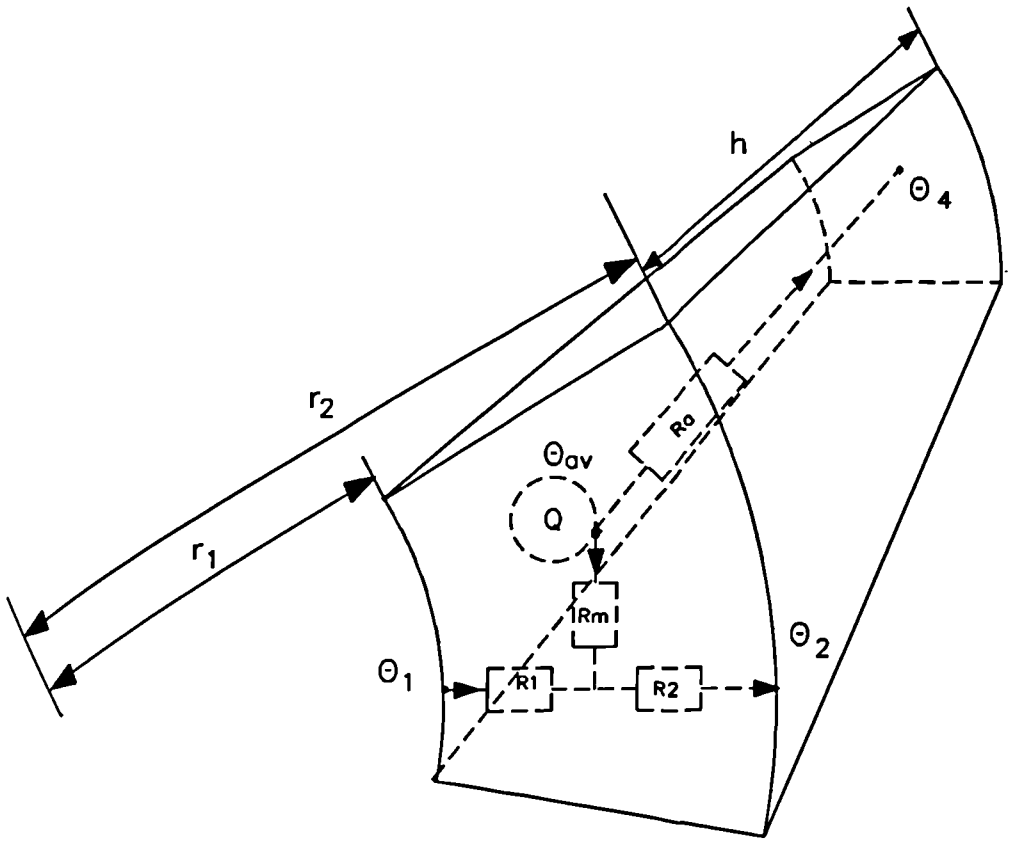

Fig. 4.10 Section of a cylinder showing the two dimensional thermal equivalent circuit.

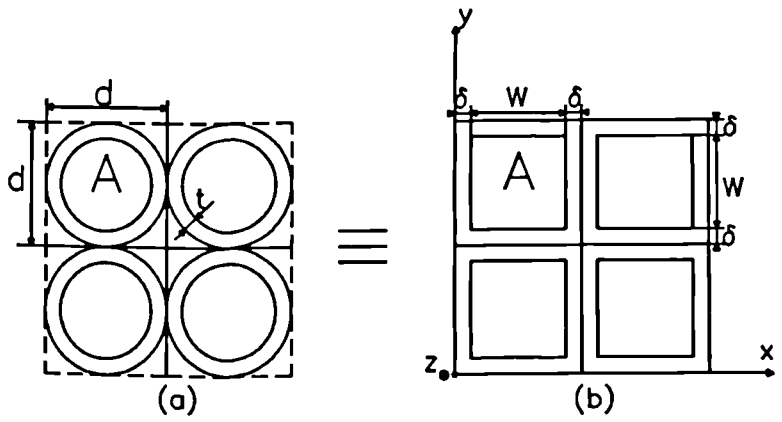

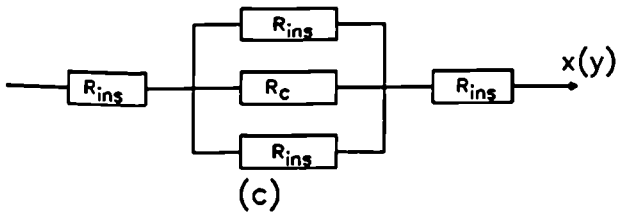

Fig. 4.11 Equivalent thermal resistance for winding.

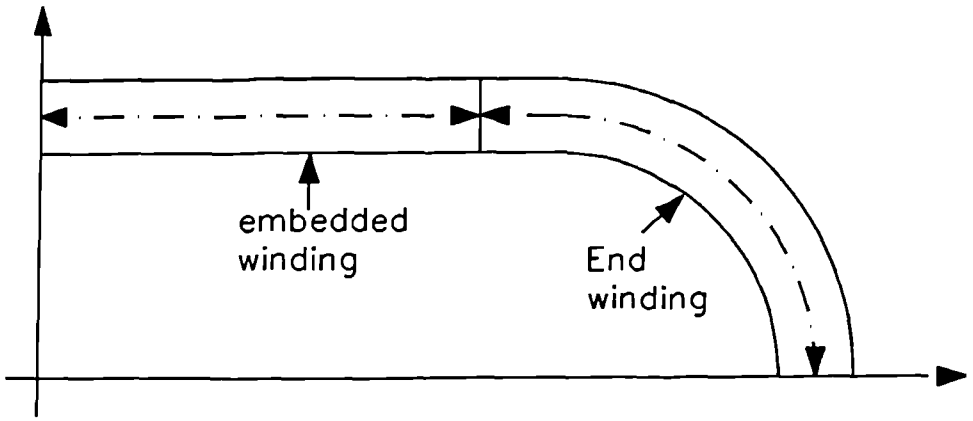

Fig. 4.12 Simplified model for a quarter of a winding

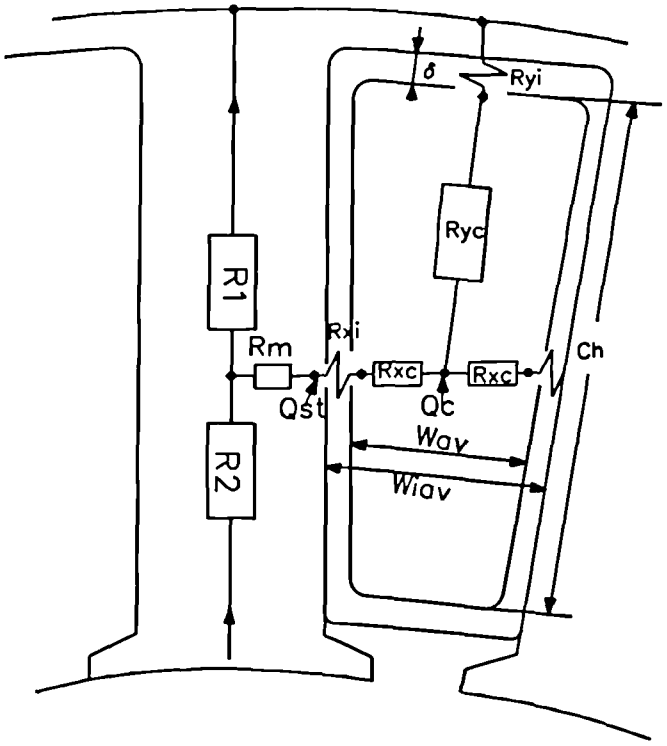

Fig. 4.13 Cross section showing slot winding.

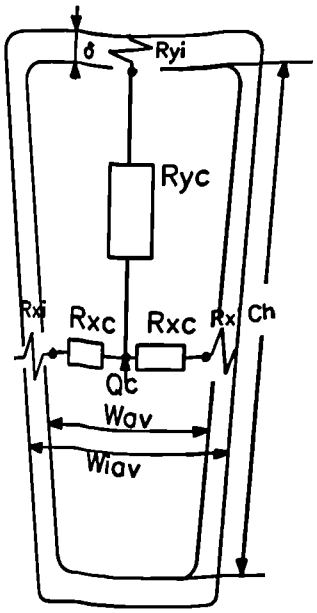

(a)

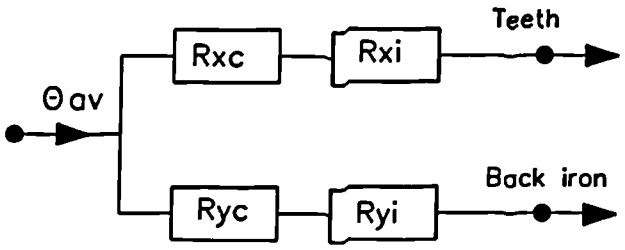

$Rxc = Rxo/6$

$Rxo = Wav/(k_e C_h h)$

$Ryc = Ryo/3$

$Ryo = C_h/(k_e Wav\ h)$

(b)

Fig. 4.14 Equivalent thermal circuit for the embedded winding.

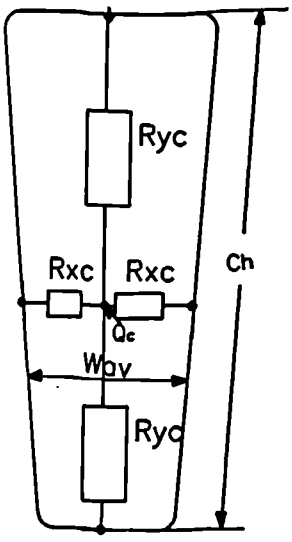

(c)

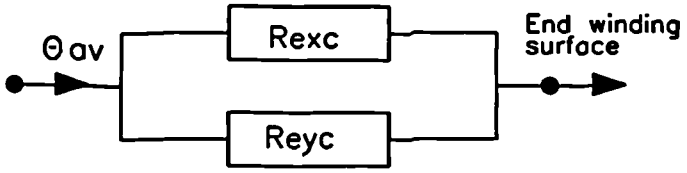

$Rexc = Rxeo/6$

$Rxeo = Wav/(k_e C_h hav)$

$Reyc = Ryeo/6$

$Ryeo = C_h/(k_e Wav\ hav)$

(d)

Fig. 4.14 Equivalent thermal circuit for the end winding.

Chapter 5

Development and evaluation of thermal model theoretical and experimental results

5.1 Introduction

To assess the accuracy of the lumped thermal model a representation of the 4-pole, 4kW induction motor, fully described in appendix A, was developed using the analysis in the preceding chapter. The induction motor was divided into ten components as shown in Fig. 4.4. Fig. 5.1 shows the equivalent thermal circuit which results as a consequence of the discretisation of the machine and the interconnection of the components. Thermal resistances are simply a function of the dimensions, and thermal and physical properties.

An accurate prediction of temperature rise in the equivalent circuit not only hinges

on the correct network but also on the correct allocation of losses to the nodes in the network. Whilst the calculation of some of the injected losses are relatively straightforward, example copper losses and rotor copper losses, other, in particular the iron loss distribution is not so clearly defined. In the sections that follow the correct allocation of the losses to each part of the network will be discussed and justified. Finally measurements made on a heavily instrumented test motor will be given to substantiate the results obtained from the equivalent thermal network.

5.2 Allocation of motor losses in the thermal model

The convenient and practical way to represent the motor losses, in terms of input current and voltage, is to use an electrical equivalent circuit used by Say [80] which was found to be reasonably accurate [26,78]. The components of the equivalent circuit can be easily be determined from the conventional no load and locked rotor tests as reported in Appendix A using IEEE standard [42]. The parameters thus calculated, (appendix C), allows the copper and iron losses to be estimated, viz

Stator copper loss is given by,

$$Q_{sc} = I_1^2 R_1 \tag{5.1}$$

Rotor copper loss is given by

$$Q_{rc} = -\frac{R_2}{cX_m(X_m + 2X_{s/c})}V_1^2 + \frac{cR_2X_m}{Xm + 2X_{s/c}}I_1^2 \tag{5.2}$$

Iron loss is given by,

$$Q_I = \frac{V_1^2}{cR_m} - \frac{R_1}{cX_m(X_m + 2X_{s/c})}V_1^2 + \left(\frac{cX_m}{Xm + 2X_{s/c}} - 1\right)R_1 I_1^2 \tag{5.3}$$

The copper loss are well defined, and can be imposed at nodes 4 and 5 in fig. 5.1. No reliable information, however, is available to indicate precisely how the iron losses, defined by Eq. (5.3), should be allocated within the motor. Mellor et al [26] employed ad-hoc method by splitting these losses into fixed proportions, 50% to the stator teeth and 50% to the rotor teeth. This is however unreliable and depends on the experience of the designer.

Tests performed on the motor using temperature time technique enables the stator losses to be split up exactly between the back iron and the teeth, the only short fall being that with the existing implementation rotor iron loss is assumed to be negligible.

5.2.1 Distribution of the motor losses

The iron loss forms a large component of the motor losses, but no reliable information exists to indicate precisely what the percentage split might be. Tests performed on similar motor using the temperature time technique described in chapter 3 was taken as the base for splitting up iron losses. However, this method falls short as it does not include the iron loss in the rotor which is considered to be small at normal running conditions. Since Eq. (5.3) agrees well with the calculated iron loss (Table 3.3) it is used as the basis for calculating the total iron loss for the new motor. Thus, according to Table 3.2 70% of total iron loss is attributed to the stator back iron whilst the remaining 30% is attributed to the teeth, i.e.

$$Q_{bI} = 0.7Q_I \tag{5.4}$$

$$Q_{tI} = 0.3Q_I \tag{5.5}$$

If the iron loss is not split up properly between the teeth and back iron, the model

will give erroneous winding temperatures. This can be observed by comparing the two circuits shown in Fig. 5.2a and b. In Fig. 5.2a where all the losses are injected to teeth, only two sources exist, i.e. $Q = (Q_1 + Q_2)$ which is the iron loss injected to the teeth, and Q_3 is the copper loss in the slots which are connected by resistances R_{12}, R_{13} and R_{23} as shown in Fig. 5.2a. This application yields a back iron temperature given by

$$\theta_{bi} = \theta_f + R_f(Q + Q_3) \tag{5.6}$$

On the other hand, splitting up the iron loss into Q_1 and Q_2 yields the arrangement shown in Fig. 5.2b and the back iron temperature is given by

$$\theta_{bi} = \theta_f + R_f(Q_1 + Q_2 + Q_3) \tag{5.7}$$

where

Q_1:iron loss in the teeth

Q_2:iron loss in the back iron

$Q = Q_1 + Q_2$

Hence, splitting of the iron losses has no influence on the back iron temperature.

The winding temperature for the two configurations can be found by simplifying the circuits to those shown in Figs. 5.2c and d so that the winding temperature (without splitting) is

$$\theta_w = \theta_{bi} + \left[Q_3 + Q\frac{R_{12}}{R_{12} + R_{13}}\right]\left[\frac{R_{23}(R_{12} + R_{13})}{R_{12} + R_{13} + R_{23}}\right] \tag{5.8}$$

Substituting for $Q = Q_1 + Q_2$ the above equation become

$$\theta_w = \theta_{bi} + \left[Q_3 + (Q_1 + Q_2)\frac{R_{12}}{R_{12} + R_{13}}\right]\left[\frac{R_{23}(R_{12} + R_{13})}{R_{12} + R_{13} + R_{23}}\right] \tag{5.9}$$

and winding temperature (with splitting) is given by

$$\theta_{ws} = \theta_{bi} + \left[Q_3 + Q_1\frac{R_{12}}{R_{12} + R_{13}}\right]\left[\frac{R_{23}(R_{12} + R_{13})}{R_{12} + R_{13} + R_{23}}\right] \tag{5.10}$$

The change in winding temperature as a result of proportioning iron loss is

$$\theta_w - \theta_{ws} = Q_2 \frac{R_{12}R_{23}}{R_{12} + R_{13} + R_{23}} \tag{5.11}$$

which indicates the importance of correctly specifying the loss distribution. In practice, over the range of loss densities investigated, the predicted difference in temperature was found to be slight, typically 0.5 ^oC. This is probably caused by cancellation effects due to the interaction of the other coupled network branches.

The losses in the winding are distributed between the slotted and end winding regions on the basis of a factor, β, which is derived from the manufacturer's design data based on the copper wire length in the embedded and end winding regions. The embedded copper loss is given by,

$$Q_{scw} = \beta Q_{sc} \tag{5.12}$$

The end winding copper loss is given by,

$$Q_{scew} = (1 - \beta) Q_{sc} \tag{5.13}$$

The losses in a squirrel cage are distributed proportionately between the bars and end rings in the ratio of their I^2R losses.

5.3 Evaluation of the thermal model parameters

5.3.1 Evaluation of materials thermal conductivity

The motor is made up of a number of materials with widely varying thermal properties. While it is easy to obtain the numerical values of thermal properties for the individual components, it is difficult to obtain the exact equivalent values when

they are in composite form, for example in the windings. The thermal conductivities which are used for individual materials are taken from published literature [70,72] are summarised in appendix D, together with the relevant dimensions of the motor. It is shown that the thermal conductivity of the conductor bunch and slot liner insulation cannot be determined from specific thermal conductivity of materials taken from table due to the type of impregnation, the tightness of fit in the slot, and voids that may be present, etc. Consequently, the effective thermal conductivity for the conductor bunch, including the slot liner insulation, was found experimentally. A d.c. current test was conducted by passing a direct current through the stator windings until steady state temperature was reached. The relevant data was collected, namely temperatures and losses, from which the effective thermal conductivity is determined using Eq. (5.14), derived in chapter 4.

$$k_e = \frac{1}{8\pi h}\frac{Q}{\Delta\theta} \tag{5.14}$$

The slot liner insulation is a composite of two layers, 0.0762 mm Nomex plus 0.1778 mm polyester. The equivalent thermal conductivity of the two layers can be found using Eq. (5.15) [81]

$$k_{sl} = \frac{k_n k_p l_e}{k_n l_p + k_p l_n} \tag{5.15}$$

where

k_n and k_p are thermal conductivity of Nomex and polyester respectively

l_n and l_p their thickness

$l_e = l_n + l_p$

Table 5.1 summarises the values found.

Method	k_e $(W/m\ ^0C)$	k_{slot} $(W/m\ ^oC)$
Analytical (Eq. 4.22)	0.477	-
From curves [70]	0.468	-
Analytical (Eq. 5.15)	-	0.244
Experimental	-	0.125

Table 5.1: The effective thermal conductivity for winding

5.3.2 Evaluation of film coefficients

The final stage of heat removal is convection from the outer surfaces of the machine. Accurate calculation of the film coefficient from frame surface is essential to allow realistic determination of temperature distribution. The heat transfer is a function of the total surface area, efficiency of the cooling fins and the convection film coefficient of the fluid.

The frame/ambient film coefficient was determined from experimental tests on the motor. The motor was run at a constant load until thermal equilibrium was reached, h_f was then determined using $Q = hA\Delta\theta$ since the ambient and surface temperatures as well as the total loss in the machine are available. Table 5.2. compares the experimental result with that calculated analytically using Eq.(4.35).

Method	Film coefficient $(W/m^2\ ^0C)$
Analytical at turbulent	227.97
Experimental	295.33

Table 5.2: Film coefficient between the frame and the ambient

The remaining film coefficients used in the induction motor model are determined as described in chapter 4 and summarised in Table 5.3. Their accuracy can only be

justified against the experimental findings of some authors [30,76,26,73,70] and the final performance of the induction motor thermal model.

Component	Film coefficients $W/^0C\ m^2$
Frame/Ambient	295.33
air gap	150.50
End winding/Endcap air	26.8
Endcap air/End shield	20.0
Contact Stator core/Frame	416.67

Table 5.3: Film coefficients used in the equivalent thermal circuit

5.4 Setting up and solving the network equations

Once all the thermal blocks have been represented, they are linked and where appropriate the admittances are lumped together to give the resultant equivalent circuit shown in Fig. 5.3. The model has seventeen nodes in total, nine of which represent the mean temperature of the elements; whilst the remaining eight, five are secondary nodes of the cylindrical conduction model, and the remaining nodes form links between the elements.

The setting up of the equations is dictated by the conservation of heat flow balance, ie, the net flow of heat into any node must be equal the heat flowing out.

$$G_1(\theta_1 - \theta_a) + G_{12}(\theta_1 - \theta_2) + G_{13}(\theta_1 - \theta_3) + \ldots + G_{1n}(\theta_1 - \theta n) + C_1\frac{d\theta_1}{dt} = Q_1$$
$$G_2(\theta_2 - \theta_a) + G_{21}(\theta_2 - \theta_1) + G_{23}(\theta_2 - \theta_3) + \ldots + G_{2n}(\theta_2 - \theta n) + C_2\frac{d\theta_2}{dt} = Q_2$$
$$\vdots \quad \vdots \qquad\qquad \vdots$$

$$G_n(\theta_n - \theta_a) + G_{n1}(\theta_n - \theta_1) + G_{n2}(\theta_n - \theta_2) + \ldots + G_{n,n-1}(\theta_n - \theta_{n-1}) + C_n \frac{d\theta_n}{dt} = Q_n$$

In matricial form the equations can be expressed as

$$[G][\theta] + [C]\left[\frac{d\theta}{dt}\right] = [Q] \tag{5.16}$$

where

G_{ij}:is admittance connecting node i to node j

G_i:is self admittance of node i

θ_i:is the temperature at node i

Q_i:is the loss at node i

C_i:is the thermal capacitance

At steady state the above equations reduces to

$$\begin{aligned}
G_1(\theta_1 - \theta_a) + G_{12}(\theta_1 - \theta_2) + G_{13}(\theta_1 - \theta_3) + \ldots + G_{1n}(\theta_1 - \theta n) &= Q_1 \\
G_2(\theta_2 - \theta_a) + G_{21}(\theta_2 - \theta_1) + G_{23}(\theta_2 - \theta_3) + \ldots + G_{2n}(\theta_2 - \theta n) &= Q_2 \\
\vdots \quad \vdots \qquad\qquad \vdots & \\
G_n(\theta_n - \theta_a) + G_{n1}(\theta_n - \theta_1) + G_{n2}(\theta_n - \theta_2) + \ldots + G_{n,n-1}(\theta_n - \theta_{n-1}) &= Q_n
\end{aligned}$$

In a matricial form

$$[G][\theta] = [Q] \tag{5.17}$$

where

$[Q]$: is a column vector of heat sources

$[G]$: is the thermal admittance matrix

$[\theta]$: column of nodal temperature

Since there are 17 nodes the problem reduces to a simple system of seventeen simultaneous linear equations which is symmetrical about the diagonal. The system can

be solved using for, example, the Gauss method to give the temperature at all the nodes.

5.5 Temperature measurements

5.5.1 Selection of measurement points

In order to provide a suitable reference against which the thermal model performance could be compared thermocouples should be located at points considered to approximate to the mean temperature of the accessible model elements. Considerable care was taken in the selection of points at which to measure the temperature. In particular, points that have to coincide with the mean temperature of each element. The position of the mean temperatures were found by equating the mean temperatures to their equivalent profile. Appendix B explains in detail how these positions can be found.

5.5.1.1 Mean temperature position in case of axial heat flow

Since there is no external heat input from either side of the motor and the assumption of uniformly heat generation within the element Eq.(B.46) applies. Since symmetry is assumed about the radial plane passing through the middle of the motor, the middle point is taken as the origin from which the mean temperature position regarding the axial heat flow results.

$$x_{av} = \frac{h}{\sqrt{3}} \tag{5.18}$$

5.5.1.2 The position of the mean temperature in case of radial heat flow

There are three cases of radial heat flow:

1. No internal heat generation

   Eq.(5.20) arises from comparing Eqs. (B.39) and (B.40) with $Q_1 = 0$,

$$r_{av} = r_2 \exp -\frac{1}{2}\left(1 - \frac{r_1^2}{r_2^2 - r_1^2}\ln(r_2/r_1)\right) \tag{5.19}$$

2. Only heat generation is involved

   Eq.(B.38) applies and is of the form,

$$r_{av}^2 - 2r_1^2 \ln r_{av} + r_1^2\,(2\ln r_2 - (1-2B)) - \frac{r_2^2 + r_1^2}{2} = 0 \tag{5.20}$$

3. In a combination of the two cases, heat generation and external heat flow both occur.

   The assumptions made regarding the flow of heat are,

   - All losses generated in the rotor flow to the stator teeth through the air gap
   - The proportion of heat from embedded windings that flows into the teeth and back iron is proportional to the contact surface area.
   - Only the embedded winding copper loss contribute to the heating of the teeth and back iron, in other words heat generated in the end winding flows entirely to the endcap air.

$$r_{av}^2 + 2\frac{Q_1}{Q}\left[r_2^2 - r_1^2\left(\frac{Q}{Q_1} + 1\right)\right]\ln(r_{av}/r_2) = -\frac{4k_r\pi h(r_2^2 - r_1^2)}{Q}A \tag{5.21}$$

   where

$$A = \frac{Q}{4k_r h\pi(r_2^2 - r_1^2)}\left[\frac{r_2^2 - r_1^2}{2} - r_1^2(1-2B)\right] + \frac{Q_1}{4\pi k_r h}(1-2B)$$

The value of r_{av} depend on the ratio of the loss generated to the loss flowing from an external source, and may be found using the Newton-Raphson iterative technique.

5.6 Location of thermocouples

For the stator teeth, back iron and frame, this involved drilling holes to a depth given by previous equations according to the type of losses involved, and at an axial position which corresponded to the mean of the parabola, symmetric about the axial centre of the motor. Though, axial thermal symmetry was assumed, thermocouples were allocated to both ends (drive and nondrive) of the motor and the average measured temperature was taken. Some problems were encountered in allocating thermocouples to the embedded winding and end winding, at points which were specified by the model. In these cases, to obtain the temperature of the desired point, the temperature of some nearby point was taken. Generally, the location of thermocouples was governed by the availability of a suitable site. Three thermocouples were strapped to the end windings on both ends of the motor. Mechanically the sensors were held by their leads against the windings with a lacing cord. It is important that the tips of the sensors are in actual physical contact with the winding.

In addition, thermocouples were located at the point of interest, i.e. endcap air, end shield, ambient air. In order to monitor the rotor temperature, six thermocouples were placed in the rotor; at the surface, bar, iron, end ring, shaft, bottom of a tooth of rotor. To survey the temperature of the frame six thermocouples were placed around the circumference of the motor frame. Fig. 5.4 shows the thermocouples positions for half section of the motor.

A special thermal glue (epoxy) was employed to ensure a good thermal contact between the thermocouple and its surroundings. Care was taken in applying the epoxy around and over the tips of the sensors to be sure that epoxy flows under the sensor to fill any voids between the tip and the underlying surface. The epoxy provides a path for conduction of heat to the sensor, but an excess of epoxy will increase its mass and degrade the thermal response time of the sensor.

5.7 Results and discussions

The results from the thermal model were checked against measurements made on a 4kW squirrel cage induction motor which was similar to that used for the measurement of the loss density distribution. For this test the thermocouples were located at positions as near as possible to the mean temperature of the bulk elements, which implies that a direct comparison could be made with the results obtained from the solution of the simultaneous equations.

Table 5.4 shows the comparison between the predicted and measured steady state temperatures when the machine is on full load.

It can be seen that there is good correlation between the predicted and measured temperatures in the stator. For the winding, there is a small discrepancy which can be probably attributed to the crude and simplistic representation of these windings and the difficulty encountered in using the correct thermal coefficients. However in the rotor there is, in general, poor agreement because the temperatures are difficult to measure.

Component	Measured temperature (^0C)	Predicted temperature (^0C)
Frame	61.4 (av.7, surface)	66.62
Stator iron	72.2 (av. of 2)	69.52
Stator teeth	77.0 (av. of 2)	75.05
Embedded winding	102.1	94.33
End winding	110.0 (av. of 6)	109.15
Air gap	135	124.69
Rotor winding	-	151.11
rotor iron	128.8	150.4
Shaft	110.2	112.27
Endcap air	71.7	83.89

Table 5.4: Comparison of full load steady state temperatures

5.7.1 Effect of stray load losses on the machine heating

Table 5.5 shows the effect of stray load losses on the heating of the different components. It can be seen from the result that, based on the distribution used in this thesis, that the rotor is most affected by stray load loss. The inclusion of 27 W led to an increase in the rotor winding by 13^0C. Thus neglecting stray load losses which is generally the case in small induction motors may lead to misleading results, especially when using temperature as a main indicator in system protection.

5.8 Sensitivity analysis

To gain confidence in the modelling, in particular the allocation of losses and the specification of thermal properties, parametric studies are performed to show the sensitivity of the temperature distribution to these parameters.

Component	Predicted temperature (^0C)		
Stray load losses (W)	0	25	27
Frame	64.29	66.62	66.81
Stator iron	67.12	69.53	69.72
Stator teeth	72.28	75.05	75.27
Embedded winding	91.62	94.33	94.55
End winding	106.39	109.15	109.37
Air gap	115.78	124.69	125.40
Rotor winding	138.91	151.11	152.08
rotor iron	138.29	150.40	151.37
Shaft	104.94	112.27	112.86
Endcap air	80.34	83.89	84.17

Table 5.5: The effect of stray load losses on the temperature rise of the machine

5.8.1 Sensitivity to loss distribution

To investigate the influence of the loss distribution on the thermal model, small increments of each type of loss was injected at the appropriate node and the new temperature noted.

The result of the analysis of the variation of temperatures with 20% increase in losses for the major components is shown in Table 5.6, while Fig. 5.5 shows typically how temperature distribution is affected by variation in rotor losses. It can be seen that the rotor temperature is most sensitive to the rotor losses whilst the other components remain relatively unaffected. The thermal model shows clearly the importance of the accurate allocation of losses to the model. With the knowledge of iron loss distribution the thermal model is an accurate model by which one can determine the influence of other parameters. The heating of the embedded winding is particularly susceptible to the change of the losses in the near environments, the increase of its own losses only leads to a small uniform rise of temperature of the

motor.

	Predicted temperature (^0C)				
Components	Rotor	Stat. teeth	Embed. Wdg.	End Wdg.	Comp. varied
Losses (W)	149.8	30.4	119.1	101.4	None
Pred.Temp.	150.40	75.44	94.33	109.15	
Losses (W)	179.76	30.4	119.1	101.4	Rotor
pred. temp.	183.78	83.16	102.14	117.04	
Losses (W)	149.8	36.48	119.1	101.4	Stat. teeth
pred. temp.	153.68	77.71	96.79	111.56	
Losses (W)	149.8	30.4	142.92	101.4	Emb. Wdg.
pred. temp.	156.30	80.44	101.68	116.32	
Losses (W)	149.8	30.4	119.1	121.68	End Wdg.
pred. temp.	155.96	80.02	100.85	118.63	

Table 5.6: The influence of changes in losses on the heating of the important components

5.8.2 Sensitivity to the heat transfer coefficients

The sensitivity of the equivalent thermal network to film coefficients was investigated in similar manner by varying heat transfer coefficients. Table 5.7 summarises the results and show that the model is most sensitive to the frame ambient film coefficient. The predicted temperatures indicate that the rotor winding temperature is the most sensitive and account for approximately 4.5% variation in the estimated temperature. However, the variations in other parameters have little effect on the model.

The variations of temperature with the change in thermal conductivity values was also investigated and it was found that the model is not sensitive to changes in thermal conductivities. The effect of a range variation of the thermal coefficient on

the heating of major components of the model is shown in Fig. 5.6.

	Predicted temperature(^0C)				
Film coefficient	Rotor	Stat. teeth	Embed. Wdg.	End Wdg.	Endcap air
zero increase	151.11	75.05	94.33	109.15	83.89
Frame/Ambient	146.66	70.70	89.77	104.54	78.39
$\Delta\theta$	-4.45	-4.35	-4.56	-4.61	-5.5
Endcap air	152.12	77.61	96.53	111.04	85.03
$\Delta\theta$	1.01	2.56	2.2	1.89	1.14
Insulation	153.62	77.71	93.21	108.12	84.89
$\Delta\theta$	2.51	2.66	-1.12	-1.03	1.00
airgap	144.26	77.88	96.90	111.60	84.38
$\Delta\theta$	-6.85	2.83	2.57	2.45	0.49

Table 5.7: The effect of changes in heat coefficient on the heating of major blocks

5.9 Conclusion

It has been shown that if satisfactory heat transfer data is available the thermal model developed may be applied to predict the temperature distribution with a high degree of confidence. The temperature distribution has also been shown to be sensitive to other parameters, such as loss distributions, which can affect the temperature significantly. Hence the method of loss density measurement described in chapter 3 is potentially a very important link in any thermal model.

Given the accuracy of the thermal model, it is possible to predetermine the ratings and duty cycles of motors which, in turn allows the designer more freedom for evolving better thermal design.

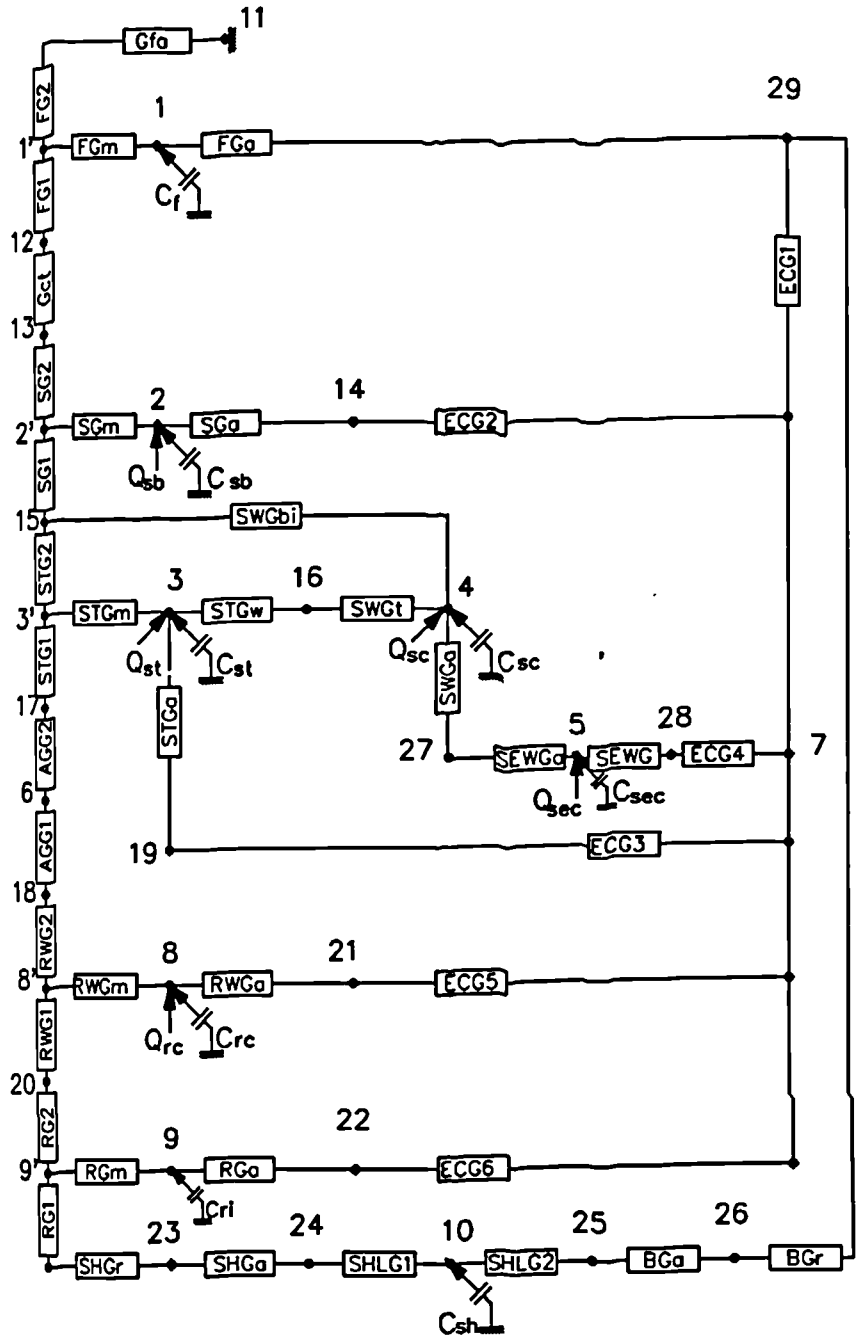

Prefixes

F: Frame	RW: Rotor winding
S: Stator	R: Rotor iron
ST: Stator teeth	SH: Shaft
SW: Stator winding	SHL: Shaft link
SEW: Stator end winding	B: Bearings
AG: Airgap	EC: Endcap

Fig. 5.1 Equivalent thermal circuit of induction motor.

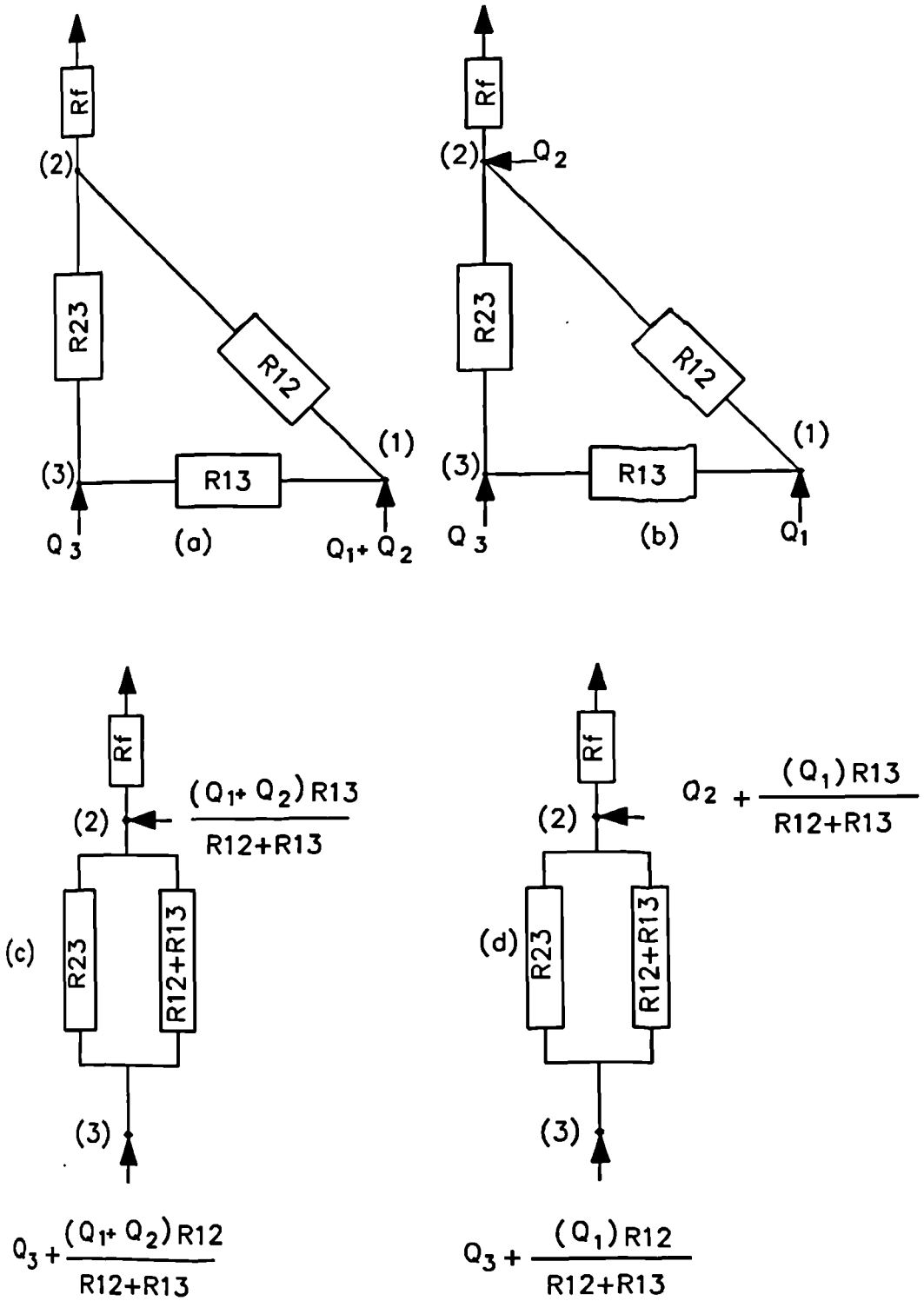

Fig. 5.2 Teeth/back iron lumped parameter configurations

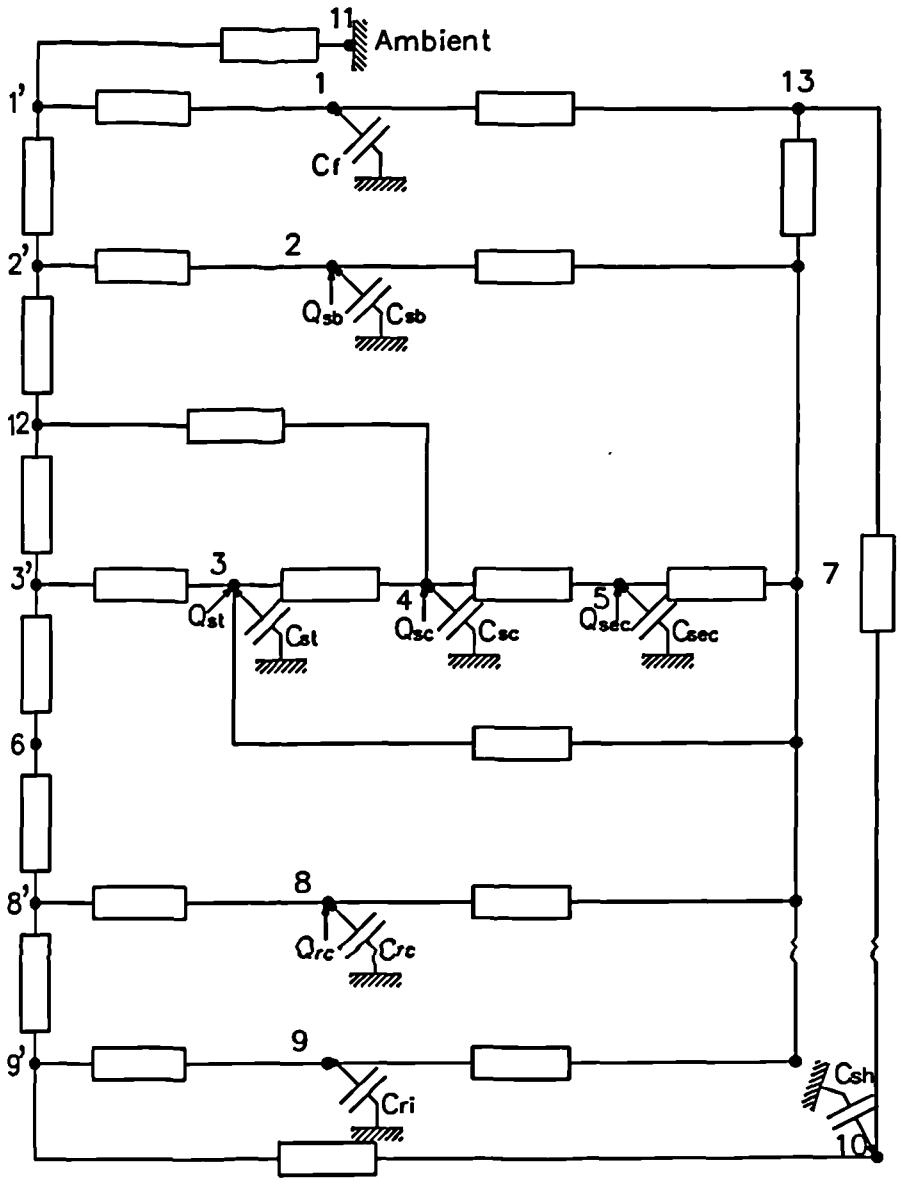

1) Frame 2) Back iron 3) Teeth
4) Embedded winding 5) End winding
6) Airgap 7) Endcap air 8) Rotor winding
9) Rotor iron 10) Shaft 11) Ambient
13) Link for shaft, endcap air and frame

Fig. 5.3 Resultant equivalent thermal circuit of an induction motor.

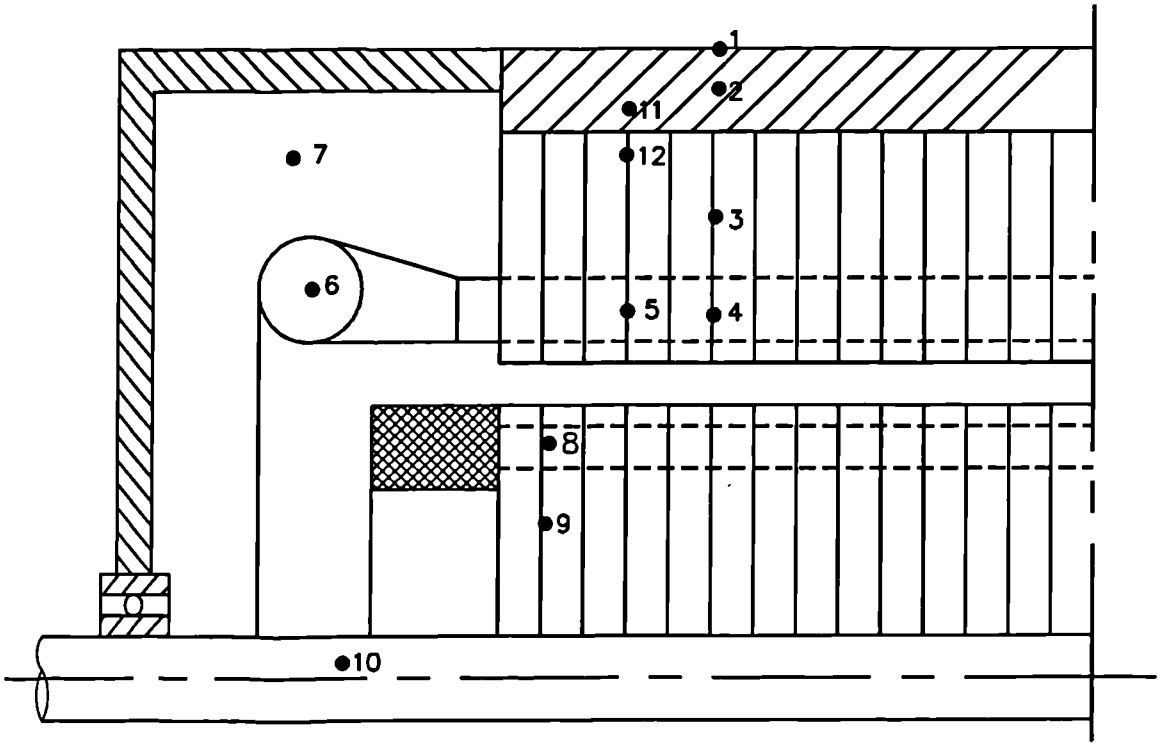

1) Frame surface
2) Frame
3) Back iron
4) Teeth
5) Embedded winding
6) End winding
7) Endcap air
8) Rotor winding
9) Rotor iron
10) Shaft
11, 12) Frame/back iron (contact resistance)

Fig. 5.4 Section of an induction motor showing location of thermocouples.

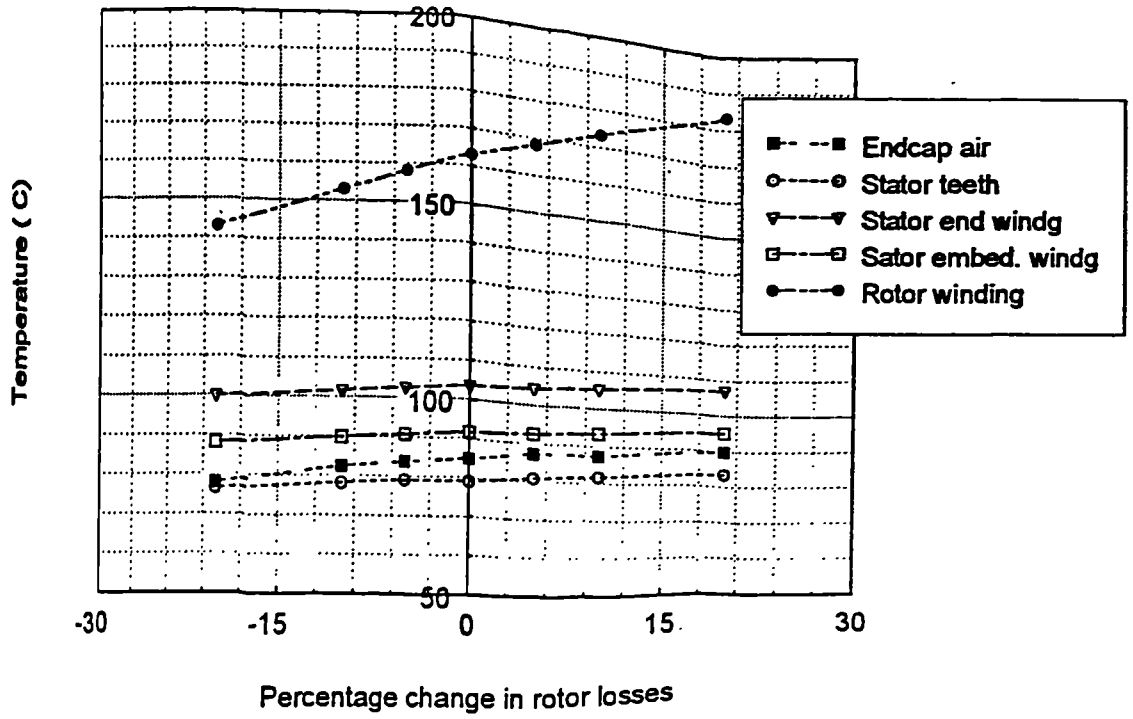

Fig. 5.5 Sensitivity of predicted temperature to rotor copper loss.

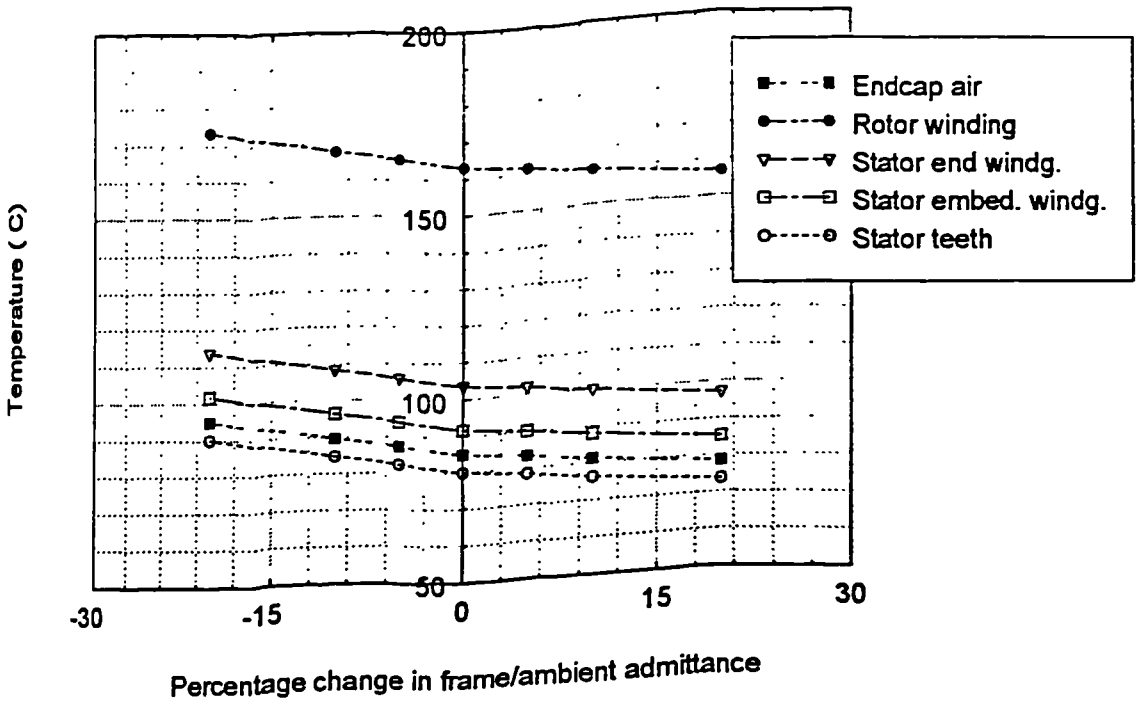

Fig. 5.6 Sensitivity of predicted temperature to frame/ambient admittance.

Chapter 6

In-situ determination of thermal coefficients

6.1 Introduction

There is often an enormous spread in experimental values of thermal conductivity even of common materials, without it being at all clear whether the divergence is due to difference between samples or to inaccurate measurements. Reported values of thermal conductivity for a particular material can differ considerably, in some cases differing by a factor of 10 [32]. However, differences are to be expected since no material is truly reproducible. Reliable data can only be acquired by being aware of the difficulties and pitfalls which are prevalent in the determination of this property. However, the theory of thermal conductivity in solids is unlikely to be dealt with thoroughly because of the difficulties involved in a rigourous treatment [31].

If, however, the conductances between the parts are obtained directly by the analysis

of test results of tests on a machine an equivalent specific thermal conductivity can be determined which can be used with confidence on other machines embodying a similar type of construction. Bates and Tustin [83] proposed a method for the determination of these coefficients from test results. This method relies on contriving tests in which only one element is subjected to loss at any one time. This method is, in general, very difficult to realise. An alternative approach adopted here is to derive a thermal lumped parameter model based on a new symmetrical equivalent circuit. The basis of this method is discussed in detail in the next sections.

6.2 Derivation of the modified thermal network equations

It can be seen from section 5.4 that at steady state the set of linear simultaneous equations can be expressed as

$$[G][\theta] = [Q] \tag{6.1}$$

where

$[Q]$: is the loss vector

$[G]$: the admittance matrix

$[\theta]$: the temperature vector

The temperature distribution $[\theta]$ can be obtained by inverting the matrix equation, Eq. (6.1), i.e.

$$[\theta] = [G]^{-1}[Q] \tag{6.2}$$

The accurate solution of Eq. (6.2) is contingent upon the correct specification of the components of $[G]$, which depends on both the dimensions of the machine and the thermal characteristics of the materials used in its construction. The dimensions of the machine are usually well defined but considerable uncertainties exist in the thermal properties, in particular when the materials are treated, machined, or when they are lumped together to form a composite mass, for example the copper, lacquer, air, and insulation combination of the stator windings. Uncertainties arise as it is usual for manufacturers to specify only the characteristics of individual untreated materials. Hence a method which allows the in-situ assessment of $[G]$ and, hence, the thermal coefficients of the material will be most beneficial.

Such a method could be developed by considering Eq. (6.1). If the equations are rearranged so that the network admittances, $[G]$, become the unknown variables, then Eq. (6.1) can be rewritten as,

$$[\theta][G] = [Q] \tag{6.3}$$

Eq. 6.3 cannot be inverted to give the network admittances because $[\theta]$ is not a square matrix. This can be deduced by considering a simple case of two conductances connected to an active node, as shown in Fig. 6.1, where the heat balance equation is given by

$$Q_0 = G_{01}(\theta_0 - \theta_1) + G_{02}(\theta_0 - \theta_2) \tag{6.4}$$

It can be seen that even if $\theta_0, \theta_1, \theta_2$ and Q_0 are known, G_{01} and G_{02} cannot be determined. To enable G_{01} and G_{02} to be determined another thermal state must be defined, i.e.

$$Q'_0 = G_{01}(\theta'_0 - \theta'_1) + G_{02}(\theta'_0 - \theta'_2) \tag{6.5}$$

so that the simultaneous solution of Eqs. (6.4) and (6.5) will yield G_{01} and G_{02}. This analysis can be extended to the case of n isolated conductances confluent at a node

in which n-thermal states must be available. Note, however, that for the case of a non-active node, ($Q_0 = Q'_0 = 0$), there will be no solution to Eqs. (6.4) and (6.5).

For a totally connected network, of n nodes, the number of unknowns or branches, assuming the effect of reciprocity $G_{ij} = G_{ji}$, is given by

$$NG = \frac{n^2 + n}{2} \tag{6.6}$$

whilst Eq. (6.3) represents a system of only n equations where, in general, $NG > n$. By imposing other thermal conditions on the network sufficient additional equations can be generated to allow Eq. (6.3) to be inverted i.e.

$$[G] = [\theta]^{-1}[Q] \tag{6.7}$$

to give the network admittances.

The number of extra equations needed to solve the system of NG variables is

$$NE = \frac{n}{2}(n-1) \tag{6.8}$$

Each load test generates n equations and since the number of equations required is NG, thus the number of tests required are

$$NT = \frac{NE}{n} + 1 \tag{6.9}$$

Therefore, in an interconnected network, at least two thermal states are required, depending on the number of the conductances to be evaluated. In general 2-thermal states, giving rise to $2n$ equations, will be sufficient for solving the network admittance assuming that, in practice, [G] does not vary significantly with temperature.

6.2.1 Model of the thermal circuit conductances

As shown in section 6.2 only active nodes may be used for determining the thermal coefficients of the equivalent thermal circuit. However, in chapter 4, it has been shown that utilising a 'T' equivalent circuit always results in an inert node. Hence, the alternative is to develop a topology which does not contain an inert node but still represents the heat flow conditions.

Fig. 6.2a shows the 'T' equivalent thermal circuit which has been developed in Appendix B. To eliminate the inert node a new symmetrical equivalent circuit shown in Fig. 6.2b is used. The total heat generated originally, Q, is now allocated to three nodes. To obtain symmetry in the network, identical losses are injected at node 1 and 2, whilst the remaining losses are imposed at node 3. Given this allocation of losses the exact proportion can now be determined by considering the analytical temperature distributions, as described in appendix B, i.e.

$$\theta_1 = \theta_2 + \frac{R_0}{2}Q + R_0 Q_1 \tag{6.10}$$

and

$$\theta_{av} = \theta_2 + \frac{R_0}{3}Q + \frac{R_0}{2}Q_1 \tag{6.11}$$

Using the equivalent circuit shown in Fig. 6.2b the temperature distribution is given by

$$\begin{aligned} \theta_1 &= \theta_2 + \frac{R_0}{2}\left[Q_1 + Q(1-\alpha)\right] + \frac{R_0}{2}(Q_1 + \alpha Q) \\ &= \theta_2 + R_0 Q_1 + \frac{R_0}{2}Q \end{aligned} \tag{6.12}$$

whilst the mean temperature is given by

$$\theta_{av} = \theta_2 + \frac{R_0}{2}[Q_1 + Q(1-\alpha)] \tag{6.13}$$

where α is the ratio of the losses situated in node 1 or 2 to the total losses in the slab.

Comparison of Eqs. (6.10) and (6.12) that the thermal network of Fig. 6.2b represents the true temperatures θ_1 and θ_2 and independent on the coefficient α. Comparing Eqs. (6.11) and (6.13), however, show that for the average temperature of the two network to be equivalent then

$$\alpha = \frac{1}{3}$$

In a similar manner the 'T' equivalent circuit for a cylinder, shown in Fig. 6.3a and developed in appendix B, can be transformed to the circuit shown in Fig. 6.3b.

For the 'T' equivalent circuit of Fig. 6.3a the temperature distribution is given by

$$\theta_1 = \theta_2 + (R_1 + R_2)Q_1 + R_2Q \tag{6.14}$$

$$\theta_{av} = \theta_2 + (R_m + R_2)Q + R_2Q_1 \tag{6.15}$$

whilst using the equivalent circuit shown in Fig. 6.3b the temperature distribution is given by,

$$\theta_1 = \theta_2 + Q[R_1\alpha_1 + R_2(\alpha_1 + \alpha_2)] + (R_1 + R_2)Q_1 \tag{6.16}$$

$$\theta_{av} = \theta_2 + QR_2(\alpha_1 + \alpha_2) + R_2Q \tag{6.17}$$

Comparison of Eqs. (6.14),(6.16) and (6.15),(6.17) respectively, shows that for equivalence

$$\alpha_1 = -\frac{R_m}{R_1} \tag{6.18}$$

$$\alpha_2 = \frac{R_m}{R_2} - \alpha_1 + 1 \tag{6.19}$$

and hence,

$$\alpha_3 = 1 - (\alpha_1 + \alpha_2) \tag{6.20}$$

Based on the original thermal network of the motor fig. 6.4 the modified equivalent circuit shown in Fig. 6.5. is obtained.

6.3 Implementation of the method

6.3.1 General consideration in the measurement of thermal conductivity

The methods of measuring the thermal conductivity can be divided into two categories, static and dynamic, depending on whether the temperature distribution within the sample is time dependent. Static measurements involve the use of Fourier's law of conduction, and it is necessary to determine the heat flow density and the temperature gradient along the normal to the isothermal surface. In contrast to the steady state measurements, dynamic methods involve the complete differential heat equation in accordance with Poisson's equation. In general, these methods determine the diffusivity and require measurement of the time for thermal disturbance to propagate a known distance. The specific heat and density must be known in order to obtain the thermal conductivity. The steady state condition assists in the achievement of a high degree of precision of measurement, although the total time involved in achieving equilibrium can be a very lengthy process. The long time constant also makes steady state methods undesirable at very high tempera-

tures. Dynamic methods, in general do not give as high a precision as static ones although modern instrumentation is improving enormously the precision attainable with this type of method.

The choice of method of measurement depends upon the order of magnitude of the thermal conductivity to be evaluated, on the temperature range, and on the sample size. Dynamic techniques are preferred to the static with the desire to obtain data rapidly, particularly at high temperatures [31].

In the static method, chosen for this application because of the lower temperature which exist in the machine, the thermal conductivity is obtained from measurements of a temperature gradient together with the heat flow density into or out of the sample in accordance with Fourier's law. In general, measurement of heat flow, and the cross sectional area present no problem. However, it is necessary to pay great attention to the measurement of temperatures, since thermal conductivity may vary with temperature. Whilst this variation can be quite marked for individual materials its effect may be much less for lumped model of composite materials. Fig. 6.6 shows that the placement of thermocouples and their locations which are the same as those discussed in previous chapter. Other thermocouples of interest have been allocated at the back iron/teeth interface, external surface of a tooth.

In order to compare the performance of the new equivalent thermal circuit with the original, the value of the coefficients related to the loss distribution, α_i, used to solve the equivalent thermal circuit are determined and summarised in Table 6.1, and Table 6.2 gives the predicted temperature values for the two types of the equivalent thermal circuit. It can be seen the two circuit perform well and give relatively the same results.

Coefficients	Magnitude of the coefficients		
	Stator back iron	Stator teeth	rotor winding
α_1	0.308	0.302	0.320
α_2	0.334	0.335	0.333
α_3	0.358	0.363	0.347

Table 6.1: The values of coefficients for the distribution of losses at three nodes

Component	Predicted temperature (^0C)	
Type of loss dist.	At 3 nodes	At mean node
Frame	63.0	66.62
Stator iron	67.37	69.53
Stator teeth	80.93	75.05
Embed. wndg	88.27	94.33
End winding	100.49	109.15
Air gap	114.64	124.69
Rotor winding	151.78	151.11
rotor iron	150.95	150.40
Shaft	149.82	112.27
Endcap air	77.46	83.89

Table 6.2: The comparison of the predicted temperatures for different equivalent thermal circuits

It is worth mentioning that if the equivalent circuit in Fig. 6.5 would present the effect of the axial heat transfer, the axial admittances should be divided by the same coefficient by which the loss generated in the component is multiplied to find the loss to be injected at the node related to the mean temperature. The results indicate that the effect of increasing the axial resistances by such an amount has no effect on the temperature rise. It can be noticed from Table 6.2 that the mean temperatures of the rotor windings and rotor iron are almost the same due to good thermal contact which exists between the aluminium conductors and rotor laminations. The output

of thermocouples on the rotating parts was not accurate as it has been explained in chapter 4. It was assumed that a good contact existed between the rotor iron and the shaft so that the rotor parts are lumped together. Frame components are lumped with the contact resistance. Where possible, nonactive nodes are avoided by lumping together the appropriate components such as back iron axial resistance with the endcap resistance. The equivalent circuit of Fig. 6.5 is reduced to the equivalent circuit shown in Fig. 6.7. Nodes 2, 3 and 4 represent the stator back iron whereas 4, 5 and 8 represent stator teeth. The embedded and end windings are represented by nodes 6 and 7 respectively, and 9 and 10 are the rotor and endcap air. It can be noticed that each block has a common node with its adjacent component. At these nodes the total loss is the sum of the losses allocated to each component. The distribution of losses is based on the same approach as described in chapter 4.

6.3.2 Formulation of equations

Under full load conditions the system of equations arising from applying Kirchhoff's first law to the equivalent thermal circuit shown in Fig. 6.7 yields,

$$Q_1 = G_{12}(\theta_1 - \theta_2) + G_{19}(\theta_1 - \theta_9) + G_{1,10}(\theta_1 - \theta_{10}) + G_{1,11}(\theta_1 - \theta_{11})$$
$$Q_2 = G_{21}(\theta_2 - \theta_1) + G_{23}(\theta_2 - \theta_3)$$
$$Q_3 = G_{32}(\theta_3 - \theta_2) + G_{34}(\theta_3 - \theta_4) + G_{3,10}(\theta_3 - \theta_{10})$$
$$Q_4 = G_{43}(\theta_4 - \theta_3) + G_{45}(\theta_4 - \theta_5) + G_{46}(\theta_4 - \theta_6)$$
$$Q_5 = G_{54}(\theta_5 - \theta_4) + G_{56}(\theta_5 - \theta_6) + G_{58}(\theta_5 - \theta_8)$$
$$Q_6 = G_{64}(\theta_6 - \theta_4) + G_{65}(\theta_6 - \theta_5) + G_{67}(\theta_6 - \theta_7)$$
$$Q_7 = G_{76}(\theta_7 - \theta_6) + G_{6,10}(\theta_6 - \theta_{10})$$
$$Q_8 = G_{85}(\theta_8 - \theta_5) + G_{89}(\theta_8 - \theta_9)$$
$$Q_9 = G_{98}(\theta_9 - \theta_8) + G_{91}(\theta_9 - \theta_1)$$

$$Q_{10} = G_{10,1}(\theta_{10} - \theta_1) + G_{10,3}(\theta_{10} - \theta_3) + G_{10,7}(\theta_{10} - \theta_7)$$

The term $G_{1,11}(\theta_1 - \theta_{11})$ represent the total heat flow from the fame, and represent the total loss in the machine which is a kown quantity. Taking the effect of reciprocity $G_{ij} = G_{ji}$ the above equations become

$$\begin{vmatrix} Q_1 \\ Q_2 \\ Q_3 \\ Q_4 \\ Q_5 \\ Q_6 \\ Q_7 \\ Q_8 \\ Q_9 \\ Q_{10} \end{vmatrix} = \begin{vmatrix} \theta_{12} & \theta_{19} & \theta_{1,10} & 0 & 0 & 0 & 0 & 0 & 0 & 0 & 0 & 0 & 0 \\ \theta_{21} & 0 & 0 & \theta_{23} & 0 & 0 & 0 & 0 & 0 & 0 & 0 & 0 & 0 \\ 0 & 0 & 0 & \theta_{32} & \theta_{34} & \theta_{3,10} & 0 & 0 & 0 & 0 & 0 & 0 & 0 \\ 0 & 0 & 0 & 0 & \theta_{43} & 0 & \theta_{45} & \theta_{46} & 0 & 0 & 0 & 0 & 0 \\ 0 & 0 & 0 & 0 & 0 & 0 & \theta_{54} & 0 & \theta_{56} & \theta_{58} & 0 & 0 & 0 \\ 0 & 0 & 0 & 0 & 0 & 0 & 0 & \theta_{64} & \theta_{65} & 0 & \theta_{67} & 0 & 0 \\ 0 & 0 & 0 & 0 & 0 & 0 & 0 & 0 & 0 & 0 & \theta_{76} & \theta_{7,10} & 0 \\ 0 & 0 & 0 & 0 & 0 & 0 & 0 & 0 & 0 & \theta_{85} & 0 & 0 & \theta_{89} \\ 0 & \theta_{91} & 0 & 0 & 0 & 0 & 0 & 0 & 0 & 0 & 0 & 0 & \theta_{98} \\ 0 & 0 & \theta_{10,1} & 0 & 0 & \theta_{10,3} & 0 & 0 & 0 & 0 & 0 & \theta_{10,7} & 0 \end{vmatrix} \begin{vmatrix} G_{12} \\ G_{19} \\ G_{1,10} \\ G_{23} \\ G_{34} \\ G_{3,10} \\ G_{45} \\ G_{46} \\ G_{56} \\ G_{58} \\ G_{67} \\ G_{7,10} \\ G_{89} \end{vmatrix}$$

Where $\theta_{ij} = \theta_i - \theta_j$

It is confirmed here that the number of unknowns in this particular case is equal to 13 whereas the number of equations that result from applying Kirchhoff's law is only 10. Thus, a further three equations are needed to fully define the problem. The extra equations can be obtained by running another test under different load conditions, at half load for example.

Inclusion of the extra equations results in a sparse matrix as shown in the above matrix. Solving the system needs the inversion of $[\theta]$. Standard inversion techniques, such as gaussian elimination and LU decomposition, were not suitable because the matrices which are generated are very close to singularity and consequently these fail to give satisfactory results. Instead a singular value decomposition (SVD) technique was applied for solving the problem [86]. Another advantage of the SVD technique is that, since running the machine under two load conditions results in more equations than unknowns, it allows an over-specification of equations.

6.4 Results

Solving the system of equations defined by two thermal states, full load and half load tests, yields the results shown in Table 6.3. Perhaps the most prominent results is the difference between the calculated thermal conductivity in the teeth and back iron, since the thermal conductivity of metals decreases with increasing temperature. In the original lumped parameter analysis it was assumed that these were of the same magnitude but this is likely incorrect and is substantiated by the much lower calculated thermal conductivity for the teeth. The results also show that the heat transfer coefficient from the end windings, which is lumped with the endcap region, is almost three times higher than the value given by Luke [75]. The endcap/frame film coefficient is approximately 50% higher. The calculated air gap coefficient, however, was very low compared to the figure obtained using Taylor [74] analysis. One of the reason for the discrepancy is the relatively inaccurate temperature measurements from the rotor.

The thermal coefficients obtained using this method were used in the solution of

Components	Thermal coef. calculated (W/m^0C)	Thermal coef. used $(W/m\ ^oC)$
Stator back iron(G_{23}) (along the lamination)	38.81	45.2
Stator back iron(G_{34}) (along the lamination)	38.71	45.2
Stator back iron($G_{3,10}$) (normal to the lamination)	1.82	1.97
Stator teeth(G_{45}) (along the lamination)	36.70	45.2
Stator teeth(G_{58}) (along the lamination)	36.98	45.2
Windg insulation(G_{46}) plus slot liner	0.10	0.125
End windg/endcap air($G_{7,10}$)	97.27 $(W/^0C\ m^2)$	26.8 $(W/^oCm^2)$
Air gap (G_{89})	21.62 $(W/^0C\ m^2)$	150.50 $(W/^oCm^2)$
Endcap air/end shield ($G_{1,10}$)	38.76 $(W/^0C\ m^2)$	20.0 $(W/^oCm^2)$

Table 6.3: Values of thermal coefficients

the original thermal equivalent circuit shown in Fig. 6.4. A comparison of the predicted and measured temperatures are shown in Table 6.4. Since the apparent thermal conductivity of the slot includes the slot liner, copper and its insulation, the modelling of the winding differs slightly from the previous case. The combination of slot liner plus copper and its insulation is modelled as a single homogeneous medium with an apparent thermal conductivity equal to the one found experimentally.

6.5 Conclusion

The accuracy of this method relies heavily on the accurate measurement of temperatures, and loss distribution. By conducting tests on a test machine all effects

Component	Predicted temperature (^0C)			Measured temp.
	$k_e = 0.1$ $W/m\ ^0c$	$k_e = 0.125$ $W/m\ ^0c$	$k_e = 0.1\ (W/m\ ^0)$ $h_{gap} = 150.5(W/^0c\ m^2)$	(^oC)
Frame	63.46	63.46	63.46	61.4
Stator iron	67.43	67.47	67.98	72.2
Stator teeth	73.99	74.12	75.80	77.0
Embed.Wndg.	112.03	105.87	107.11	102.1
End winding	118.34	112.22	112.59	110.0
Air gap	166.28	164.17	121.93	135.0
Rotor winding	241.46	240.07	153.22	-
rotor iron	238.98	237.60	152.12	128.8
Shaft	236.17	234.82	119.76	110.2
Endcap air	98.67	97.23	87.49	71.7

Table 6.4: The predicted temperatures rise using the thermal coefficients found experimentally

associated with the use of composite materials in the machine are taken into consideration. Thus the predicted thermal coefficients should be more accurate than those taken from tables, which are made under laboratory conditions, or those estimated using analytical techniques

The problem common to all methods of thermal measurement is the attainment of the ideal conditions of heat flow required mathematically. In fact Parrott and Stuckes [31] state that if these conditions are not met experimentally the data acquired could be meaningless. There are three possible major sources of error which may arise when determining the thermal conductivities, viz sample dimensional inaccuracies, errors in the measurement of heat flow and temperature. For a desired level of accuracy the first two sources are to a large extent scale dependent, i.e. the larger the machine the smaller will be the error. However, temperature measurement on the sample is subjected to uncertainties such as

- Distortion of heat flow in the immediate vicinity of the thermocouple tip
- Possibility of the thermocouple tip being in a small air pocket
- Inaccurate location of the thermocouple

The results presented show a good agreement with those presented by Roberts [30] and, hence, the method is a very promising tool for further development.

The equivalent thermal circuit has been shown to be capable of providing two important primary functions. Firstly, by the use of appropriately assumed values of heat transfer coefficients it is possible to predict the temperature rise in different parts of the motor. Secondly, by appropriate temperature measurements on an actual machine under two load conditions, and using the equivalent thermal circuit, thermal coefficients can be calculated and analysed with respect to the conduction and convection modes of heat transfer. Information on measured convection coefficients is sparse and, therefore, the application of this method will help to increase the available knowledge.

Using the experimental thermal coefficients yielded relatively the same predicted temperatures as those using the lumped parameter model. The results so obtained were about 10% lower than the experimental for some components, without being clear whether the discrepancy is due to the method or to inaccurate measurements. To assess the accuracy of the lumped thermal model localised temperature distribution using finite element method is used and described in the following chapter.

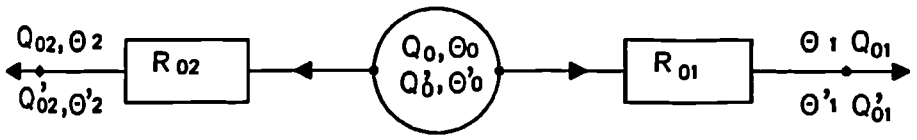

Fig. 6.1 Resistances Confluent at an active node.

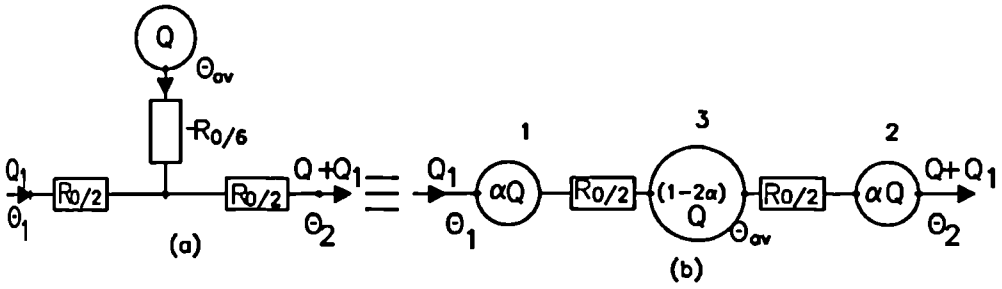

Fig. 6.2 Equivalent thermal circuits for heat flow through an active slab.

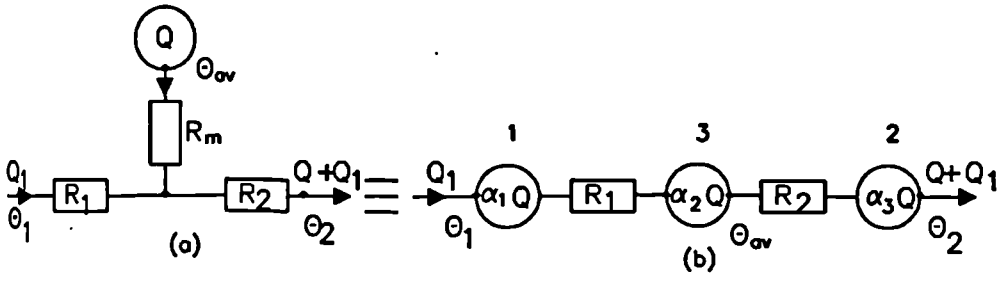

Fig. 6.3 Equivalent thermal circuit for outward heat flow from an active cylinder

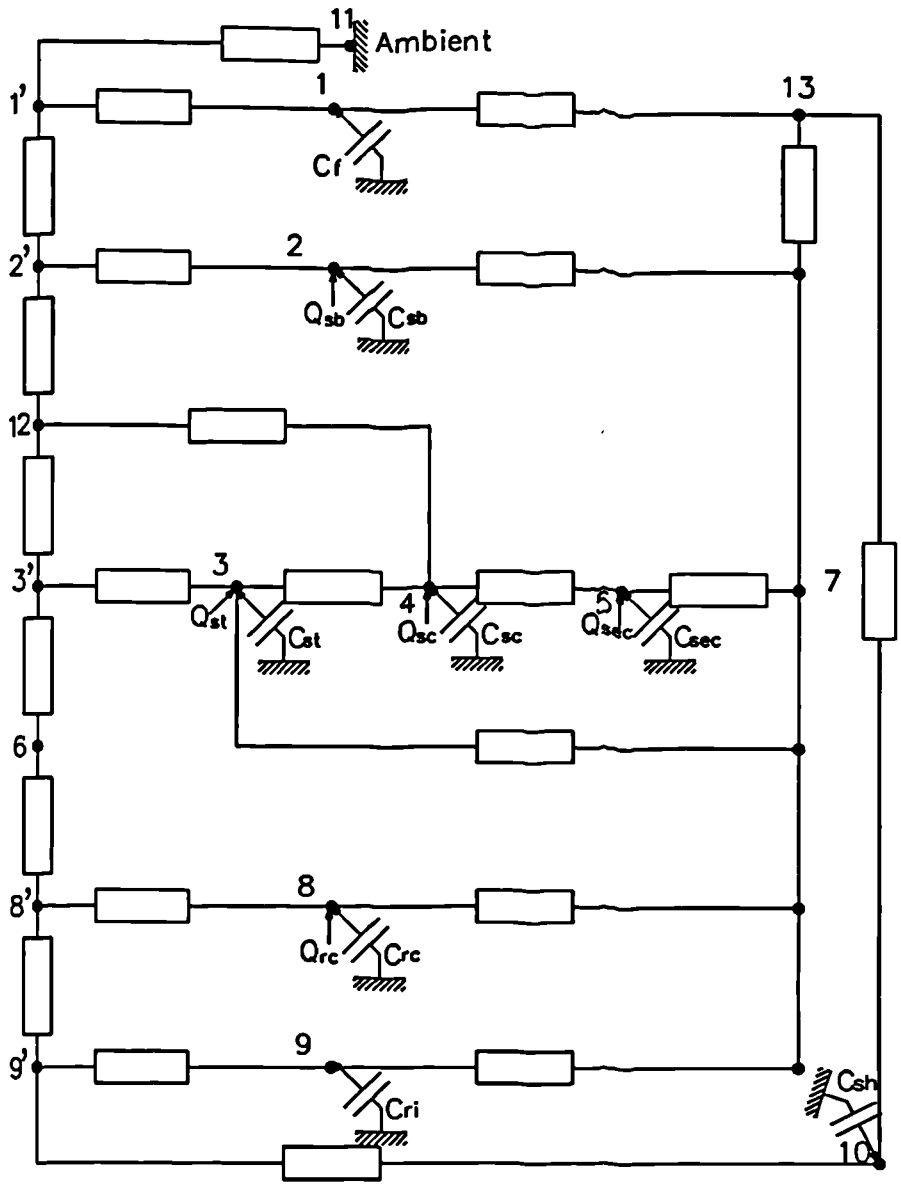

1) Frame 2) Back iron 3) Teeth
4) Embedded winding 5) End winding
6) Airgap 7) Endcap air 8) Rotor winding
9) Rotor iron 10) Shaft 11) Ambient
13) Link for shaft, endcap air and frame

Fig. 6.4 Resultant equivalent thermal circuit of induction motor.

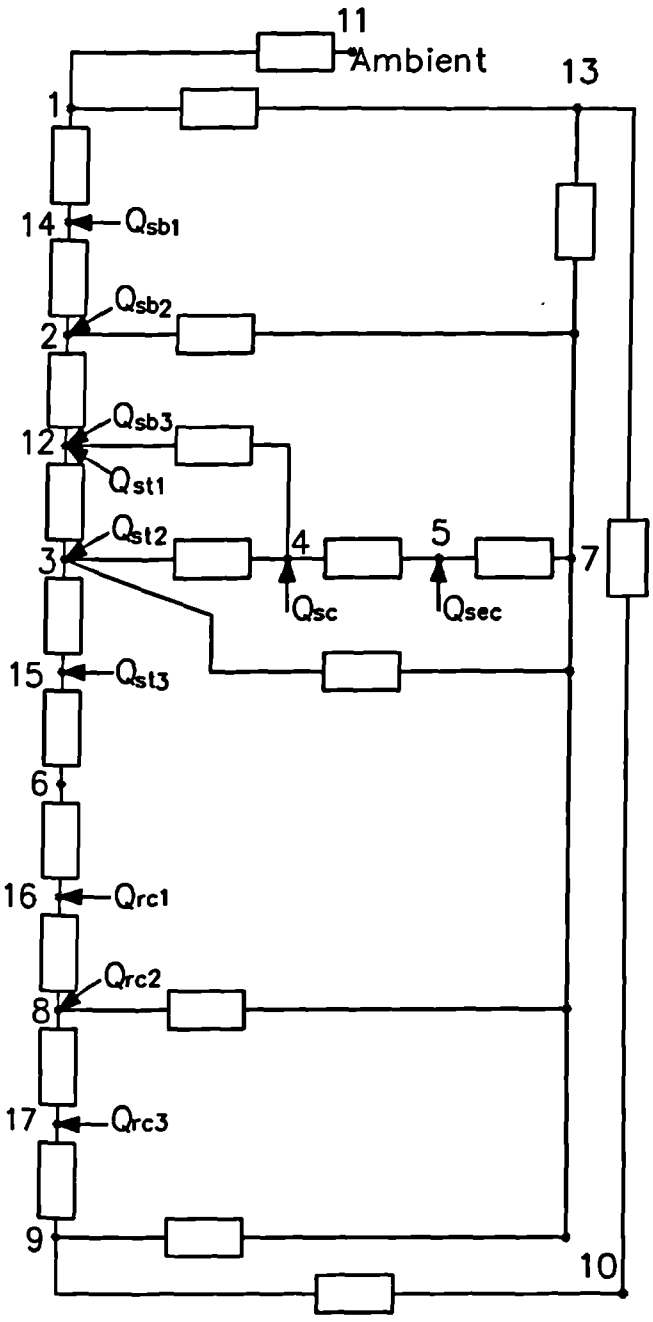

Fig. 6.5 Resultant equivalent thermal circuit based on 3 node loss distribution model.

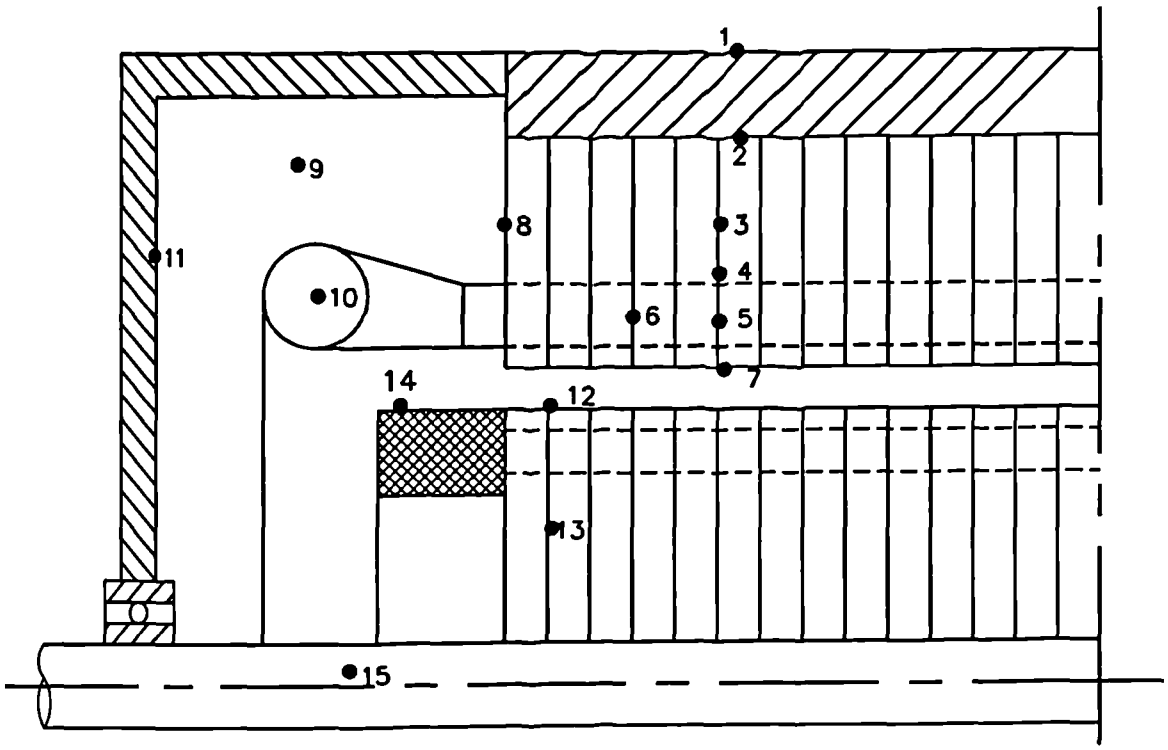

1) Frame
2) Frame/back iron interface
3) Stator iron
4) Back iron/teeth interface
5) Stator teeth
6) Slot winding
7) Tooth surface
8) Stator end lamination
9) Endcap air
10) End winding
11) Endcap
12) Rotor surface
13) Rotor iron
14) Rotor end ring
15) Shaft

Fig. 6.6 Section of an induction motor showing location of thermocouples

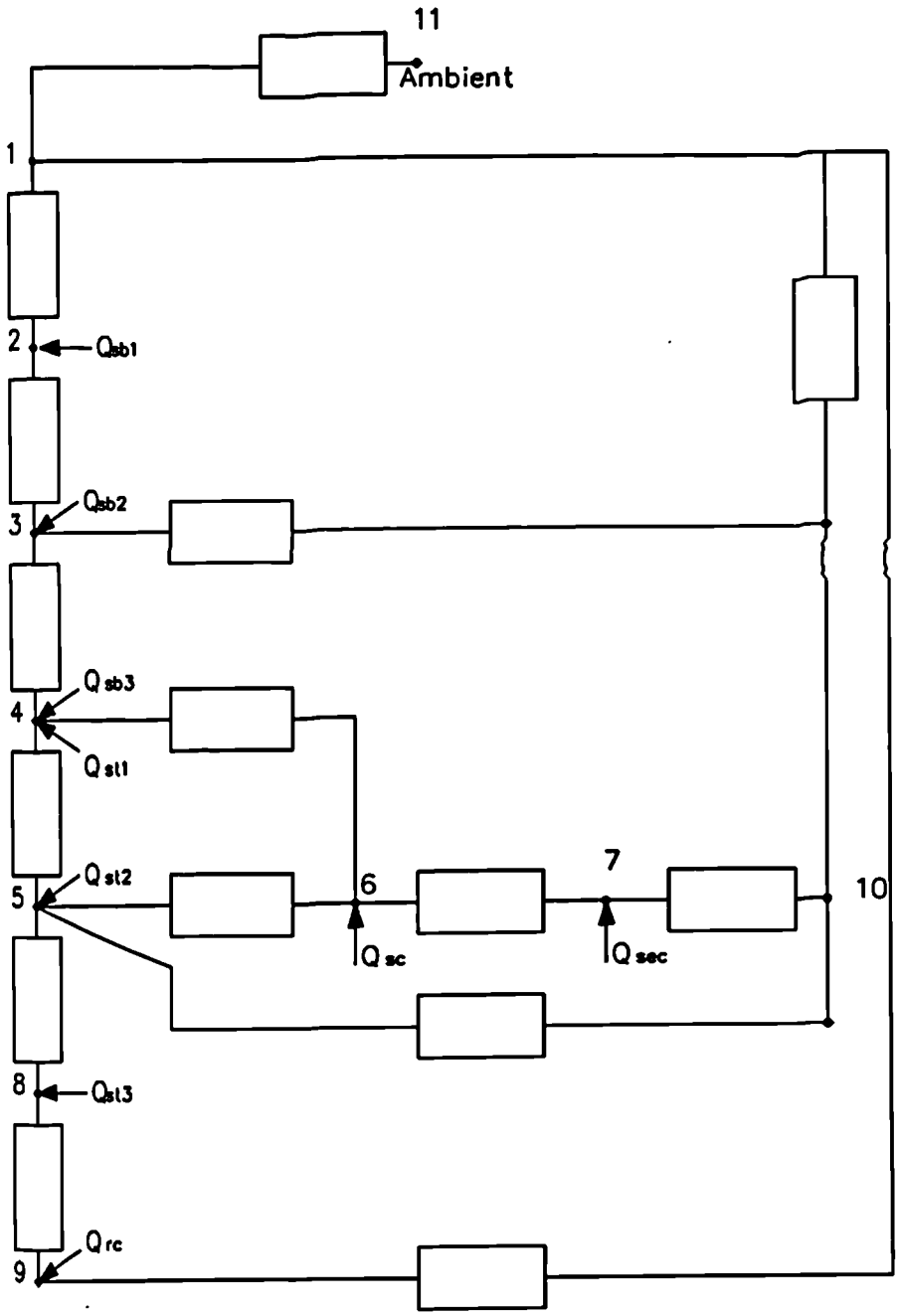

Fig. 6.7 Simplified equivalent thermal circuit.

Chapter 7

Finite element analysis of temperature distribution

7.1 Introduction

In the view of the trend towards smaller motors and exact ratings using computer derived optimum design, motors are being operated much nearer to their overload than ever before. To ensure satisfactory motor life time, the motor components temperature must remain within its designated limits. The success of any thermal protection depends heavily upon the motor physical phenomenon to predict the motor temperatures. The lumped parameter thermal model was used to predict the temperature rise given a knowledge of the loss distribution, thermal physical properties and dimensions of the motor. Although the method gives a relatively accurate temperature distribution on a 'macroscopic level' localised temperatures cannot be determined unless the lumped parameter model is further subdivided making the model very tedious and time consuming to generate and solve. To obtain

accurate localised temperature distribution numerical field solution techniques must be employed.

The finite element method, arguably the most versatile numerical technique for the solution of field problems governed by partial differential equations, is well established and easily adapted for solving a wide variety problems. One of the main reasons for the popularity of the method in different fields of engineering, is that once a general computer program is written, it can be used for the solution of any problem simply by changing the input data. Although the method has been extensively used in the field of structural mechanics, it has been successfully applied for solving other types of engineering problems for example heat transfer, electric and magnetic fields etc. [89].

Basically, this technique replaces the domain by a large number of simple shaped finite elements which could be either triangles or quadrilaterals. Each element is described by its nodal points, the larger the number of nodes per element, the higher the order and hence the more sophisticated and accurate will be the approximating function used for representing the field distribution. As with all numerical techniques the finite element method reduces the field problem to one of solving a finite set of simultaneous equation; the size of the set of the of equations being dependent on the level of discretisation. The generation of the matrix equations could be approached via a variational approach which is derived from minimisation principles. However, this is only possible if a functional, which when minimised satisfies the governing heat flow equation boundary conditions, can be found. Then, by considering the equilibrium at all the inter element boundaries, together with the imposed boundary conditions, a set of simultaneous equations can be obtained. The solution to the simultaneous equations will give nodal temperatures, from which other information, for example heat flow, can be obtained.

To analyse the temperature distribution in an induction motor, a two dimensional finite element computer package developed in this Department was used. The package is made up of two programs, MESHGEN and THERMAL which were originally developed for electromagnetic problems. MESHGEN allows the user to define and discretise the domain as required by the finite element method, to set the boundary conditions and heat sources. THERMAL is then executed to solve the temperature distribution and allows the user to analyse the results in detail. A more comprehensive description of the software can be found in references [87] [88].

7.2 Formulation of the problem

For two dimensional heat flow, the partial differential equation describing the steady state heat conduction is given by,

$$\frac{\partial}{\partial x}\left(k_x \frac{\partial \theta}{\partial x}\right) + \frac{\partial}{\partial y}\left(k_y \frac{\partial \theta}{\partial y}\right) + q = 0 \tag{7.1}$$

To ensure that the solution is unique, it is necessary to impose sufficient boundary conditions to fully define the problem. The more common boundary conditions, shown in Fig. 7.1, are:

- Dirichlet boundary conditions defined by,

$$\theta(x, y) = \theta_0 \tag{7.2}$$

- Neumann boundary conditions defined by,

$$k_n \frac{\partial \theta}{\partial n} + q'_{S_2} = 0 \tag{7.3}$$

$$k_n \frac{\partial \theta}{\partial n} + h_{S_3}(\theta - \theta_\infty) = 0 \tag{7.4}$$

where

n:outward normal direction to a surface

k_n:thermal conductivity in the normal direction

q:The heat density generated within the body

q'_{s_2}:the heat flux from the boundary S_2

$h_{S_3}(\theta - \theta_\infty)$:the surface heat flow due to convection from boundary surface S_3

It should be noted that the convection loss $h_{S_3}(\theta - \theta_\infty)$ and the heat flux q'_{S_2} must not occur in the same position on the boundary.

The solution of Eq. (7.1) can be obtained by formulating the scalar potential temperature problem in variational terms by an energy functional, and minimising with respect to a set of trial functions. Rao [89] has shown, through calculus of variations, that the functional which when minimised satisfies Eq. (7.1) is given by,

$$\begin{aligned} \Im &= \frac{1}{2}\int\int_R \left[k_x \left(\frac{\partial \theta}{\partial x}\right)^2 + (k_y \left(\frac{\partial \theta}{\partial y}\right)^2 - 2q\theta \right] dx dy \\ &+ \int_{S_2} q'\theta dS_2 + \frac{1}{2}\int_{S_3} h(\theta - \theta_\infty)^2 dS_3 \end{aligned} \tag{7.5}$$

The double integrals are taken over the region of interest R, the last two terms have been introduced to account for the imposed boundary conditions. The first of these is an integral over that portion of the boundary where the heat flux q' has been specified; the second term is an integral along the boundary of the region R where the convective heat transfer from the boundary occurs, as shown in Fig. 7.1. Minimisation of the functional $\Im$ will yield the equations governing the temperature

distribution.

The three noded, first order, triangular element has been used extensively for the solution of two dimensional heat conduction problems. Within each element the temperature is assumed to vary linearly and can be expressed as,

$$\theta(x,y) = e_1 + e_2 x + e_3 y \tag{7.6}$$

Eq. (7.6) can be expressed in terms of the nodal coordinates and potentials, as demonstrated in appendix E , to give

$$\theta(x,y) = [N][\theta] \tag{7.7}$$

where

$$N = \begin{vmatrix} N_i(x,y) \\ N_j(x,y) \\ N_k(x,y) \end{vmatrix} = \begin{vmatrix} (a_i + xb_i + yc_i)/2A \\ (a_j + xb_j + yc_j)/2A \\ (a_k + xb_k + yc_k)/2A \end{vmatrix}$$

In order to permit analysis by finite element two further assumptions are made,

- The thermal conductivity is constant over a linear element.
- The loss density, if present, is also constant within an element.

The solution for the temperature distribution is obtained by minimising the functional given by Eq. (7.5), with respect to the variational parameters $\theta_p, p = i,j,k$ for each element, which yields

$$\frac{d\Im}{d\theta} = [G][\theta] - [Q] = 0 \tag{7.8}$$

where [G] and [Q] are the admittance matrix and loss vector respectively (appendix E) given by,

$$[G] = \int\int_R [B]^T[D][B]dxdy + \int_{S_3} h[N]^T[N]dS_3 \tag{7.9}$$

$$[Q] = \int\int_R q[N]^T dxdy - \int_{S_2} q'[N]dS_2 + \int_{S3} h[N]^T\theta_\infty dS_3 \tag{7.10}$$

where

$$[B] = \begin{vmatrix} \frac{\partial N_i}{\partial x} & \frac{\partial N_j}{\partial x} & \frac{\partial N_k}{\partial x} \\ \frac{\partial N_i}{\partial y} & \frac{\partial N_j}{\partial y} & \frac{\partial N_k}{\partial y} \end{vmatrix}$$

$$D = \begin{vmatrix} k_x & 0 \\ 0 & k_y \end{vmatrix}$$

For all the elements in the domain, Eq. (7.8) is summed over all the finite elements to give

$$\sum_1^m \frac{d\Im}{d\theta} = 0 \tag{7.11}$$

where m is the number of finite elements which give rise the general matrix equation

$$[G][\theta] = [Q] \tag{7.12}$$

The analysis, hence, reduces to one of solving an $n \times n$ matrix equation, where n is the number of nodes in the region. In order to obtain a unique solution Dirichlet boundary conditions are specified, and imposed in Eq. 7.12. The coefficient matrix [G] is usually large and sparse since non-zero coefficients will exist only when nodes

are coupled by finite element mesh. The sparsity of the matrix [G] can be exploited by using one of the sparse algorithms described by Low [90].

The finite element method has been applied to model the thermal behaviour of the 3 phase induction motor to verify the results given in chapters 4,5,and 6.

For the computation of the temperature rise the following assumptions are made,

- Temperature distribution is assumed to be periodic about a pole pitch (90^0).
- Effect of rotor motion is negligible, i.e. what ever the relative position of the rotor with respect to stator both the temperature and thermal load distribution is identical. Hence the rotor model may be considered as static.
- The losses are distributed according to the measurements obtained in chapter 4.
- A two dimensional finite element model is used so axial heat flow is not taken into consideration. On this basis, therefore that the losses generated in the end winding and end rings flow entirely to the end cap air. Consequently all losses generated within the motor flow radially to the surrounding air.

As a result of applying the above assumptions regarding the end rings, the rotor copper loss is divided between the embedded bars and the rings according to Alger [50]. The ratio of the end ring loss to bar loss is equal to the ratio of the squares of their current densities multiplied by the ratio of the two end ring volume to the volume of all the bars. That is,

$$\frac{R_E}{R_B} = \frac{C_2 D_R}{2\pi C_E L_B P^2} \tag{7.13}$$

where

R_E : the end rings resistance,

R_B : the bars resistance,

D_R : diameter of the end ring,

C_2 : total cross section of all bars

L_B : length of each bar,

C_E : cross section of one end ring,

P : number of pair poles.

7.3 Results and discussion

Fig. 7.2 shows one pole pitch of the machine. This has been selected on the basis of geometrical and thermal symmetry. Boundary conditions applicable to this thermal problem, are also shown in Fig. 7.2 , i.e. AB periodic to AC and BC specified temperature (Dirichlet).

Fig. 7.3 shows the discretised finite element domain created using MESHGEN. Following the field solution using the THERMAL, equi-thermal contours are obtained and typical distributions are shown in Fig. 7.4.

Table 7.1 shows a comparison between experimental results and those calculated using the lumped parameter network and finite element analysis.

The highest discrepancy between measurements and finite element analysis occurs in the embedded winding which is about $25°C$ followed by the air gap, about $20°C$ with all other temperature differences less than 10%. The measured results are higher

Component	Temperatures (^0c)		
Method	Measured	Lumped model	Finite element
Frame	61.4	66.62	63.0
Stator iron	72.2	69.53	66.3
Stator teeth	77.0	75.05	70.2
Embedded winding	102.1	94.33	77.2
End winding	110.0	109.15	-
Air gap	135.0	124.69	116.0
Rotor winding	-	151.11	156.0
rotor iron	128.8	150.40	156.0
Shaft	110.2	112.27	-
Endcap air	71.7	83.89	-

Table 7.1: The comparison of the temperatures for different methods in use

compared to those obtained using finite element method, and the likely reason is the drastic assumptions for the end regions in finite element model. In the lumped model, however, axial heat flow was modelled and this accounted for the better agreement. Comparisons between the lumped parameter and finite element results show that in all regions the lumped parameter results yielded higher temperatures. Possible reasons for this is the inclusion of contact resistance in the lumped network since this will restrict radial heat flow and, hence increases the temperature.

Moreover, the thermal conductivity in the circumferential direction was taken to be the same as that in the radial direction since the finite element does not allow the specification of anisotropic thermal conductivities. This may be gross assumption since in published literature the circumferential conductivity is only about one fifteenth of the radial component. This results in more heat flow, therefore, lower temperatures.

7.4 Conclusion

Undoubtedly, the finite element method has several advantages and limitations. Like all numerical approximations, the finite element method is based on the concept of discretisation. Some of the most important advantages of the finite element method derive from the techniques of introducing boundary conditions.

Though drastic simplifications, the finite element gave an insight into the temperature distribution for the motor in use. It can be concluded that

- Using 2-D finite element is not practical since it does not account for axial heat flow as evident by the large discrepancy between results.
- Contact resistance cannot also be specified in the finite element model to accurately model the system.
- Using anisotropic thermal conductivities will give better results.
- Using 3-D finite element and inclusion of the above recommendations will yield more accurate results.

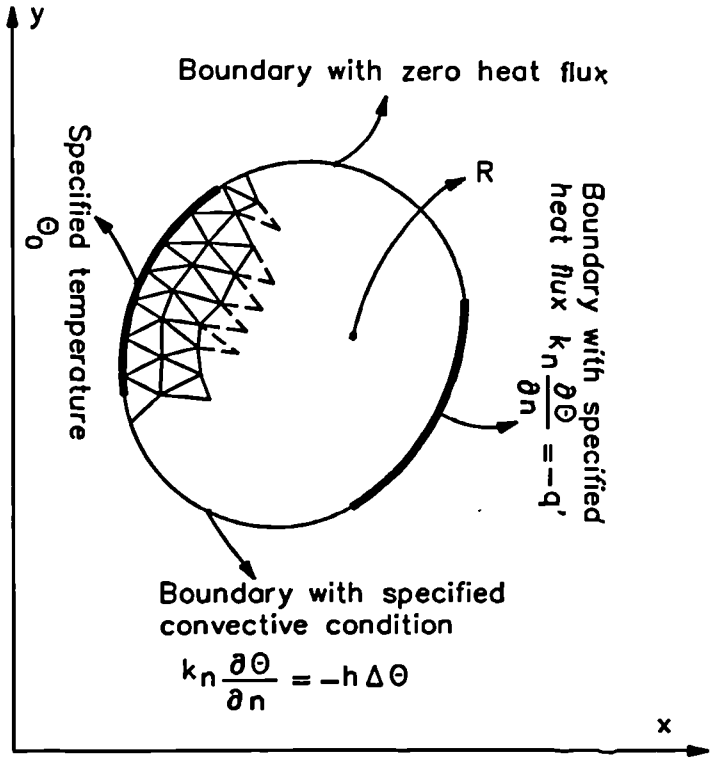

Fig. 7.1 A generalised two dimensional domain showing the discretisation and boundary conditions.

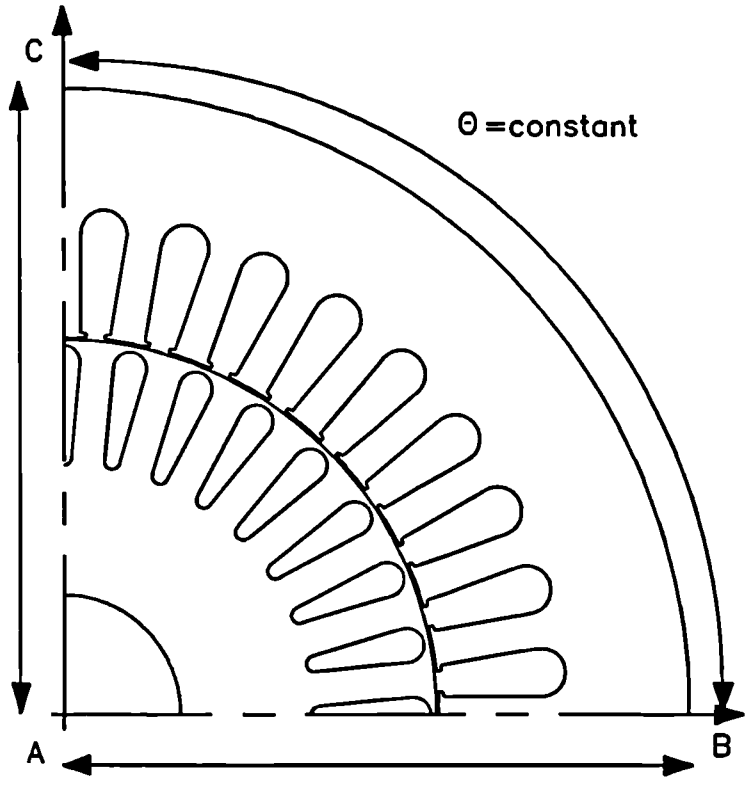

Fig. 7.2 Section of an induction motor used in the finite element analysis.

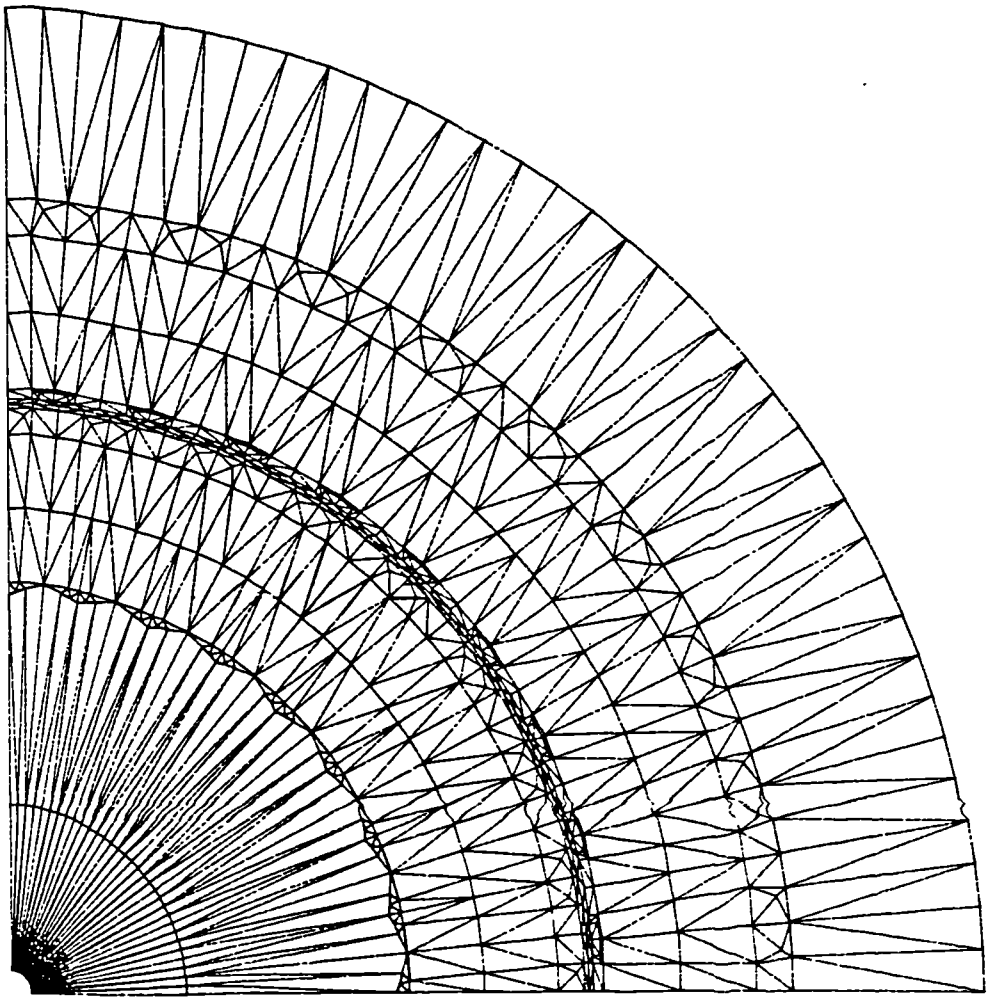

Fig. 7.3 Two dimensional finite element mesh.

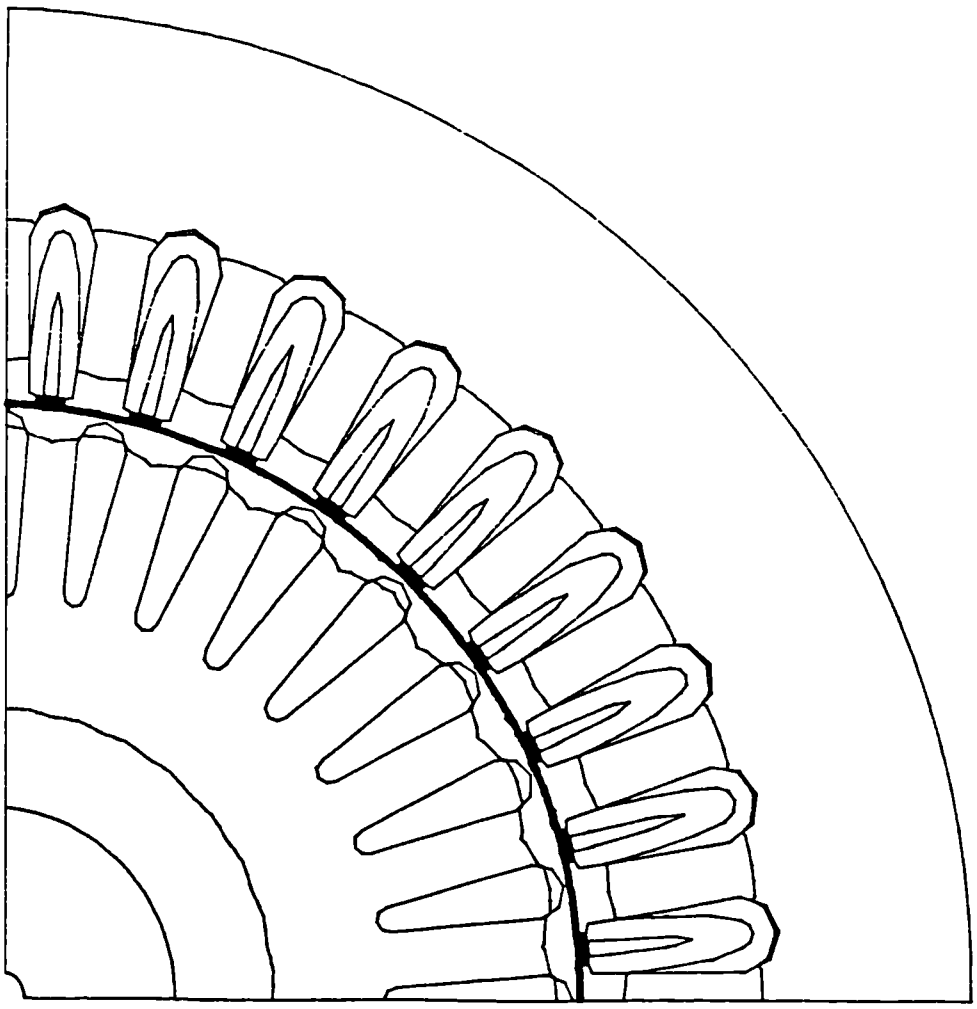

Fig. 7.4 Equi-thermal contours distribution.

Chapter 8

Conclusions

Major improvements have taken place in all aspects of motor design through work centred on maximising the motor output for a given amount of active material subjected to the limiting factors of temperature. The advent of new materials, optimum design strategies, and competitive economics has encouraged the design of small motors with performance temperatures approaching the limits even more closely. Consequently, there is an ever increasing demand for a more precise model for determining the temperature rise in a machine.

The temperature time technique enables more detailed information about iron loss distribution to be obtained which, when coupled with tomographic loss density maps [62], allows easy visualisation and facilitates the explanation of the physical phenomena occurring within the motor.

The ability to predict the temperature rise relies on a complete knowledge of the dimensions of the machine, thermal properties of materials and losses which are generated. Whilst most parameters can be determined quite satisfactory from de-

sign data and tests, the distribution of the iron losses is particularly difficult to ascertain. A comprehensive investigation has been undertaken for determining loss density distribution in an induction motor using a temperature time technique. The temperature time method was applied to a heavily instrumented three phase, 415V, 4kW, induction motor in an attempt to determine the iron loss distribution to a better accuracy than hitherto possible. Following a series of tests the loss densities at specific locations within the volume of the machine were determined and developed in order to predict the loss density distribution in the machine.

The loss density distribution obtained for different sections of the stator showed that the losses in the teeth were higher compared to those occurring in the back iron. This was as expected since flux density levels in the teeth are usually much higher than the back iron. The work shows that an improved distribution of losses would be on the basis of 70% in the stator back iron, and 30% in the stator teeth and not the assumption of 50% to the stator teeth and the remaining 50% to rotor teeth used by other authors. Based on the measurements it was also found that these losses tended to increase slightly at both ends of the motor under load conditions, possibly due to stray load losses.

The provision of volumetric loss density distribution data allows the nature of some components, such as skew and end leakage losses, to be investigated in greater detail. This information will also provide more accurate data for future designs, as well as the corroboration, or otherwise, of previous published works on the subject.

Of special importance in the loss density measurements is the difference obtained between the no load and full load losses which are defined as stray load losses. This is attributed to the change in load current which in turn modifies the flux distributions and, hence, eddy current distribution. Currently there is considerable difficulty

in establishing the magnitude of stray load losses despite the availability of well known experimental methods, because these assume a fundamental incorrect leakage flux distribution under test conditions [12]. Stray load losses for the test motor, determined using the temperature time method were about 27W which represents approximately 0.68% of the rated output of the motor. This figure is in agreement with the British standard [41] value of 0.5% of the rated output power.

One of the main drawbacks associated with the practical implementation of the temperature time method is the inability to record temperature time characteristics on the rotor due to erratic data transmission through rubbing contacts on slip rings. Furthermore the number of thermocouples which can be placed on the rotor is also limited by the availability of sufficient precision slip rings in the integrated circuit unit. Despite these difficulties the temperature time method shows great potential as a tool for gaining valuable information on iron loss distribution in machines from which optimum design strategies can be developed.

From the heat transfer point of view, electric machines tend to be somewhat complex, due to their geometric configuration, diverse material properties, distribution of heat sources, and complicated ventilating paths. These give rise to a myriad of problems and the ability to solve these problems therefore has a great impact on the cost, size and, to some extent, on the feasibility of a particular design. These problems have largely been alleviated through the use of the lumped thermal circuit which has proved to be relatively accurate for predicting the temperature distribution in the machine. In applying the lumped parameter thermal model, special attention was focussed on the proportioning of the iron loss since it was found that an incorrect temperature distribution is obtained if the iron losses are not divided correctly to the teeth and back iron.

As well as predicting the temperature distribution in the motor the model also provides an interesting insight into the thermal behaviour of the machine by evaluating the sensitivity of temperature in the different components to variations in material conductivities, convective heat transfer coefficients, and losses. It was found that the overall temperature distribution is relatively insensitive to the variations of most of the parameters. However, localised temperature distributions are affected by changes in the parameters of component and adjacent components. For example, the temperature of the copper winding is most sensitive to the conductivity of the insulation and to the frame/ambient convective heat transfer coefficient, whilst the variation of other parameters has little effect on the winding temperature (chapter 5). This is an unfortunate situation since insulation properties and convective heat transfer coefficients are the least reliable and most difficult to determine.

Consequently, one of the primary problems associated with the prediction of the temperature distribution is that of using correct thermal parameters associated with the materials as well as modes of heat transfer. A novel technique for determining heat transfer coefficients, using the lumped equivalent thermal circuit was developed to determine the thermal coefficients of composite regions such as bundle conductors/slot lining and also to verify manufacturer's data. This method relies on the accurate measurement of both the temperature and the loss density distribution within the machine.

In general the thermal coefficients obtained for the lumped components are in good agreement with the results of Roberts [33]. But, in the region where the rotor temperature has to be coupled to the network coefficients were not likely to be reliable due to the poor signals from the thermocouples embedded in the rotor. However, this is unlikely to affect the computation of the thermal coefficients for the components remote from the rotor since it has been shown that, via, sensitivity

analysis, that the level of interaction is low. Overall, the results show that by using the equivalent thermal circuit it is possible to predict the global thermal coefficients of the motor to a sufficient accuracy. This method, thus, represents a new technique which may be further developed to provide accurate thermal coefficients for complicated combinations of materials and geometries.

The validity of the lumped parameter thermal network was checked against the finite element method. Undoubtedly, the finite element method has reached a high level of development as a solution technique and provides highly accurate results. However, the finite element method yields accurate results only if the thermal coefficients and loss distribution are available to the required accuracy.

In this research only a 2-dimensional finite element formulation was used which assumed that axial heat flow was negligible. Clearly, this was not the case and consequently a detailed comparison between lumped and finite element method cannot be made. For this to be possible a full 3-dimensional model must be used but this was not attempted due to the lack of time. Nevertheless, the finite element results showed good agreement with those of lumped parameter in regions where heat flow was predominantly radial, e.g. stator teeth, back iron and rotor. This was due to the fact that the laminations acted as heat barriers thereby constraining heat flow to be radial. The discrepancies were largest in the conductors because heat is now able to flow axially in copper. Hence the lumped parameter results can be assumed to be correct with high degree of confidence.

8.1 Further work

More extensive experimental work is required to obtain accurate information from the machine. For a complete study the use of improved instrumentation in the data capture stage is an obvious necessity as is reliable instrumentation of the rotor.

Current measurement of stray load losses is complicated, costly, and not accurate [12]. The test rig and software developed for this project may be extended to investigate stray load losses. Further development of the method would enable stray load losses to be segregated into individual components in order to understand the nature and magnitude so that steps may be taken in the design stage to minimise these losses.

Certain modelling issues still need to be investigated for example the bearings, fan, etc. Although the thermal model is satisfactory, the thermal resistance of the bearings, conduction of heat to the ambient through the shaft and mountings, and the magnitude and distribution of rate of flow of coolant still require detailed attention.

Extensive experimental work is required to determine whether or not the method used to determine thermal coefficients is effective by applying the method to a wider range of motors for example brushless d.c. motors, or synchronous machines.

Appendix A

Performance calculations

The induction machine under, steady state conditions, can be represented by an equivalent network of various resistances and inductances (i.e. magnetising and leakage) which are independent of current, frequency and saturation conditions.

Fig. A.1 shows one phase of a motor where R_1 and R_2 represent the resistances, X_1 and X_2 the leakage reactances of the stator and rotor windings, X_m the magnetising reactance and R_m the resistance representing the iron core losses. In order to predict the performance characteristics of the machine a number of accurate tests are required to determine the equivalent circuit parameters. The IEEE Std. 112 Test Code for Induction Motors and Generators [42] gives authoritative procedures for conducting all the usual tests, i.e. the no load and locked rotor tests from which the circuit parameters may be determined.

A.1 Determination of the circuit parameters

A.1.1 Measurement technique

Due to the accuracy needed throughout this investigation the choice of most suitable and appropriate instrumentation is critical. R.m.s voltages and currents were measured by a PM 2521 automatic multimeter manufactured by Philips with an error of ±1.5%. To account for discrepancies due to possible system unbalance the current was measured in each phase and the average calculated. Input power was measured using two wattmeters each with a maximum error of ±1.5%. Speed measurement was achieved using a compact optical tachometer. The speed measurement is given in revolutions per minute with an error of ± one digit, i.e. at 1000 rpm the error is 0.1% and decreases with increasing speed. Finally, the winding temperature is measured using a thermocouple, which was placed on the stator just at the entrance of the winding during the assembly of the motor.

The relevant manufacturer's data for the test motor is summarized in Table A.1 and the experimental set up is shown in Fig. A.2.

An improved method of parameter evaluation is found in form F1 of the recently revised American standard test code for polyphase induction motors and generators [42] which also details how each test must be performed to achieve accurate results.

Frame size	DM112
Rated Output Power (kW)	4
Rated Line Voltage (V)	415
Rated Line Current (A)	8.4
Number of Poles	4
Number of Stator Slots	36
Number of Rotor Slots	32
Number of Stator Coils/slot	54
Rotor Bar Skew	1.25
Stator winding Connection	Δ
Insulation Class	F

Table A.1: Summary of test motor details

A.1.2 D.C. test for stator resistance

At 25^0c the stator phase resistance was measured using a high accuracy Wheatstone bridge and the resistance value was found to be 4.965 Ω.

A.1.3 No load test

The no load test of induction motor is used to determine the rotational losses of the motor and provides information about its magnetization current. The no load test is carried out by running the uncoupled motor at rated voltage and frequency until thermal equilibrium is reached. At this stage the readings of input power give the total losses within the machine. If no load stray losses are assumed to be part of the core losses and the losses induced in the rotor are neglected (i.e. s=0), then the subtraction of the stator copper losses at test temperature from the total no load losses gives the sum of windage and friction, and core losses. Segregation of the core losses from the friction and windage is achieved by performing a series of no

load tests by varying the applied voltage from 125% of rated voltage down to about 25%. A curve of iron losses and mechanical losses versus voltage is plotted and the extrapolation of curve to intercept the power axis gives a value for the friction and windage losses. The no load characteristic obtained is shown in Fig. A.3 from which the friction and windage losses of $19.9W$ was obtained.

A.1.4 Locked rotor test

The test is performed with a reduced applied voltage which results in about rated current being circulated in the winding. In wound rotor motors the impedance usually varies with different positions of the rotor relative to the stator whereas squirrel cage is a symmetrical bar winding and no variation occurs. Therefore, the rotor may be blocked in any position in the case of a squirrel cage motor, so that it cannot move. In addition, for safety reasons prior to any locked rotor test the direction of rotation should be established thus blocking the rotor in the appropriate direction. When the current is full load value, the voltage, current, and power flowing into the motor are measured.

Following the tests equations are derived from the equivalent circuit of Fig. A.1 and were solved in accordance with the IEEE standard form F-1 and F-3 as follows,

Unless otherwise noted, all admittances, impedances and voltages are per phase for wye for three phase motors. Power ampers are per complete motor. Subscripts, L and 0 refer to quantities pertaining to impedance test and to no load test or operation respectively.

1) No load: Since $s \rightarrow 0$ $\frac{r_2}{s} + jx_2$ is treated as open circuit.

The reactance volt amperes at no load is:

$$var_0 = 3I_1^2 x_1 + 3I_m^2 x_m \tag{A.1}$$

$$I_m = \frac{V_0}{x_m}\left(\frac{1}{1+\frac{x_1}{x_m}}\right) \tag{A.2}$$

Substituting for I_m in Eq.A.1 yields

$$var_0 = 3I_{10}^2 x_1 + \frac{3V_0^2}{x_m}\left(\frac{1}{1+\frac{x_1}{x_m}}\right)^2 \tag{A.3}$$

$$x_m = \frac{3V_0^2}{var_0 - 3I_{10}^2 x_1}\left(\frac{1}{1+\frac{x_1}{x_m}}\right)^2 \tag{A.4}$$

The losses at no load

$$Q_I = Q_0 - 3I_{10}^2 r_1' - Q_{fw} \tag{A.5}$$

$$Q_I = 3I_{h0}^2 r_m \tag{A.6}$$

$$I_{h0} = \frac{V_0}{r_m}\left(\frac{1}{1+\frac{x_1}{x_m}}\right) \tag{A.7}$$

therefore

$$Q_I = \frac{3V_0^2}{r_m}\left(\frac{1}{1+\frac{x_1}{x_m}}\right)^2 \tag{A.8}$$

$$r_m = \frac{3V_0^2}{Q_I}\left(\frac{1}{1+\frac{x_1}{x_m}}\right)^2 \tag{A.9}$$

$$g_m = \frac{Q_I}{3V_0^2}\left(1+\frac{x_1}{x_m}\right)^2 \tag{A.10}$$

Equations (A.9) and (A.10) are the equivalent of (7) and (8) of the IEEE Std.112, form F-1.

2) Locked rotor: At short circuit test $s = 1$ and therefore $x_2 >> r_2$

The volt ampere reactance at locked rotor with r_2 negligible is:

$$var_L = 3I_{1L}^2\left(x_{1L} + \frac{x_{2L}x_{mL}}{x_{2L}+x_{mL}}\right) \tag{A.11}$$

$$var_L(x_{1L})(x_{2L} + x_{mL}) = 3I_{1L}^2(x_{1L})(x_{1L}x_{2L} + x_{1L}x_{mL} + x_{2L}x_{mL}) \quad \text{(A.12)}$$

$$x_{1L} = \frac{var_L}{3I_{1L}^2\left(1 + \frac{x_1}{x_2} + \frac{x_1}{x_m}\right)}\left(\frac{x_1}{x_2} + \frac{x_1}{x_m}\right) \quad \text{(A.13)}$$

$$x_1 = \frac{f}{f_L}x_{1L} \quad \text{(A.14)}$$

Equations (A.4), (A.13) and (A.14) are the same as (1), (2) and (3) of the IEEE Std.112, form F-1, and are solved as follows,

1. Solve (A.4) for x_m, assuming a value of x_1 and $\frac{x_1}{x_2}$,
2. Solve (A.13) for x_{1L}, using the value of $\frac{x_1}{x_m}$ from step 1 and the design ratio of $\frac{x_1}{x_2}$,
3. Solve (A.14) for x_1,
4. Solve (A.4) for x_m, using x_1 from step 3 and the ratio of $\frac{x_1}{x_m}$ from steps 1 and 3,
5. Continue iteration until converged values are obtained to within 1%.

Then

$$x_2 = \frac{x_1}{\left(\frac{x_1}{x_2}\right)} \quad \text{(A.15)}$$

Losses at locked rotor,

$$Q_L = 3I_{1L}^2 r_1'' + 3I_{2L}^2 r_2'' + 3I_{hL}^2 r_m \quad \text{(A.16)}$$

$$I_{hL}r_m = I_{2L}x_{2L} \quad \text{(A.17)}$$

$$I_{hL}^2 r_m = I_{2L}^2 x_{2L}\frac{I_{hL}}{I_{2L}} = I_{2L}^2\frac{x_{2L}^2}{r_m} \quad \text{(A.18)}$$

$$I_{2L} = I_{1L}\left(\frac{1}{1 + \frac{x_2}{x_m}}\right) \quad \text{(A.19)}$$

Therefore

$$Q_L = 3I_{1L}^2 \left[r_1'' + \left(\frac{1}{1+\frac{x_2}{x_m}} \right)^2 r_2'' + \left(\frac{1}{1+\frac{x_2}{x_m}} \right)^2 \frac{x_{2l}^2}{r_m} \right] \tag{A.20}$$

$$r_2'' = \left(\frac{Q_L}{3I_{1L}^2} - r_1'' \right) \left(1 + \frac{x_1 x_2}{x_1 x_m} \right)^2 - \left(\frac{x_2}{x_1} \right)^2 \frac{x_{1L}^2}{r_m} \tag{A.21}$$

With the substitution of g_m for $\frac{1}{r_m}$, Eq.(A.21) is the same as (9) of the IEEE Std.112, from F-1. with,

r_1' stator resistance at temperature during no load test.

r_1'' stator resistance at temperature during short circuit test.

r_2'' rotor resistance referred to stator at temperature during short circuit test.

Accurate prediction of machine characteristics by the equivalent circuit depend upon the closeness by which R_2 represent the actual rotor resistance. The motor parameters are not linear, but are current, frequency and temperature dependent. Accordingly, proper care and adequate knowledge of motor design is often necessary to obtain accurate results. Since there is no single method that is applicable or right for all situations, the IEEE Std 112 [42] includes alternative methods for determining the motor parameters.

In normal operation, the stator frequency is the line frequency of the power system (50 Hz). At starting conditions, the rotor currents are also at line frequency. However, under normal operating conditions, the slip of the motor is only 2 to 4 per cent and therefore the resulting rotor frequency is in the range of 1 to 2 Hz. This creates a problem in that the line frequency does not present the normal operating conditions of the rotor. Depending upon the rotor winding structure, in particular the depth of the conductors, the rotor parameters may or may not be frequency dependent. This frequency dependence must be allowed for in translating the locked rotor parameters, at supply frequency, to their equivalents during normal operation where the frequency drops to a very low value (almost 0 Hz). IEEE Std 112 [42]

states that if the locked rotor test is performed at rated frequency then the total reactance should be corrected for frequency based calculations or tests on similar machine and R_2 must be determined by a load point following form F-3 where the equivalent circuit is solved iteratively until a value of R_2/s is found such that the measured input power equals the calculated power. Then, by multiplying R_2/s by the measured slip, the value of R_2 is determined.

Another alternative is the use of the ratio of the 50 Hz to 0 Hz equivalent values which is related to the rotor winding depth, divided by the skin depth of the rotor conductor at 50 Hz according to a theoretical analysis by Swann and Salmon [67]. Having determined the ratio from the manufactures design data and the physical properties of the rotor conductor, the ratio of $R_2(50Hz)/R_2(0Hz)$ can be read directly from Swann's theoretical curve. The correction factor is found to be of the order of 1.2. The validity of the correction process was gained by comparing the locked rotor parameter with that determined from using form F-3, at full load point. Table A.2, shows a good agreement between the two methods.

The results obtained are listed in Tables A.3, A.4 and A.5. A great deal of care was exercised in taking the measurement of these tests and calculation of equivalent circuit parameter values to minimise errors in subsequent prediction and loss calculation procedures.

Method	R_2 (Ω)
Using Swann's curve	$5.48/1.2 = 4.57$
Using Form F-3	4.93

Table A.2: Rotor parameter frequency correction factors

Locked rotor results				No load results				F+W
V (V)	I (A)	W (W)	T_{wndg} (^{0} C)	V (V)	I (I)	W (W)	T_{wndg} (^{0} C)	W_{fw} (W)
95.6	8.45	710	23	415.6	3.98	365	40.3	19.9

Table A.3: Locked rotor and no load test results

Components	Symbols	magnitude
Stator Resistance	R_1 (Ω)	4.984
Rotor Resistance	R_2 (Ω)	3.52
Stator Leakage Reactance	X_1 (Ω)	8.66
Rotor Leakage Reactance	X_2 (Ω)	8.66
Magnetising Reactance	X_m (Ω)	169.52
Core Resistance	R_m (Ω)	1848.08

Table A.4: Equivalent circuit parameters of the motor

Components	Magnitude
Copper losses (W)	708
Iron losses (W)	90.4
Friction and windage losses (W)	19.9
Stray load losses (W)	25
Total losses (W)	843.3

Table A.5: Total losses of the motor at full load

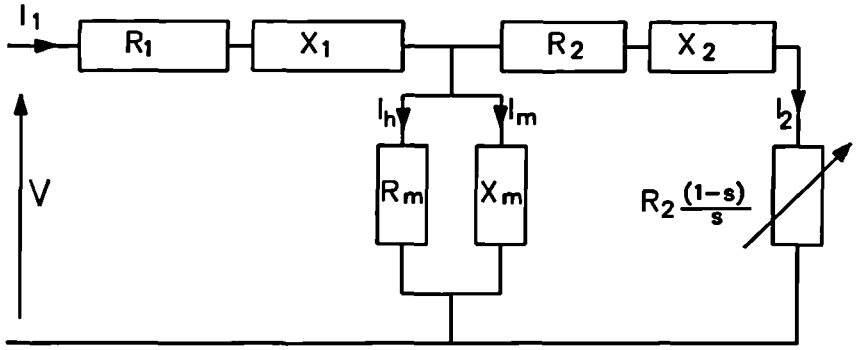

Fig. A.1 Equivalent circuit of an induction motor.

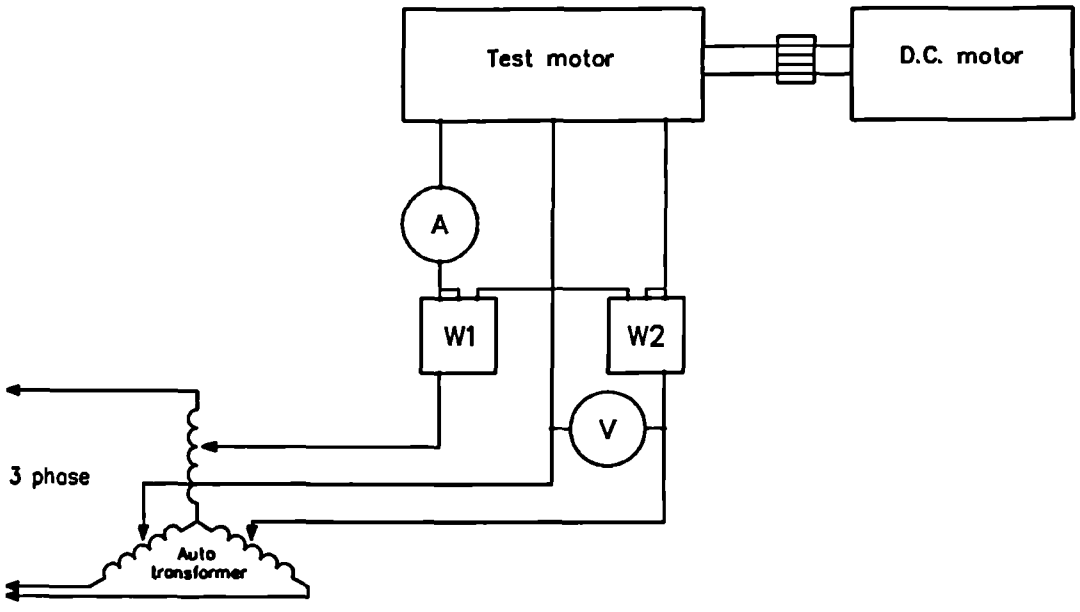

Fig. A.2 Diagram representation of experimental test rig.

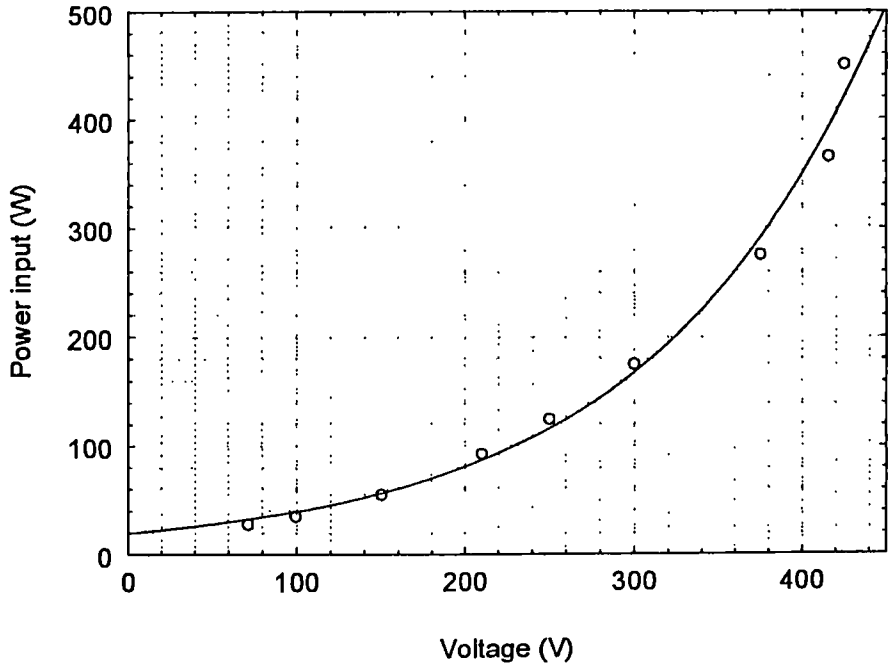

Fig. A.3 No load test characteristic.

Appendix B

Development of the equivalent thermal circuit

B.1 Introduction

For certain geometries an exact temperature distribution may be obtained analytically from the solution of the governing partial differential equation which is of the Poissonian or Laplacian type. An electrical machine, however, is a complex thermal system so that the solution to the differential equation, subject to the boundary conditions, for the whole machine is largely impossible. A more amenable method is to develop an equivalent thermal circuit comprising of thermal resistances, capacitances and heat sources, which can then be solved as an electrical network. Thermal resistances are calculated from the solution of the differential conductance equation for a unidirectional flow of heat in representative ideal elements. The temperature distribution in these elements then serves as the basis for the formulation of resistances.

By definition, the equivalent thermal resistance between two elements, i and j, based on Fourier's law of heat conduction is given by the basic equation

$$R_{ij} = \frac{\theta_i - \theta_j}{Q_{ij}} \tag{B.1}$$

where

θ_i and θ_j are the i^{th} and j^{th} node mean temperatures,

Q_{ij} The heat flow between the i and j nodes,

R_{ij} The thermal resistance.

To illustrate the calculation of thermal resistances, the case of a slab which is insulated on all its surfaces except its two ends is chosen, as shown in Fig. B.1. The thermal resistance is

$$R_0 = \frac{L}{kA} \tag{B.2}$$

where

L: Length of the slab,

A: Cross section,

k: Thermal conductivity,

The total heat generated in the element is given by

$$Q = qAL$$

where

q Internal heat generated per unit volume.

For a one directional heat flow in a medium, three possible cases exist and these will be described in the subsequent section.

B.1.1 Unidirectional heat flow with only external heat input

Laplace's equation applies for this case, shown in Fig. B.1, and general form of the one dimensional equation is

$$k\frac{d^2\theta}{d^2x} = 0 \tag{B.3}$$

Integrating Eq.(B.3) twice yields the general equation,

$$\theta(x) = c_1 x + c_2 \tag{B.4}$$

where the constants c_1 and c_2 can be evaluated by applying the boundary conditions, i.e.

$$Q_{x=0} = -kA(\tfrac{d\theta}{dx})_{x=0} = Q_1,$$
$$\theta_{x=0} = \theta_1,$$
$$\theta_{x=L} = \theta_2$$

where the negative sign indicates that Q_1 is in a direction opposite to the temperature gradient.

The final expression for the temperature distribution is,

$$\theta(x) = \theta_2 + Q_1 R_0 \left(1 - \frac{x}{L}\right) \tag{B.5}$$

According to Eq.(B.5) the temperature variation in a slab for these conditions is linear.

The mean temperature of the slab is the important parameter in the equivalent circuit and is defined by,

$$\theta_{av} = \frac{1}{L}\int_{x=0}^{x=L} \theta(x)dx = \theta_2 + \frac{Q_1 L}{2kA}$$

$$= \theta_2 + Q_1 \frac{R_0}{2} \tag{B.6}$$

The maximum temperature of the slab is given by,

$$\frac{d\theta}{dx} = 0$$

i.e. the location when $Q_1 = 0$ (at $x = 0$).

$$\theta_m = \theta_{x=0} = \theta_2 + Q_1 R_0 \tag{B.7}$$

The location at which the temperature is equal to the mean temperature may be obtained by comparing the Eqs.(B.5) and (B.6)

$$\theta_{av} = \theta_2 + Q_1 \frac{R_0}{2} = \theta_2 + Q_1 R_0 \left(1 - \frac{x_{av}}{L}\right) \tag{B.8}$$

which gives;

$$x_{av} = \frac{L}{2}$$

It can be seen that the thermal resistance of heat from the location of mean temperature to the cooling medium is represented by $\frac{R_0}{2}$ which is clearly the thermal resistance of the slab of an area A and effective length $\frac{L}{2}$.

B.1.2 Unidirectional heat flow with only internal heat generation

For this conditions the one dimensional form of Poisson's equation applies, and given by,

$$\frac{d^2\theta}{dx^2} + \frac{q}{k} = 0 \tag{B.9}$$

Integrating Eq. (B.9) twice and imposing the appropriate boundary conditions, viz

$$Q_{x=0} = -kA(\frac{d\theta}{dx})_{x=0} = 0,$$
$$\theta_{x=L} = \theta_2$$

yields the resulting expression for the temperature distribution in the slab,

$$\begin{aligned} \theta(x) &= \theta_2 + \frac{q}{2k}(L^2 - x^2) \\ &= \theta_2 + \frac{QR_0}{2}\left(1 - (\frac{x}{L})^2\right) \end{aligned} \tag{B.10}$$

The mean temperature is calculated using,

$$\begin{aligned} \theta_{av} &= \frac{1}{L}\int_0^L \theta(x)dx \\ &= \theta_2 + Q\frac{R_0}{3} \end{aligned} \tag{B.11}$$

whilst the maximum temperature at $x = 0$ is given by,

$$\theta_m = \theta_1 = \theta_2 + Q\frac{R_0}{2} \tag{B.12}$$

The location at which the mean temperature occur can be found by comparing Eqs.(B.11) and (B.10) to give,

$$x_{av} = \frac{L}{\sqrt{3}}$$

A thermal network which represents heat flow in the slab for the condition of internal heat generation is shown in Fig. B.2.

B.1.3 Unidirectional heat flow with external heat input and internal heat generation

It can be deduced from the above limiting examples that, the effective thermal resistance for the general case, must be somewhere between these values i.e. between $\frac{R_0}{2}$ and $\frac{R_0}{3}$.. This can be shown by solving Eq. (B.9) subjected to the boundary conditions,

$$Q_{x=0} = -kA(\tfrac{d\theta}{dx})_{x=0} = Q_1,$$
$$\theta_{x=L} = \theta_2$$

The temperature distribution in the slab is of the form,

$$\begin{aligned}\theta(x) &= \theta_2 + \frac{q}{2k}(L^2 - x^2) + \frac{Q_1}{kA}(L - x) \\ &= \theta_2 + Q\frac{R_0}{2}\left(1 - (\frac{x}{L})^2\right) + Q_1 R_0(1 - \frac{x}{L}) \end{aligned} \tag{B.13}$$

The maximum temperature at $x = 0$ is given by,

$$\theta_1 = \theta_2 + \frac{R_0}{2}Q + R_0 Q_1 \tag{B.14}$$

The mean temperature is,

$$\theta_{av} = \theta_2 + \frac{R_0}{3}Q + \frac{R_0}{2}Q_1 \tag{B.15}$$

and the maximum temperature is,

$$\theta_m = \theta_1 = \theta_2 + \frac{R_0}{2}Q + R_0 Q_1 \tag{B.16}$$

The position of the point of the mean temperature of the slab is given by equating Eqs.(B.15) and (B.13),

$$x_{av} = \left(-D + \sqrt{D^2 + D + \frac{1}{3}}\right) L \tag{B.17}$$

where

$$D = \tfrac{Q_1}{Q} \text{ and } \tfrac{1}{2} \leq x_{av} \leq \sqrt{\tfrac{1}{3}}$$

Let the ratio $E = \frac{Q_1}{Q_1+Q}$

$$\Rightarrow \theta_{av} = \theta_2 + (Q_1 + Q)R_0\left(\frac{E+2}{6}\right)$$

The effective thermal resistance is,

$$R = \frac{E+2}{6} R_0 \tag{B.18}$$

In electrical machines E is usually not known, and will vary between zero (0) and one (1). However this ratio can be adequately approximated in most cases, and if necessary the resistance may be corrected following the initial solution of the equations.

It can be seen that the direct application of Eqs. (B.14) and (B.15) results in non-symmetrical network. To develop a symmetrical network, therefore, the circuit for Fig. B.3 is utilised where the temperature can be expressed as

$$\begin{aligned} \theta_1 &= \theta_2 + \frac{R_0}{2}[Q_1 + Q(1-\alpha)] + \frac{R_0}{2}(Q_1 + \alpha Q) \\ &= \theta_2 + R_0 Q_1 + \frac{R_0}{2} Q \end{aligned} \tag{B.19}$$

and the mean temperature as,

$$\theta_{av} = \theta_2 + \frac{R_0}{2}[Q_1 + Q(1-\alpha)] \tag{B.20}$$

Where $\alpha = \frac{1}{3}$ is the ratio of the losses situated in node 1 or 2 to the total losses in the slab, Q, in order for Eq. (B.20) to be consistent with Eq. (B.15)

The parameter α of this equivalent thermal circuit do not depend on the value of Q_1, and it may therefore be applied to case of section (B.1.1) since at $Q = 0$ it is identical to the case from section B.1.1. This scheme is therefore applicable for all three cases of heat flow and for both flow directions.

Any value of ,α, may be used to give a representation of the average temperature. For example If $\alpha = 0$ then to ensure a symmetric equivalent circuit it is necessary to add an additional resistance R_m, as shown in Fig. B.4. The mean temperature of the body is now not assigned to node 3 but rather to node 4 at which all losses

generated in the body are situated. The mean temperature of node 4 from the equivalent thermal circuit Fig. B.4 is equal to,

$$\theta_{av} = \theta_2 + Q_1 \frac{R_0}{2} + Q\left(R_m + \frac{R_0}{2}\right) \tag{B.21}$$

Comparing Eqs. (B.21) and (B.15) results,

$$R_m = -\frac{R_0}{6} \tag{B.22}$$

In the case $Q = 0$, there is no fall in temperature at resistance R_m and the two nodes 3 and 4 have identical temperatures and the equivalent thermal network from Fig. B.4 is transformed into the form shown in Fig. B.5. The equivalent thermal circuits Figs. B.3 and B.4 are equivalent to each other but the equivalent thermal network, Fig. B.4, is more convenient to use, since it contains only one node. In the case where the mean temperature of the body is not of interest, the equivalent thermal network shown in Fig.B.5 may be used. The mean temperature may be calculated from the simple relationship,

$$\theta_{av} = \theta_3 + R_m Q$$

B.2 Case of cylinder

B.2.1 Radial heat flow in a hollow cylinder

Fig. 4.6 shows a section of hollow cylinder of length H with constant thermal conductivities, k_r and k_a in the radial and axial directions respectively, and internal heat generation q per unit volume.

The total heat generated in the element is given by,

$$Q = \pi q H(r_2^2 - r_1^2) \tag{B.23}$$

from which expressions for the thermal resistances in the radial direction can be derived by solving the differential equations for two specific cases, viz with and without internal heat generation.

B.2.1.1 No internal heat generation

Steady state heat conduction through a cylindrical wall in the radial direction is governed by the cylindrical form of Laplace's equation, i.e.

$$\frac{d^2\theta}{dr^2} + \frac{1}{r}\frac{d\theta}{dr} = 0 \tag{B.24}$$

subjected to the boundary conditions

$$Q_{r=r_1} = Q_1 = -k_r A_1 \tfrac{d\theta}{dr},$$
$$\theta_{r_2} = \theta_2 \quad .$$

where $A_1 = 2\pi r_1 H$ is the internal surface of the cylinder.

The general solution of Eq.(B.24) is in the form,

$$\theta(r) = c_1 \ln r + c_2 \tag{B.25}$$

where the constant can be determined by introducing the boundary conditions to give

$$c_1 = -\frac{Q_1 r_1}{k_r A_1} \tag{B.26}$$

$$c_2 = \theta_2 + \frac{Q_1 r_1}{k_r A_1} \ln r_2 \tag{B.27}$$

The temperature distribution in the radial direction can be expressed as,

$$\theta(r) = \theta_2 - \frac{Q_1 r_1}{k_r A_1} \ln \frac{r}{r_2} \tag{B.28}$$

from which temperature θ_1 on the inside of the cylinder is given by,

$$\theta_1 = \theta_2 - \frac{Q_1 r_1}{k_r A_1} \ln \frac{r_1}{r_2} \tag{B.29}$$

Thus the mean temperature of the cylinder can be calculated using

$$\theta_{av} = \frac{1}{V} \int_0^V \theta(r) dV \tag{B.30}$$

at a distance r the volume of the cylinder can be expressed as $V = \pi(r^2 - r_1^2)H$ from which one can derive the expression of $dV = 2\pi r H dr$ then Eq. (B.30) becomes,

$$\begin{aligned} \theta_{av} &= \frac{2}{r_2^2 - r_1^2} \int_{r_1}^{r_2} (c_1 \ln r + c_2) r dr \\ &= \frac{2}{r_2^2 - r_1^2} \left(c_1 \left[\frac{r^2 \ln r}{2} \right]_{r_1}^{r_2} - c_1 \int_{r_1}^{r_2} \frac{r}{2} dr + c_2 \int_{r_1}^{r_2} r dr \right) \\ &= \frac{c_1}{r_2^2 - r_1^2} (r_2^2 \ln r_2 - r_1^2 \ln r_1) - \frac{c_1}{2} + c_2 \end{aligned} \tag{B.31}$$

Substituting for c_1 and c_2 from Eqs. (B.26) and (B.27) yields,

$$\theta_{av} = \theta_2 + \frac{Q_1 r_1}{2 k_r A_1} (1 - 2B) \tag{B.32}$$

where

$$B = \frac{r_1^2}{r_2^2 - r_1^2} \ln \frac{r_2}{r_1}$$

The mean temperature of the cylinder is situated on the radius,

$$r_{av} = r_2 \exp -\frac{1}{2} \left(1 - \frac{r_1^2}{r_2^2 - r_1^2} \ln \frac{r_2}{r_1} \right) \tag{B.33}$$

The position of the mean radius is dependent on the ratio of $\frac{r_1}{r_2}$ and varies within the limits given by,

$r_{av} = r_1 + 0.5(r_2 - r_1)$ when $\quad \frac{r_1}{r_2} \to 1$

$r_{av} = r_1 + (r_2 - r_1)\exp(-\frac{1}{2}) = r_1 + 0.6065(r_2 - r_1)$ when $\quad \frac{r_1}{r_2} \to 0$

For $\frac{r_1}{r_2} \rightarrow 0$ the form of the cylinder becomes similar to that of the slab.

The thermal resistances can now be determined by dividing the temperature difference by the heat flow through it, i.e.

$$\begin{aligned} R_1 &= \frac{\theta_1 - \theta_{av}}{Q_1} \\ &= \frac{1}{4\pi k_r H}[2\ln(r_2/r_1) - (1-2B)] \end{aligned} \tag{B.34}$$

Substituting for B in Eq. (B.34) can be reduced to,

$$R_1 = \frac{1}{4\pi k_r H}\left(\frac{2r_2^2 \ln(r_2/r_1)}{r_2^2 - r_1^2} - 1\right) \tag{B.35}$$

In a similar manner the thermal resistance R_2 is obtained and is given by,

$$R_2 = \frac{1}{4\pi k_r H}\left(1 - \frac{2r_1^2 \ln(r_2/r_1)}{r_2^2 - r_1^2}\right) \tag{B.36}$$

R_1 applies to the inner part of the cylinder whilst R_2 applies to the outer part, as shown in Fig. 4.8.

B.2.1.2 With internal heat generation

For radial heat flow in cylinder with internal heat generation, Poisson's equation applies and is given by:

$$\frac{d^2\theta}{dr^2} + \frac{1}{r}\frac{d\theta}{dr} + \frac{q}{k_r} = 0 \tag{B.37}$$

subjected to the boundary conditions

$$\left(\frac{d\theta}{dr}\right)_{r=r_1} = -\frac{Q_1}{k_r A_1},$$

$$\theta_{r=r_2} = \theta_2$$

The solution of Eq. (B.37) is of the form:

$$\theta(r) = -\frac{q}{4k_r}r^2 + c_3 \ln r + c_4 \tag{B.38}$$

and if the boundary conditions are applied the temperature distribution is of the form,

$$\begin{aligned}\theta(r) &= \theta_2 + \frac{Q}{2\pi k_r H(r_2^2 - r_1^2)}\left[\frac{r_2^2 - r^2}{2} + r_1^2 \ln(r/r_2)\right] \\ &- \frac{Q_1}{2\pi k_r H}\ln(r/r_2)\end{aligned} \tag{B.39}$$

hence the mean temperature of the cylinder can be evaluated to give

$$\begin{aligned}\theta_{av} &= \theta_2 + \frac{Q}{4\pi k_r H(r_2^2 - r_1^2)}\left[\frac{r_2^2 - r_1^2}{2} + r_1^2(1 - 2B)\right] \\ &- \frac{Q_1}{4\pi k_r H}(1 - 2B)\end{aligned} \tag{B.40}$$

The location of the mean radius depends on the ratio of the cylinder radii $\frac{r_1}{r_2}$ and the ratio of losses, $\frac{Q_1}{Q}$, and can be determined by a comparison of temperature at $\theta_{r=r_{av}} = \theta_{av}$.

For example if $Q_1 = 0$ then,

$r_{av1} = r_1 + \frac{1}{\sqrt{2}}(r_2 - r_1)$ when $\frac{r_1}{r_2} \to 0$

$r_{av2} = r_1 + \frac{1}{\sqrt{3}}(r_2 - r_1)$ when $\frac{r_1}{r_2} \to 1$

For $\frac{r_1}{r_2} \to 1$ the form of the cylinder is similar to that of a bar.

The case of $\frac{Q}{Q_1} = 0$ becomes the case considered in the section B.2.1 For the intermediate cases, $0 \leq \frac{Q}{Q_1}$, r_{av} lies between the limits $r_{av1} \leq r_{av} \leq r_{av2}$.

To represent this model a T equivalent circuit, as shown in Fig. 4.9, is used. Here R_1 and R_2 are the same as those developed for the case with no internal heat generation,

and R_m can be calculated using,

$$R_m = \frac{\theta_{av} - \theta_2}{Q} - R_2(\frac{Q_1}{Q} + 1) \tag{B.41}$$

Substituting for θ_{av} and R_2 from Eqs. (B.40) and (B.36) into Eq.(B.41) gives,

$$R_m = \frac{1}{8\pi k_r H(r_2^2 - r_1^2)} \left(r_1^2 + r_2^2 - \frac{4r_1^2 r_2^2 \ln(r_2/r_1)}{r_2^2 - r_1^2} \right) \tag{B.42}$$

B.2.2 Axial heat flow in hollow cylinder

For steady state heat conduction in the axial direction, the governing Poisson's equation is,

$$\frac{d^2\theta}{dx^2} + \frac{q}{k_a} = 0 \tag{B.43}$$

To simplify the analysis, symmetry about the axial centre plane is assumed. This implies that the heat generated within each half of the cylinder is half of the total heat generated, and heat flows in both directions about the plane symmetry is equal and opposite.

Due to the symmetry the following boundary conditions apply

$$Q_{x=0} = kA(\tfrac{d\theta}{dx})_{x=0} = 0$$

$$\theta_{x=h} = \theta_4$$

and the solution of Eq. (B.43) yields,

$$\begin{aligned} \theta(x) &= \theta_4 + \frac{q}{2k}(h^2 - x^2) \\ &= \theta_4 + \frac{Q' R_0'}{2} \left[1 - \left(\frac{x}{h} \right)^2 \right] \end{aligned} \tag{B.44}$$

where $h = \frac{H}{2}$ and $Q' = \pi h(r_2^2 - r_1^2)$

The mean temperature can then be derived using

$$\begin{aligned} \theta_{av} &= \frac{1}{h}\int_0^h \theta(x)dx \\ &= \theta_4 + \frac{Q'R'_0}{3} \end{aligned} \tag{B.45}$$

From which the location of the mean temperature can be determined by comparing Eqs. (B.43) and (B.45) to give,

$$x_{av} = \frac{h}{\sqrt{3}}$$

Fig. 4.7 shows the equivalent circuit for this model where

$$R_1 = \frac{R'_0}{3} = \frac{h}{3\pi k_a(r_2^2 - r_1^2)} \tag{B.46}$$

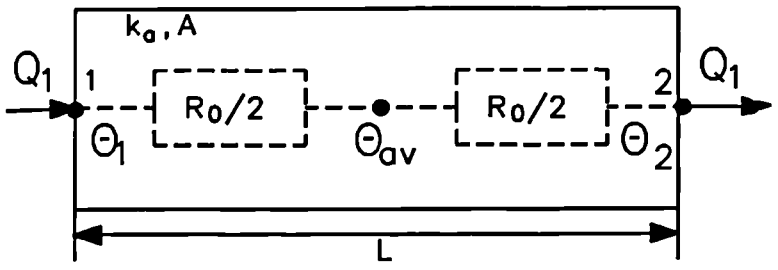

Fig. B.1 Equivalent circuit for a slab (no internal heat generation).

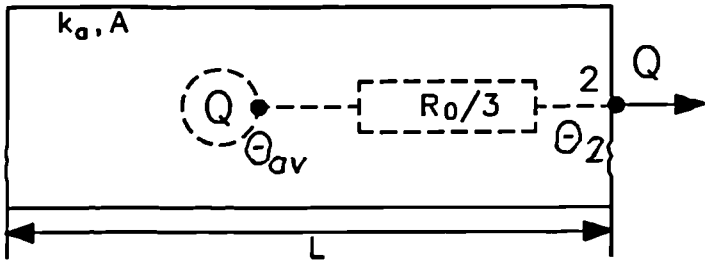

Fig. B.2 Equivalent circuit for a slab (internal heat generation only)

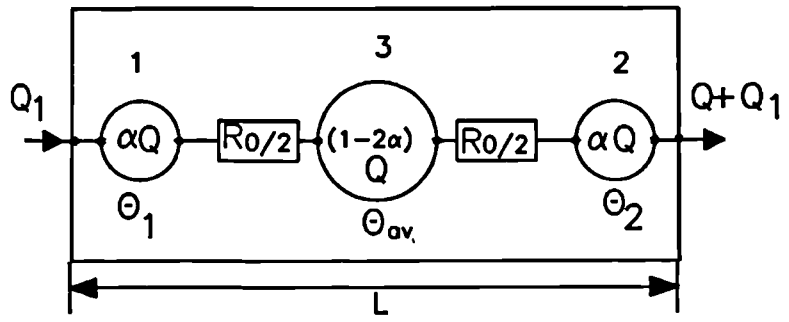

Fig. B.3 Equivalent circuit for a slab (with internal heat generation).

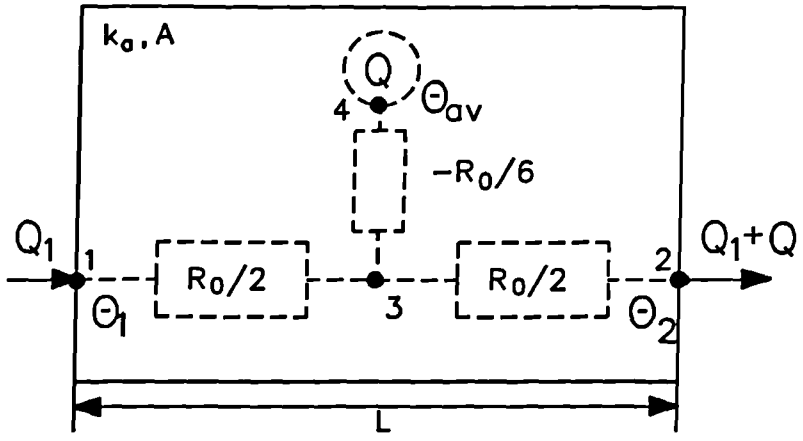

Fig. B.4 'T' Equivalent circuit for a slab (with internal heat generation).

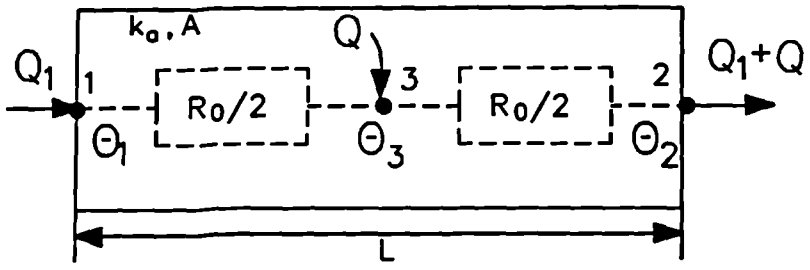

Fig. B.5 Equivalent circuit for a slab (with internal heat generation)

Appendix C

Steady state theory of the equivalent circuit

The behaviour of the induction motor can be investigated by the use of the equivalent electrical circuit provided that proper values are assigned to the parameters to suit the operating conditions.

Referring to Fig. C.1 the total machine losses per phase are given from the equivalent circuit by,

$$Q_{ph} = \frac{V_1^2}{cR_m} + \left(\frac{I_2}{c}\right)^2 cR_{s/c} \tag{C.1}$$

$$R_{s/c} = R_1 + cR_2$$

$$X_{s/c} = X_1 + cX_2$$

$$c \simeq 1 + \frac{X_1}{cX_m}$$

The branch current can be found in terms of the measurable quantities V_1 and I_1 by considering the reactive power in the circuit and the vector diagram relating I_m,

$\frac{I_2}{c}$ and I_1 to the input voltage, shown in Fig. C.2 with the assumption that I_m is strongly reactive which is the case of induction motor ($X_m << R_m$) then,

$$\left(\frac{I_2}{c}\right)^2 = (I_1 \cos\beta)^2 + (I_1 \sin\beta - I_m)^2 \tag{C.2}$$

and furthermore,

$$I_m = \frac{V_1}{cX_m} \tag{C.3}$$

Substituting for I_m in Eq. (C.2) gives,

$$\left(\frac{I_2}{c}\right)^2 = I_1^2 - \frac{2V_1 I_1 \sin\beta}{cX_m} + \frac{V_1^2}{cX_m^2} \tag{C.4}$$

The term, $V_1 I_1 \sin\beta$, is the reactive power per phase which can be expressed from the equivalent circuit as,

$$V_1 I_1 \sin\beta = \frac{V_1^2}{cX_m} + cX_{s/c}\left(\frac{I_2}{c}\right)^2 \tag{C.5}$$

Substituting for this in Eq. (C.4) yields,

$$\left(\frac{I_2}{c}\right)^2 = \frac{X_m}{X_m + 2X_{s/c}} I_1^2 - \frac{1}{c^2 X_m (X_m + 2X_{s/c})} V_1^2 \tag{C.6}$$

Substituting for $\frac{I_2}{c}$ in Eq. (C.1), the total power per phase can be expressed as,

$$Q_{ph} = \frac{V_1^2}{cR_m} - \frac{R_{s/c}}{cX_m(X_m + 2X_{s/c})} V_1^2 + \frac{cR_{s/c}X_m}{X_m + 2X_{s/c}} I_1^2 \tag{C.7}$$

The Total power loss per phase include iron losses, stator copper losses and rotor copper loss. Eq. (C.7) must be split into three components which are,

Stator copper loss is simply given by,

$$Q_{sc} = I_1^2 R_1 \tag{C.8}$$

Rotor copper loss is given by

$$\begin{aligned} Q_{rc} &= \left(\frac{I_2}{c}\right)^2 c^2 R_2 \\ &= -\frac{R_2}{X_m(X_m + 2X_{s/c})} V_1^2 + \frac{c^2 R_2 X_m}{X_m + 2X_{s/c}} I_1^2 \end{aligned} \tag{C.9}$$

Iron loss is given by,

$$\begin{aligned} Q_I &= Q_{ph} - (Q_{sc} + Q_{rc}) \\ &= \frac{V_1^2}{cR_m} - \frac{R_1}{cX_m(X_m + 2X_{s/c})} V_1^2 + \left[\frac{cX_m}{Xm + 2X_{s/c}} - 1 \right] R_1 I_1^2 \end{aligned} \quad \text{(C.10)}$$

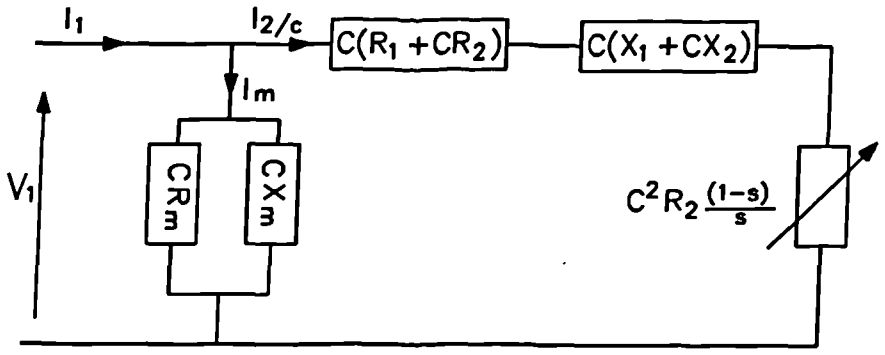

Fig. C.1 Induction motor electrical equivalent circuit.

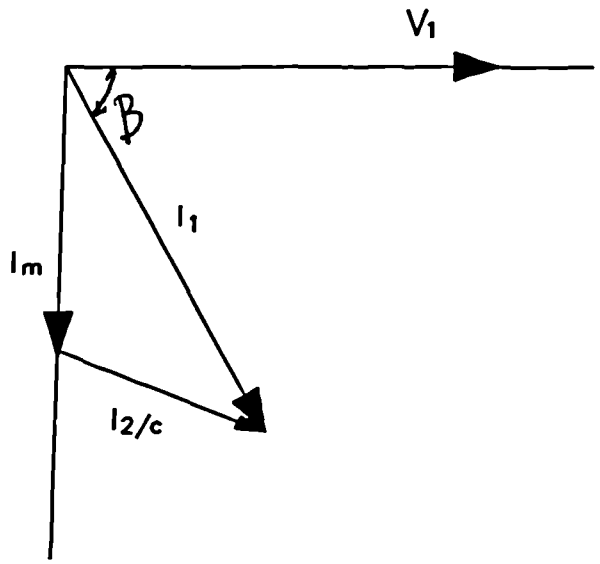

Fig. C.2 Equivalent circuit phasor diagram.

Appendix D

Thermal constants and motor dimensions

Material	Symbol	Magnitude	Unit
Aluminium conductivity	k_a	204	$W/m\ ^0c$
Copper conductivity	k_c	385	$W/m\ ^0c$
Steel conductivity	k_s	41.3	$W/m\ ^0c$
Lamination conductivity (along the lamination)	k_r	45.2	$W/m\ ^0c$
Lamination conductivity (perpendicular to the lamination)	k_a	1.97	$W/m\ ^0c$
Slot liner conductivity	k_i	0.26	$W/m\ ^0c$
Varnish conductivity	k_v	0.4	$W/m\ ^0c$
Aluminium specific heat	c_a	896	$J/K_g\ ^0c$
Copper specific heat	c_c	383	$J/K_g\ ^0c$
Steel specific heat	c_c	502	$J/K_g\ ^0c$
Aluminium density	ρ_a	2707	K_g/m^3
Copper density	ρ_c	8954	K_g/m^3
Steel density	ρ_s	7850	K_g/m^3

Table D.1: Thermal constants

Component	Symbol	Magnitude	Unit
Frame area	A_f	0.1017	m^2
Frame outer radius	fr_2	90.93	mm
Frame inner radius	fr_1	82.93	mm
Stator length	H	130.0	mm
Stator outer radius	sr_2	82.93	mm

Table D.2: Dimensions of the frame

Component	Symbol	Magnitude	Units
Stator axial length	H	130.0	mm
Stator outer radius	sr_2	82.93	mm
Stator inner radius	sr_1	66.168	mm
Stator staking factor	s	0.95	-

Table D.3: Dimensions of the stator back iron

Component	Symbol	Magnitude	Units
Stator teeth length	H	130.0	mm
Equivalent tooth high	t_h	16.168	mm
Stator tooth width	t_{av}	7.29	mm
Stator staking factor	s	0.95	-
Number of teeth	n	36	-

Table D.4: Dimensions of the stator teeth

Component	Symbol	Magnitude	Units
Stator winding axial length	H	130.0	mm
Equivalent copper high	c_h	13.5	mm
Slot copper average width	c_w	6.78	mm
Slot copper+liner insulation average width	c_w	7.034	mm
Equivalent slot copper area	A_c	74.0E-04	m^2
Slot to end winding length ratio	β	0.54	-
Number of slots	n	36	-

Table D.5: Dimensions of the stator slot

Component	Symbol	Magnitude	Units
Axial mean length of the end winding	H_e	130.0	mm
Equivalent copper high	c_{eh}	13.5	mm
Slot copper average width	c_{ew}	6.78	mm
End slot winding length ratio	β_e	0.46	-
Number of slots	n	36	-

Table D.6: Dimensions of the end winding

Component	Symbol	Magnitude	Units
Airgap axial length	H	130.0	mm
Gap outer radius	gr_2	50.0	mm
Gap inner radius	gr_1	49.62	mm
Airgap width	l_g	0.38	mm
Tooth pitch	τ_t	10.0	Degrees
Equivalent tooth arc	τ_c	5	Degrees

Table D.7: Dimensions of the airgap

Component	Symbol	Magnitude	Units
Rotor axial length	H	130.0	mm
Rotor outer radius	rwr_2	49.62	mm
Equivalent rotor winding radius	rwr_1	44.11	mm
Volume of the end ring	V_{er}	49.62	mm^3

Table D.8: Dimensions of the rotor windings

Component	Symbol	Magnitude	Units
rotor axial length	H	130.0	mm
Rotor outer radius	rr_2	41.11	mm
Rotor inner radius	rr_1	15.875	mm
Stator staking factor	s	0.95	-

Table D.9: Dimensions of the stator back iron

Component	Symbol	Magnitude	Units
Shaft axial length	H_{sh}	130.0	mm
Bearing length	l_b	16	mm
Shaft radius	r_{sh}	15.875	mm

Table D.10: Dimensions of the shaft

Appendix E

Derivation of finite element equations

E.1 Derivation of the interpolation function

With the assumption of linear variation of temperature inside a triangular finite element, and may be expressed as,

$$\theta(x, y) = e_1 + e_2 x + e_3 y \tag{E.1}$$

Therefore, at each corner, the temperature can be written as,

$$\theta_i = e_1 + e_2 x_i + e_3 y_i \tag{E.2}$$

$$\theta_j = e_1 + e_2 x_j + e_3 y_j \tag{E.3}$$

$$\theta_k = e_1 + e_2 x_k + e_3 y_k \tag{E.4}$$

In a matricial form

$$\begin{vmatrix} \theta_i \\ \theta_j \\ \theta_k \end{vmatrix} = \begin{vmatrix} 1 & x_i & y_i \\ 1 & x_j & y_j \\ 1 & x_k & y_k \end{vmatrix} \begin{vmatrix} e_1 \\ e_2 \\ e_3 \end{vmatrix}$$

The constants e_1, e_2 and e_3 can be expressed in terms of the nodal temperature θ_i, θ_j and θ_k as,

$$\begin{vmatrix} e_1 \\ e_2 \\ e_3 \end{vmatrix} = \frac{1}{2A} \begin{vmatrix} a_i & a_j & a_k \\ b_i & b_j & b_k \\ c_i & c_j & c_k \end{vmatrix} \begin{vmatrix} \theta_i \\ \theta_j \\ \theta_k \end{vmatrix}$$

where A is the area of the triangle $= \frac{1}{2} \mid (x_{ij}y_{jk} - x_{jk}y_{ij}) \mid$

$$x_{ij} = x_i - x_j$$

$$y_{ij} = y_i - y_j$$

and the constants $a_i, a_j, \ldots, c_k$ are

$$a_i = x_j y_k - x_k y_j$$

$$a_j = x_k y_i - x_i y_k$$

$$a_k = x_i y_j - x_j y_i$$

$$b_i = y_i - y_k$$

$$b_j = y_k - y_i$$

$$b_k = y_i - y_j$$

$$c_i = x_k - x_j$$

$$c_j = x_i - x_k$$

$$c_k = x_j - x_i$$

By substituting, e_1, e_2 and e_3 into Eq. (E.1) and rearrangement yields the equation

$$\theta(x, y) = N_i(x, y)\theta_i + N_j(x, y)\theta_j + N_k(x, y)\theta_k \qquad \text{(E.5)}$$

where

$$N_i(x,y) = \tfrac{1}{2A}(a_i + b_i x + c_i y)$$
$$N_j(x,y) = \tfrac{1}{2A}(a_j + b_j x + c_j y)$$
$$N_k(x,y) = \tfrac{1}{2A}(a_k + b_k x + c_k y)$$

The shape function $N_i(x,y)$ when evaluated at node $i(x_i, y_i)$ gives value of 1 and $N_i(x,y) = 0$ at node j and k, and at all points on the line passing through these nodes. Similarly the shapes N_j and N_k have a value of 1 at nodes j and k respectively and zero at other nodes.

E.2 Derivation of element matrices

The solution to the temperature problem is obtained by minimising the functional,

$$\begin{aligned}\Im &= \frac{1}{2}\int\int_R \left[k_x\left(\frac{\partial\theta}{\partial x}\right)^2 + k_y\left(\frac{\partial\theta}{\partial y}\right)^2 - 2q\theta\right] dxdy \\ &+ \int_{S_2} q'\theta dS_2 + \frac{1}{2}\int_{S_3} h(\theta-\theta_\infty)^2 dS_3 \end{aligned} \tag{E.6}$$

Differentiating Eq. (E.6) with respect to the variational parameters, θ_p; $p = i, j$ and k; gives,

$$\begin{aligned}\frac{\partial\Im}{\partial\theta_i} &= \int\int_R \left[k_x\frac{\partial\theta}{\partial x}\frac{\partial}{\partial\theta_i}\left(\frac{\partial\theta}{\partial x}\right) + k_y\frac{\partial\theta}{\partial y}\frac{\partial}{\partial\theta_i}\left(\frac{\partial\theta}{\partial y}\right) - q\frac{\partial\theta}{\partial\theta_i}\right] dxdy \\ &+ \int_{S_2} q'\frac{\partial\theta}{\partial\theta_i} dS_2 + \int_{S_3} h(\theta-\theta_\infty)\frac{\partial\theta}{\partial\theta_i} dS_3 \end{aligned} \tag{E.7}$$

Note that the surface integrals do not appear in the above equation if node i does not lie on S_2 and S_3.

However, Eq. (E.5) gives,

$$\frac{\partial\theta}{\partial x} = \frac{\partial N_i}{\partial x}\theta_i + \frac{\partial N_j}{\partial x}\theta_j + \frac{\partial N_k}{\partial x}\theta_k \tag{E.8}$$

and,

$$\frac{\partial \theta}{\partial \theta_i} = N_i \tag{E.9}$$

Therefore,

$$\frac{\partial}{\partial \theta_i}\left(\frac{\partial \theta}{\partial x}\right) = \frac{\partial N_i}{\partial x} \tag{E.10}$$

By substituting Eqs. (E.8) to (E.10) into Eq. (E.7) the differentiation of the functional with respect to the variational parameter θ_i becomes.

$$\begin{aligned}\frac{\partial \Im}{\partial \theta_i} &= \int\int_R \left[k_x\left(\frac{\partial N_i}{\partial x}\right)^2 + k_y\left(\frac{\partial N_i}{\partial y}\right)^2\right]\theta_i \\ &+ \left[k_x\frac{\partial N_i}{\partial x}\frac{\partial N_j}{\partial x} + k_y\frac{\partial N_i}{\partial y}\frac{\partial N_j}{\partial y}\right]\theta_j \\ &+ \left[k_x\frac{\partial N_i}{\partial x}\frac{\partial N_k}{\partial x} + k_y\frac{\partial N_i}{\partial y}\frac{\partial N_k}{\partial y}\right]\theta_k dxdy\end{aligned} \tag{E.11}$$

Similarly, one can take $\frac{\partial \Im}{\partial \theta_j}$ and $\frac{\partial \Im}{\partial \theta_k}$ and write equations similar to Eq. (E.11).

For the convective term

$$\int_{S_3} h\theta\frac{\partial \theta}{\partial \theta_i}dS_3 \tag{E.12}$$

becomes after substitution of the related expressions as,

$$\int_{S_3} h\theta\frac{\partial \theta}{\partial \theta_i}dS_3 = \int_{S_3} h(N_i^2\theta_i + N_iN_j\theta_j + N_iN_k\theta_k)dS_3 \tag{E.13}$$

The remaining terms are grouped together to give,

$$Q = \int\int_R qN_i dxdy - \int_{S_2} q'N_i dS_2 + \int_{S_3} h\theta_{infty}N_i dS_3 \tag{E.14}$$

By using Eqs. (E.11) to (E.14) Eq. (E.6) can be expressed in matrix form

$$\frac{\partial \Im}{\partial \theta} = [G_1 + G_2][\theta] - [Q] = 0 \tag{E.15}$$

where

$$[G_1] = \int\int_R [B]^T[D][B]dxdy \tag{E.16}$$

$$[G_2] = \int_{S3} h[N]^T[N]dS_3 \tag{E.17}$$

$$Q = q_1 - q_2 + q_3 \tag{E.18}$$

where

$$[B] = \begin{vmatrix} \frac{\partial N_i}{\partial x} & \frac{\partial N_j}{\partial x} & \frac{\partial N_k}{\partial x} \\ \frac{\partial N_i}{\partial y} & \frac{\partial N_j}{\partial y} & \frac{\partial N_k}{\partial y} \end{vmatrix}$$

$$[D] = \begin{vmatrix} k_x & 0 \\ 0 & k_y \end{vmatrix}$$

$$q_1 = \int \int_R q[N]^T dA \tag{E.19}$$

$$q_2 = \int_{S_2} q'[N]^T dS_2 \tag{E.20}$$

$$q_3 = \int_{S_3} h\theta_\infty [N]^T dS_3 \tag{E.21}$$

The elements of the matrices $[G_1]$, $[G_2]$ and Q can be assembled to obtain the overall equation as,

$$[G][\theta] = [Q] \tag{E.22}$$

Bibliography

[1] VARIABLE SPEED DRIVES, "lessons in efficient driving". Electrical Review, 13-16 April 1992.

[2] NASER, S.A., "Handbook of electrical machines". McGraw-Hill, Inc., 1987.

[3] KNIGHTS, D.E., "Efficient use of electricity in motor drives". Electronic and Power, Nov./Dec. 1977 pp. 921-924.

[4] MOHAN, N., "Improvement in energy efficiency of induction motors by means of voltage control". Trans. IEEE, Vol. PAS 99, No 4 July/August 1980, pp. 1466-1471.

[5] DRIVES MARKET "DC death knell: a false alarm?". Electrical Review 15-28 May, 1992, pp. 23-24.

[6] HOLMES, L., "Energy-saving motor controller: background and update". Electronic and Power, March 1982, pp. 232-235.

[7] "Energy efficient motors". Electrical Review, 20 March-2 April, 1992, pp.30-31

[8] BERTOTTI, G., BOGLEITTI, A., CHAMPI, M., CHIARABAGLIO, D., FIORILLO AND F., LAZZARI, M., "An improved estimation of iron losses in rotating electrical machines".Trans. IEEE on Magnetics, Vol. 25, No. 5, 1991.

[9] AIEE COMMITTEE REPORT, "Stray load losses measurement in induction machines". Trans. AIEE, 1959, pp. 67-71.

[10] ODOK, A.M., "Stray load losses and stray torques in induction machines". Trans. IAEE, Vol. 77, Pt.II, 1958, pp. 43-53.

[11] MURKHERJI, K.B.C., "Stray load losses in a.c. rotating machinery". A Review of State of the Art, ERA Report 7/T102, 1956.

[12] SCHWARZ, K.K., "Survey of basic stray load losses in squirrel cage induction motors". Proc. IEE, Vol. 111, 1964, pp.1565-1573

[13] JIMOH, A.A., FINDLAY, R.D., POLOUDJADOUFF, M., "Stray load losses in induction machines. Part 1 : Definition, origin and measurement. Part 2 : Calculation and reduction". IEEE, PAS, Vol., 104, 1985, pp.1500-1512

[14] "Discussion on stray load losses". Proc. IEE, Vol. 112, 1965, pp.1750-1759

[15] BAHBOUTH, S., ROYE, D. AND PERRET, R., "Heating of static inverter fed induction machine". IEEE/IAS conference, Cincinatti, 1980, pp.540-544.

[16] OLIVER, E., PERRET, R. AND PERRARD, J., "Localisation of the losses in an induction machine supplied by an inverter". Electric machine and power systems, Vol. 9, 1984, pp.401-412.

[17] CHITLET, C., ISNARD, R., HADI, A.W. AND BRUNELLO, M., "Analysis and localisation of losses in an induction machine using a calorimetric method". EMPS, Vol.18, 1990, pp.29-39.

[18] LAFFOON, C.M. AND CALVERT, J.F., "Additional losses of synchronous machines". Trans. AIEE, 1927, pp.84-97

[19] GILBERT, A.J., "A method of measuring loss distribution in electrical machines". Proc. IEE, Vol. 108A, 1961, pp.239-244.

[20] MACHINE DESIGN, "Why protect motors". August 13 1964, pp. 145-158.

[21] SCREENIVASAN, V.K., "Thermal design of totally enclosed fan cooled induction motors". IEEE PES winter meeting, Paper A 77 097-9, 1977.

[22] KOTNIK, R.L., "An equivalent thermal circuit for non ventilated induction motors". Trans. AIEE, Vol. 73, Pt. 3A, 1954, pp.1604-1609.

[23] SODERBERG, C.R., "Steady flow of heat in large turbine generators". Trans. AIEE, Vol. 50, 1931, pp.787-802.

[24] PEREZ, I.J. AND KASSAKIAN, J.K., "A stationary thermal model for smooth airgap rotating electrical machines". Elec. Mach. Electromech., Vol. 3, No 3-4, 1979, pp.285-303.

[25] PEREZ, I.J., "Computer aided design of high speed electric machinery". M.S. Thesis, E.E. Department, MIT, Cambridge, Massuchusetts, 1977.

[26] MELLOR, P.H., ROBERT, D. AND TURNER, D.R., "Lumped parameter thermal model for electrical machines of TEFC design". Proc. IEE, Vol. 138, No. 5, 1991, pp.205-218.

[27] NUMBURI, N.R. AND BARTON, T., "Thermal modelling of an induction motor". Trans. IEEE, PAS, Vol. 102, 1983, pp.2636-2639.

[28] ROSENBERRY, G.M., "The transient stalled temperature rise of cast aluminum squirrel cage rotors for induction motors". Trans. AIEE, Pt.III, PAS, Vol.74, 1955, pp.819-824.

[29] WILSON, P., "Motors and motor control: Protecting the machinery as well as motor". Electrical Review, Vol. 215, No 15, 16 Nov., 1984, pp. 35-36.

[30] ROBERTS, T.J., "Determination of the thermal constants of heat flow equations of electrical machines". Proc. Instn. Mech. Engrs., Vol. 148, Pt.3E, 1969-1970, pp.84-92.

[31] PARROTT, J.E and STUCKES, A.D., "Thermal conductivity of solids". Pion Limited, 1975.

[32] TYE, R.P., "Thermal conductivity". Academic Press, 1969, Vol. 1 and 2

[33] ROBERTS, T.J., "The solution of heat flow equations in large electrical machines". Proc. IME, Vol. 184, Pt.3E, 1969-70, pp.70-83.

[34] EMERY, A.F. AND CARSON, W.W. "Evaluation of use of the finite element method in the computation of temperature". ASME, Winter Annual Meeting, Nov. 16-20, Los Angeles, 1969.

[35] SARKAR, D., MUKHERJEE, P.K. AND SEN, S.K., "Approximative analysis of steady state heat conduction in an induction motor" Trans, IEEE on Energy Conversion, Vol. 8, No. 1, 1993, pp. 78-84.

[36] ARMOR, A.F., AND CHARI, M.V.K., "Heat flow in the stator core of large turbine generators, by the method of 3-dimensional finite elements. Part I: Analysis by scalar potential formulation. Part II: Temperature distribution in the stator iron" Trans, IEEE PAS, Vol.95, No. 5, Sept./Oct. 1976, pp.1648-1668.

[37] ARMOR, A.F., "Transient, 3-dimensional, finite element analysis of heat flow in turbine generator rotors". Trans. IEEE PAS, Vol. 99, No. 3, May/June 1980, pp.934-946.

[38] SARKAR, D., MUKHERJEE, P.K. AND SEN, S.K., "Use of 3-dimensional finite elements for computation of temperature distribution in the stator of an induction motor". Proc. IEE, Vol. 138, No. 2, March 1991, pp-75-86.

[39] SARKAR, D., MUKHERJEE, P.K. AND SEN, S.K., "Temperature rise of induction motor during plugging". Trans. IEEE on Energy Conversion, Vol. 7, No. 1, March 1992, pp-116-122.

[40] BOURNE, R. "Electrical rotating machine testing". Iliffe Books Ltd. London, 1969.

[41] BRITISH STANDARD "BS 4999, Part 33", 1977

[42] ANSI/IEEE Std 112, 1984, "IEEE Standard test procedure for induction motors and generators".

[43] CUMMINGS, P.G., BOWERS, W.D. AND MARTINY, W.J., "Induction motor efficiency test methods ". Trans. IEEE, IA, Vol. 17, 1981, pp.253-272

[44] RAO, S.V., "Losses in ferromagnetic laminations due to saturation". Proc. IEE, Vol. 111, N^0 12, Dec. 1964, pp.2111-2117

[45] ALGER, P.L. AND EKSERGIAN, R., "Induction motor core losses". Jour. AIEE, 1920, pp.906-920

[46] LINKOUS, C.E., "Computing iron losses in fractional horse power induction motors". Trans. AIEE, Vol. 78, 1959, pp. 175-178

[47] LORENZEN, H.W. AND NUSCHELER, R., "The calculation of iron loss and field distribution in anisotropic steel laminations". Trans. IEEE, vol. Mag-24, 1988, pp.1972-1974

[48] ATALLAH, K., ZHU, Q.Z. AND HOWE,D., "An improved method for predicting iron losses in brushless permanent magnet DC drives". Trans. IEEE, Vol. 28, No. 5, 1992, pp. 2997-2999.

[49] TURNER, D.R., BINNS,K.J., SHAMSADEEN, B.N. AND WARNE,D.F., "Accurate measurement of induction motor losses using balanced calorimeter". Proc. IEE, Vol. 138, No 5, Sept. 1991, pp.233-242

[50] ALGER, P.L., "Induction machines". Gordon and Breach Science Publishers, 1970

[51] LIWSCHITZ,-GARIK, M., "Skin effect bars of squirrel cage rotors". Trans. AIEE, Vol. 73, 1954, pp.255-258

[52] LIWSCHITZ-GARIK, M., "Computation of skin effect in bars of squirrel cage rotors", Trans. AIEE, Vol. 74, 1955, pp.768-771

[53] ALGER, P.L., ANGST AND G., DAVIES, E.J., "Stray load losses in polyphase induction machines". Trans. AIEE, Vol. 78, 1959, pp.349-357

[54] CHRISTOFIDES, N., "Origin of load losses in induction motors with cast Aluminium rotors". Proc. IEE, Vol. 112, 1965, pp.2317-2332

[55] SUBBA, R.V. AND BUTLER, O.I., "Stray load losses of polyphase cage-induction motors with particular reference to the condition of imperfect rotor-bar-iron insulation". Proc. IEE, Vol.116, 1967, pp. 737-751.

[56] BIRD, B.M., "Measurement of stray load losses in squirrel cage induction motors". Proc. IEE, Vol. 111, 1964, pp.1697-1705

[57] "Polyphase induction motors for generating station". ANSI, C50.41, 1977

[58] BARTON, T.N. AND AHMAD, V., "The measurement of induction motor stray loss and its effect on performance". Proc. IEE, 1958, Vol. 105c, pp.69-

[59] LARGIADER, H., "Design aspects of induction motors for traction applications with supply through static frequency changers". The Brown Boveri Review, Vol. 4, 1970, pp.152-167

[60] KLINGSHIRN, E.A. AND JORDAN, H.E., "Polyphase induction motor performance and losses on nonsinusoidal voltage sources". Trans. IEEE, PAS, Vol. 87, 1968, pp.624-631

[61] CHALMERS, B.J. AND WILLIAMSON, A.C., "Stray losses in squirrel cage induction motors - Validity and of reverse rotation test method". Proc. IEE, Vol. 110, 1963, pp.1773-1777

[62] BENAMROUCHE, N., "An investigation of loss distribution in induction motors fed from nonsinusoidal supplies". PhD Thesis, University of Sheffield, 1990

[63] CZERLINSKY, E.R. AND MACMILLAN, R.A., "A calorimeter method for core loss measurements". AIAA Conference on magnetism and magnetic materials, 1957, pp. 311-315.

[64] ROSS, M.D., "Time temperature tests to determine machine losses". Electrical Engineering, 1935, pp. 512-515.

[65] BALL, D.A. AND LORCH, H.O., "An improved thermometric method of measuring local power dissipation". J. Sci. Instrum., Vol. 42, 1965, pp.90-93.

[66] NOLTINGK, B.E., "Instrumentation reference book". Butterworth and Co. Ltd., 1988.

[67] SWANN, S.A. AND SALMON, J.W., " Effective resistance and reactance of a rectangular conductor placed in a semi-closed slot". Proc. IEE, Vol. 110, No 9, Sept 1963, pp. 1656-1662

[68] BENAMROUCHE, N., McCormick, M., OMETTO, A. AND PARRASSILITI, F., "Spatial energy loss density measurements in induction motors". Proc. ICEM, Pisa Itally, Vol.2, pp.35-40, 1988.

[69] TINDALL, C.E. AND BRANKIN, S. "Loss at source thermal modelling in salient pole alternators using 3-dimensional finite difference techniques". Trans. IEEE on Magnetics, Vol. 24, No. 1, January 1988, pp.278-281.

[70] "Heat transfer and fluid data book". General Electric 1969.

[71] HEILES, F., "design and arrangement of cooling fins". Digest, Vol. 13, No 10, 1952, pp.343-346.

[72] ROHSENOW, W.M., HARTNEH, J.P. AND GANIC, E.N., "Hand book of heat transfer fundamentals". McGraw-Hill, Inc. Second Edition, 1985.

[73] GAZLEY, C.,"Heat transfer characteristics of rotational and axial flow between concentric cylinders". Trans. ASME, Jan. 1958, pp.79-89.

[74] TAYLOR, G.I., "Distribution of velocity and temperature between concentric cylinders". Proc. Royal Society, Vol. 159 A, 1935, pp.546-578.

[75] LUKE, G.E., "The cooling of electric machines". Trans. AIEE, Vol. 45, 1923, pp.1278-1288.

[76] CHAPMAN, A.J., "Heat transfer". MaCmillan Co. 2^{nd} Edition, 1967.

[77] BRUNOT, I.W., AND BUCKLAND, F.F., "Thermal contact resistance of laminated and machined joints". Trans. ASME, April 1950, pp.253-257.

[78] ROBERTS, D., "The application of an induction motor thermal model to motor protection and other functions". PhD thesis, University of Liverpool, 1986.

[79] SHLYKOV, Y.P. AND GANNIN, Y.A., "Thermal resistance of metallic contacts". Int. J. Heat Transfer, Vol.7, 1964, pp.921-929.

[80] SAY, M.G., "Alternating current machines". Pitman, 1976.

[81] ROTH, E. "Introduction a l'etude analytique de l'echauffement des machines electriques". Bulletin de la Societe Francaise d'Eloctroniciens, Vol. 7, 1927, pp. 846-965.

[82] OSLEJSCK, O., "Analysis of the cooling of an enclosed asynchronous motor". Electro. Obzor., Vol.54, 1965, pp.527-537.

[83] BATE, J.J. AND TUSTIN, A. "Temperature rises in electrical machines as related to the properties of thermal networks". Proc. IEE, Vol.103.A, No. 11, 1956, pp.471-482.

[84] WILLIAMS, A., "Heat flow across stacks of steel laminations". J. Mech. Engrs. Science, Vol.13, No 3, 1971, pp.217-223.

[85] MUKOSIEJ, J. "Problems of thermal resistances measurement of equivalent thermal network of electric machines". pp.199-202.

[86] PRESS, W.H., FLANNERY, B.P., TEUKOLSKY, S.A. AND VETTERLY, W.T., "Numerical recipes, the art of scientific computing". Fortran version, Cambridge University Press, 1989.

[87] LOW, W.F., "Meshgen 2D, automatic 2D mesh generation program". Dept. of Electronic and Electrical Engineering, University of Sheffield, U.K.

[88] RILEY, C.D., "Magstat 2D, interactive 2D finite element field solver and post processor". Dept. of Electronic and Electrical Engineering, University of Sheffield, U.K.

[89] RAO, S.S., "The finite element method in engineering". Pergamon Press Plc., 2^{nd} Edition, 1989.

[90] LOW, W.F., "The computation of magnetostatic fields in permanent magnet devices". Ph.D. Thesis, University of Sheffield, 1985.

Publications

1. A. Bousbaine, W.F. Low, M. McCormick, "Thermal modelling of induction motors". Proc. 26^{th}, UPEC Conference 1991, Brighton Polytechnic, pp.127-130.

2. A. Bousbaine, W.F. Low, M. McCormick, N. Benamrouche, "Thermal modelling of induction motors based on accurate loss density measurements". Proc. ICEM, Sept. 1992, UMIST, Manchester, pp.953-957.